Measuring crosswind using scintillometry

Daniëlle van Dinther

Thesis committee

Promotor

Prof. Dr A.A.M. Holtslag
Professor of Meteorology
Wageningen University

Co-promotor

Dr O.K. Hartogensis
Assistant professor, Meteorology and Air Quality Group
Wageningen University

Other members

Prof. Dr R. Uijlenhoet, Wageningen University
Dr F. Beyrich, German Meteorological Service, Lindenberg, Germany
Prof. Dr S. Crewell, University of Cologne, Germany
Dr B. Wichers Schreur, KNMI, de Bilt

This research was conducted under the auspices of the SENSE Research School

Measuring crosswind using scintillometry

Daniëlle van Dinther

Thesis
submitted in fulfilment of the requirements for the degree of doctor
at Wageningen University
by the authority of the Rector Magnificus
Prof. Dr M.J. Kropff,
in the presence of the
Thesis Committee appointed by the Academic Board
to be defended in public
on Friday 16 January 2015
at 4 p.m. in the Aula.

D. van Dinther
Measuring crosswind using scintillometry
163 pages.

PhD-thesis, Wageningen University, Wageningen, NL (2015)
With references, with summaries in Dutch and English

ISBN 978-94-6257-1815

Contents

1 Introduction **9**
1.1 Motivation . . . 9
1.2 Scintillometry . . . 9
1.3 Open issues discussed in this thesis . . . 12
1.4 Research strategy . . . 14
1.5 Outline of this thesis . . . 15

2 Theory **17**
2.1 Atmospheric turbulence . . . 17
2.2 Power spectra . . . 19
2.2.1 Spectral visualizations . . . 19
2.2.2 Fast Fourier transform . . . 20
2.2.3 Wavelet transform . . . 20
2.3 Scintillometry . . . 23
2.3.1 Scintillation (co)variance function . . . 24
2.3.2 Scintillation power (co)spectra . . . 26
2.3.3 Scintillation (co)variance . . . 28
2.3.4 Scintillation weighting functions . . . 29

3 Crosswind from a Single-Aperture Scintillometer using Spectral techniques **31**
3.1 Introduction . . . 32
3.2 Theory . . . 34
3.3 Method . . . 38
3.3.1 Determination of scintillation power spectra . . . 38
3.3.2 Crosswind algorithms based on scintillation spectra . . . 39
3.3.3 Crosswind algorithm used by SRun . . . 42
3.3.4 Validity of the spectral techniques . . . 43

3.4 Experimental set-up 48
3.5 Results and discussion 50
3.5.1 Crosswinds from FFT spectra 50
3.5.2 Crosswinds from wavelet spectra 53
3.5.3 Crosswind with Scintec's BLS900 algorithm 55
3.6 Conclusions 57
3A Appendix: Varying scintillometer beam height and crosswind 59
3A.1 The effective crosswind height of a scintillometer 59
3A.2 Validity of the spectral techniques to obtain $U_\perp$ with a scintillometer over a slant path 60

4 Using the Time-Lag Correlation Function of Dual-Aperture Scintillometer measurements to Obtain the Crosswind 65

4.1 Introduction 66
4.2 Theory 67
4.3 Methods 72
4.3.1 Peak method 73
4.3.2 Briggs method 73
4.3.3 Zero-slope method 75
4.3.4 Lookup table method 75
4.4 Experimental setup and data treatment 77
4.4.1 Experimental setup 77
4.4.2 Noise filtering 78
4.5 Results and discussion 78
4.5.1 Mean crosswind 79
4.5.2 Briggs-quality check 83
4.5.3 Standard deviation of the crosswind 85
4.5.4 SRun version 1.14 87
4.6 Conclusions 88
4A Appendix: Determination of the Time-Lag Correlation function 91
4A.1 Shifting the two signals with respect to each other to obtain $r_{12}(\tau)$ 91
4A.2 Time window over which $r_{12}(\tau)$ should be determined 92

5 Observing crosswind over urban terrain using scintillometer and Doppler lidar **95**
5.1 Introduction 96
5.2 Theory and Methods 97
5.2.1 Scintillometry 97
5.2.2 Doppler lidar 100
5.3 Experimental setup 101
5.4 Results and discussion 103
5.4.1 Doppler lidar path-resolved crosswinds 103
5.4.2 Path-averaged crosswinds 106
5.4.3 Variable crosswinds along the path 109
5.5 Conclusions and outlook 112

6 Runway wake vortex, crosswind, and visibility detection with a scintillometer at Schiphol airport **115**
6.1 Introduction 116
6.2 Theory 117
6.2.1 Wake vortices 118
6.2.2 Crosswind 118
6.2.3 Visibility 119
6.3 Methods 120
6.3.1 Wake-vortex detection 120
6.3.2 Crosswind 122
6.3.3 Visibility 122
6.4 Experimental set-up and data treatment 123
6.4.1 Setup 124
6.4.2 Data treatment 125
6.5 Results and discussion 126
6.5.1 Wake-vortex detection 126
6.5.2 Crosswind 133
6.5.3 Visibility 134
6.6 Conclusions 136

7 Summary **139**

8 General discussion & Outlook **143**
8.1 General discussion 143
8.2 Outlook 146

References **149**

Samenvatting **155**

Dank / Thanks! **159**

List of publications **161**

1

Introduction

1.1 Motivation

This thesis outlines how a scintillometer device measures the so-called crosswind ($U_\perp$), where $U_\perp$ is defined as the wind component perpendicular to a path (depicted in Fig. 1.1). A scintillometer is able to obtain a path averaged value of the crosswind ($\overline{U_\perp}$) (among others Lawrence *et al.*, 1972; Wang *et al.*, 1981). More details on scintillometry are given in Section 1.2 and 2.3 of this thesis.

Airports can strongly benefit from $\overline{U_\perp}$ measurements. Strong $U_\perp$-values on an airport runway introduce a serious safety risk for airplanes either landing or taking off (Wong *et al.*, 2006). Therefore, as a safety measure, the 10-m $U_\perp$ magnitude is restricted to a certain value depending on the type of airplane for airports operations. Nowadays, the wind field near the runway is typically represented by local measurements (e.g., cup anemometer and wind vane). Local measurements are more susceptible to errors due to changes in the wind field under the influence of ground clutter. Therefore, a path-averaged value of $U_\perp$, as that given by the scintillometer, is more representative for $U_\perp$ along the runway than point measurements. The motivation of this thesis is, therefore, to measure a path-averaged value of $U_\perp$ near an airport runway using scintillometry.

1.2 Scintillometry

A scintillometer consists of a transmitter and a receiver, typically spaced a few hundred meters to a few kilometers apart. As the name already suggests, a scintillometer measures scintillations. These are visible with the naked eye for example on a hot summer day when the air seams to vibrate and the image one is looking at is distorted.

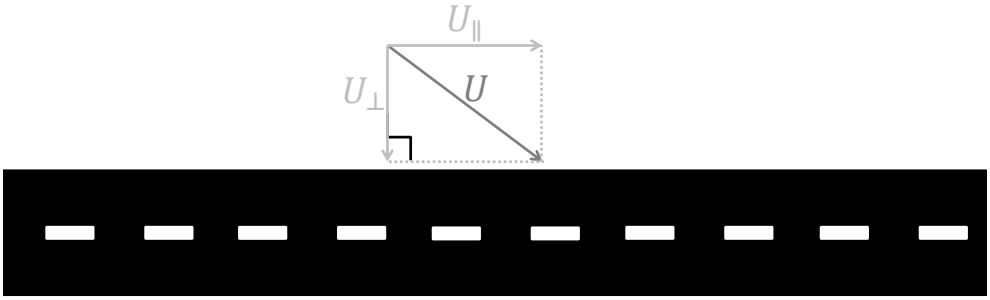

Figure 1.1: Schematic sketch of the crosswind ($U_{\perp}$) and the parallel wind component ($U_{\parallel}$) on a runway given a certain horizontal wind speed (U).

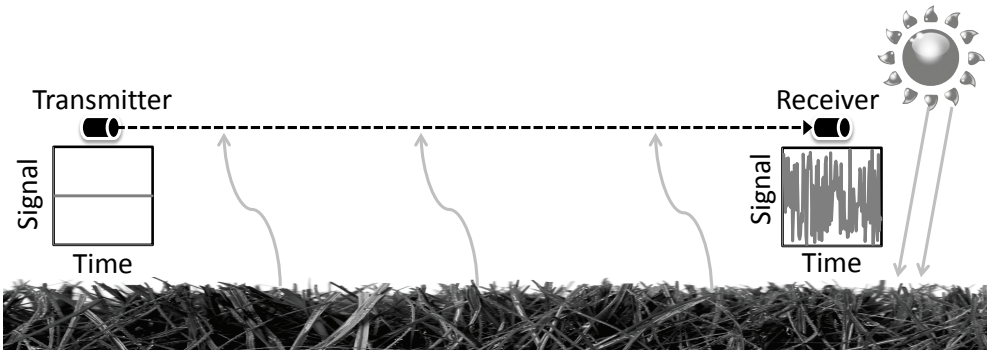

Figure 1.2: Schematic sketch of a scintillometer setup. The sun heats the surface causing warm air to rise in eddies that refract the scintillometer beam, resulting in signal intensity fluctuations at the receiver side.

The scintillations are caused by turbulent motions of the air above the Earth's surface in the lower part of the atmosphere (i.e., surface layer). The transmitter of a scintillometer emits light with a certain wavelength, of which the intensity is measured by the receiver. In the surface layer a parcel of air with a higher temperature than its surrounding rises and parcels form so called eddies. These eddies have a different air temperature and humidity than their surrounding, and therefore also a different air density. This difference in air density causes the light beam of the scintillometer to be refracted. As a result of the turbulent nature of the surface layer the eddy field through which the light beam travels is constantly changing, and therefore the light intensity fluctuates at the receiver's side, as is schematically depicted in Fig. 1.2. These fluctuations are the scintillation signal.

There are two phenomena driving the change of eddy fields in the scintillometer path; wind and eddy decay. The wind blows a different eddy field into the scintillometer path, while eddy decay causes large eddies to break up into smaller eddies (the process of eddy decay is discussed in more detail in Section 2.1). The scintillometer measures with a high frequency (in this thesis 500 Hz), thus it can be assumed that the eddy field does not decay while it is being transported by the scintillometer (i.e., Taylor's frozen turbulence assumption is valid). Thereby, wind is the only phenomenon driving the change in the eddy field.

Traditionally scintillometers are used to determine the surface fluxes, i.e., exchange of heat or moisture between the Earth's surface and the atmosphere. When there is more exchange (i.e., larger surface fluxes) the atmosphere is more turbulent, causing more fluctuations in the scintillation signal. Therefore, the variance in the scintillation signal is linked to the surface fluxes. A benefit of the scintillometer compared to other measurement devices (e.g., sonic anemometer and gas analyzer) is that it yields path-averaged surface fluxes, which are more suitable to compare with model output than point measurements (Kleissl *et al.*, 2009). Another benefit is that the scintillometer needs less averaging time than point measurements to obtain statistically sound surface fluxes ($\leq$ 1 min compared to $\geq$ 10 min) (Van Kesteren *et al.*, 2013).

This thesis focuses on crosswind measurements by a scintillometer. The crosswind can be obtained from scintillometer measurements by either the time-lagged correlation function ($r_{12}(\tau)$) between two spatially separated scintillometers (i.e., dual-aperture scintillometer) or the scintillation power spectra ($S_{11}(f)$) of a single aperture scintillometer. The theoretical models behind $r_{12}(\tau)$ and $S_{11}(f)$ are discussed in Section 2.3. Here I will give a general outline on how $r_{12}(\tau)$ and $S_{11}(f)$ are influenced by $U_{\perp}$.

When two scintillometers are installed side by side (i.e., dual-aperture scintillometer), the wind transports the eddy field from one scintillometer to the other. When Taylors frozen turbulence assumption is valid, the eddy field does not change while it is being transported through the two scintillometer paths (see Fig. 1.3a). Therefore, the only difference between the two scintillation signals is a time-shift (see Fig. 1.3b). The stronger the crosswind the faster the eddy field will be transported from the one to the other scintillometer, and therefore the shorter the time-shift in between the two signals. The time shift, and thereby the crosswind, can be obtained from $r_{12}(\tau)$. Methods that rely on $r_{12}(\tau)$ to obtain the crosswind are discussed in Chapter 4 of this thesis.

The crosswind can also be obtained from the scintillation power spectra, which visualize how much a certain frequency contributes to the variance of the scintillation

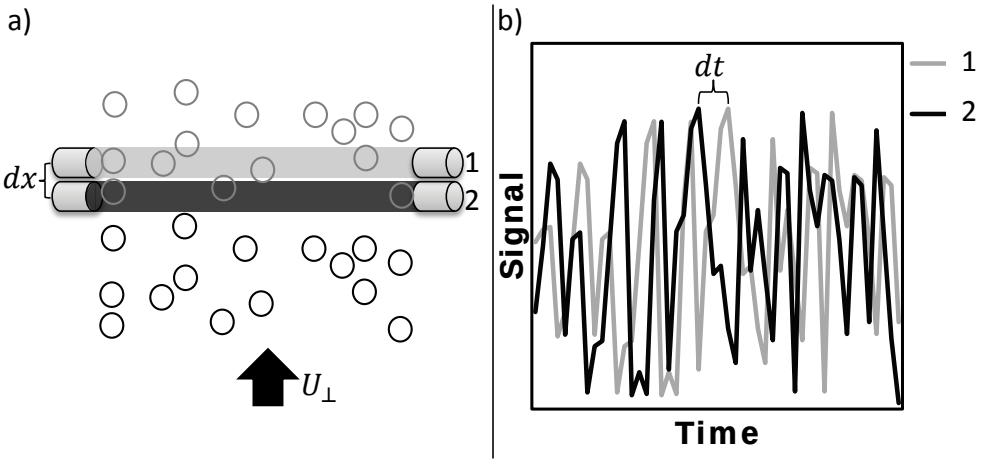

Figure 1.3: (a) Schematic sketch of a dual-aperture scintillometer. (b) Schematic graph of two scintillometer signals indicating a time-shift (dt) in between the two signals.

signal. An example of such a $S_{11}(f)$ is given in Fig. 1.4b. An eddy field that is blown through the scintillometer path causes a certain variance in the scintillation signal. If the same eddy field is blown through the scintillometer path but faster (i.e., by a stronger crosswind), the variance in the signal will be the same, but the signal will be squeezed in time (see Fig. 1.4a). Therefore, the higher frequencies will contribute more to the scintillation signal, which will be visible in $S_{11}(f)$ (see Fig. 1.4b). In that way, the crosswind can be determined by obtaining a characteristic point on the frequency axis of $S_{11}(f)$. Methods that rely on $S_{11}(f)$ to obtain the crosswind are discussed in Chapter 3 of this thesis.

1.3 Open issues discussed in this thesis

The application of measuring crosswind with a scintillometer is not new. Briggs *et al.* (1950) already suggested a long time ago that with a spatially separated scintillometer, the crosswind can be measured from the time-lagged correlation function between the two signals. Wang *et al.* (1981) showed that a single-aperture scintillometer can also be used to obtain the crosswind through the autocovariance function, which is related to the scintillation spectra. As far as could be traced back, all previous studies relied on experimental calibration to obtain the crosswind from scintillometer measurements. Theoretical models of both the time-lagged correlation function (Lawrence *et al.*,

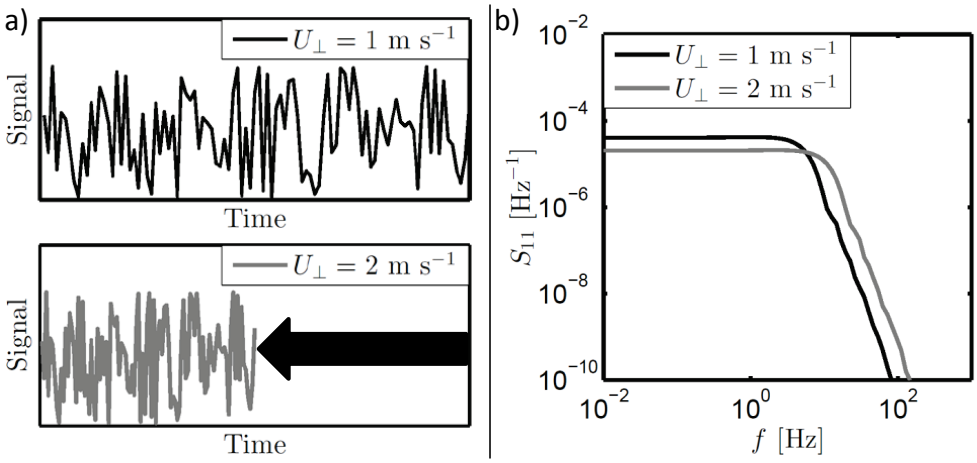

Figure 1.4: (a) Schematic sketch of a scintillometer signal which is squeezed in time when $\overline{U_\perp}$ is higher. (b) Scintillation spectra for a large-aperture scintillometer for $\overline{U_\perp}$ values of 1 and 2 m s^{-1}.

1972) and scintillation spectra (Clifford, 1971) exist, which can make experimental calibration redundant. The first research question of this thesis is:

Question 1: Are the theoretical models by Lawrence *et al.* (1972) and Clifford (1971) suitable to calibrate the crosswind measurements of a scintillometer, instead of experimental calibration?

Besides calibration, the models of Lawrence *et al.* (1972) and Clifford (1971) also give the opportunity to obtain the crosswind using the shape of the theoretical time-lagged correlation functions and the theoretical scintillation spectra. Based on that, the second research question of this thesis is:

Question 2: Can the shape of the theoretical models by Lawrence *et al.* (1972) and Clifford (1971) be used to obtain the crosswind?

Ward *et al.* (2011) showed that a variable crosswind along the scintillometer path smooths the scintillation spectra. However, their focus was not on crosswind measurements but on scintillation spectra and structure parameter measurements. It remains unknown to what extent the scintillometer crosswind measurements are influenced by variable crosswinds along the path. The third research question addressed in this thesis is thus:

Question 3: How are the crosswind measurements of a scintillometer influenced by variable crosswind values along the scintillometer path?

In Section 1.1 we stated that path-averaged crosswind measurements are desirable near airport runways to ensure safety. However, at airport runways there is turbulence produced by the airplanes themselves, which will influence the scintillation signal. Furthermore, there are also two other applications of scintillometers which might be beneficial to ensure airport safety. First, it was noted by Beyrich *et al.* (2002) that fog introduces a drop in the signal of the scintillometer. Therefore, it might be possible to estimate visibility using a scintillometer. Second, wake vortices created by airplanes can cause safety issues for the immediately following airplane landing or taking off. These wake vortices are turbulent motions, which should affect the scintillation signal. Thereby, making it possible to detect wake vortices with a scintillometer. The fourth (and last) research question asked in this thesis is:

Question 4: To what extent can a scintillometer detect wake vortices, crosswind, and visibility near an airport runway?

1.4 Research strategy

The four research questions are addressed using different experimental datasets. In this section I state which datasets are used to answer the research questions and which research strategy is chosen.

Questions 1 & 2 are answered on the hand of data collected on a flat grassland site in the Netherlands. On this site the crosswind can be assumed to be constant along the scintillometer path. Different methods will be used to obtain the crosswind from scintillometer measurements using both the scintillation spectra and the time-lagged correlation function. The methods are calibrated using the models of Clifford (1971) and Lawrence *et al.* (1972). Also, new methods are introduced where the crosswind is obtained using the shape of the scintillation spectra and time-lagged correlation function from the theoretical models of Clifford (1971) and Lawrence *et al.* (1972). We will validate the crosswind values obtained from the scintillometer with those calculated from sonic anemometer measurements.

Question 3 is first addressed using the theoretical model of Clifford (1971) to investigate the influence of a slant path on scintillation spectra, and thereby the measurement of the crosswind. A logarithmic wind profile is used to calculate the change of the crosswind along the path, which is than used in the model of Clifford (1971). The question is also answered by using the model of Lawrence *et al.* (1972), where two

extreme cases are tested with two different crosswind values on the two halves of the scintillometer path.

The question is lastly addressed by analyzing data from an experiment undertaken in the city of Helsinki, in Finland. In this experiment a Doppler lidar and scintillometer were setup along-side each other. From the Doppler lidar measurements the crosswind can be calculated for each range-gate using a duo-beam method described by Wood *et al.* (2013c). By doing so, the values of the crosswind along the scintillometer path are obtained. These values can be used to calculate the theoretical scintillation spectra and time-lagged correlation functions, using the models of Clifford (1971) and Lawrence *et al.* (1972), respectively. These theoretical scintillation spectra and time-lagged correlation functions can be compared to the measured ones by the scintillometer.

Question 4 is addressed using experimental data collected at Schiphol airport in the Netherlands. The data consisted of scintillometer measurements, which are compared to wind and visibility measurements obtained by the Royal Netherlands Meteorological Institute (KNMI). First, we investigate if it is also possible to detect wake vortices shed by airplanes. For detection of wake vortices the intensity fluctuations measured by the scintillometer are used, which should increase when a wake vortex is present in the scintillometer path. The registered take-offs and landings from Schiphol airport can identify if indeed a wake vortex should be present in the scintillometer signal. Second, we investigate if the crosswind values obtained from the scintillometer over a short 3-s time window are comparable to observations made simultaneously by a cup anemometer and wind vane. Third, the applicability of scintillometer as a visibility measurement device is investigated, by comparing the intensity level measured by the scintillometer with visibility measurements of KNMI.

1.5 Outline of this thesis

Before going into detail about the issues discussed in Section 1.3, Chapter 2 briefly discusses some of the theory behind atmospheric turbulence, obtaining power spectra, and scintillometry. Chapter 3, discusses how the crosswind can be obtained from single-aperture scintillometer measurements using the scintillation spectra. In this chapter it is investigated if the theoretical model of Clifford (1971) can be applied for calibration. In appendix 3A we investigate if the crosswind measurements of a scintillometer are influenced by a slant scintillometer path.

The methods to obtain the crosswind from the time-lagged correlation function of a dual-aperture scintillometer are discussed in Chapter 4. In this chapter we also

investigate if the model of Lawrence *et al.* (1972) can be used to calibrate the scintillometer crosswind measurements. This model also opens the possibility to investigate how in theory the time-lagged correlation function responds to a variable crosswind along the path, which is done in Section 4.2. Besides using the models of Clifford (1971) and Lawrence *et al.* (1972), Doppler lidar measurements along the scintillometer path are used to validate the scintillometer crosswind measurements in a complex urban environment in Chapter 5.

The ability of the scintillometer to detect wake vortices, crosswind, and visibility near an airport runway are discussed in Chapter 6. In Chapter 7 I summarize the main finding of this thesis, and in Chapter 8 I place the findings of this thesis in a broader perspective.

2

Theory

2.1 Atmospheric turbulence

The typically turbulent nature of the lower part of the atmosphere affects the scintillation signal. The following section discusses some of the basics concerning atmospheric turbulence.

In the lower part of the atmosphere heat, water vapor, and momentum are exchanged between the Earth's surface and the atmosphere. This exchange is mainly driven by buoyancy and wind shear. Buoyancy causes air parcels that have a higher temperature than their surrounding to rise in turbulent eddies. Besides transporting heat, eddies also transport humidity, momentum, and other air quantities.

Eddies have different sizes, which range from millimeters to kilometers (Garratt, 1992). When sampling a turbulent signal (e.g., temperature) in open air all eddy sizes contribute to the signal. How much each eddy size contributes to the signal is expressed in the turbulence spectrum (see Fig. 2.1).

The turbulence spectrum can be divided into three ranges; the production range, the inertial sub-range, and the dissipation range (see Fig. 2.1). The production range is the range where large eddies are produced by the main flow. The inertial sub-range is the range where eddies break up into smaller eddies without gaining or loosing energy. Thus the slope of the energy spectrum within this range is constant ($K^{-5/3}$), according to the Kolmogorov's law (Kolmogorov, 1941). The dissipation range is the range where small eddies dissipate into heat (typically ~ 1 mm).

The structure parameter of a quantity x (C_{x^2})) gives the linear relationship, in the inertial subrange, between spectral energy and $K^{-5/3}$ (where K is the turbulent spatial wavenumber), according to the Kolmogorov's law (Kolmogorov, 1941). This

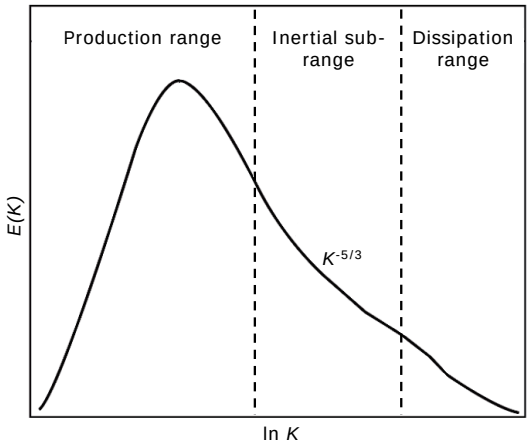

Figure 2.1: Schematic plot of a turbulence spectrum, with the production range, inertial sub-range, and dissipation range indicated (adopted from Foken (2008)).

parameter is a measure of the intensity of fluctuations of x caused by turbulence. The Kolomogorov's law states (Kolmogorov, 1941):

$$S_x = 0.25 C_{x^2} K^{-5/3}, \tag{2.1}$$

where S_x is the power spectra of x.

Instead of a turbulent spectrum the fluctuations of a quantity in the atmosphere are also expressed in the second order structure function of the quantity (D_{x^2}), which is given by (Monin & Yaglom, 1975):

$$D_{x^2} = \overline{[x(y) - x(y+r)]^2}, \tag{2.2}$$

where $x(y)$ is the value of x at location y, $x(y+r)$ is the value of x at a location r away from y, and the overbar indicates averaging. In the inertial range the increase in D_{xx} is linear with C_{x^2} and $r^{2/3}$ (Obukhov, 1949). Thus, C_{x^2} can also be obtained from x measurements at two different locations, which is given by (Monin & Yaglom, 1971):

$$C_{x^2} = \frac{D_{x^2}}{r^{2/3}}. \tag{2.3}$$

Assuming Taylors frozen turbulence hypothesis the signal of a quantity does not change while the eddy field is being transported from one measurement location to the other. Therefore, C_{x^2} can then be calculated from one point measurements using:

$$C_{x^2} = \frac{\overline{[x(t) - x(t+\Delta t)]^2}}{U \Delta t^{2/3}}, \tag{2.4}$$

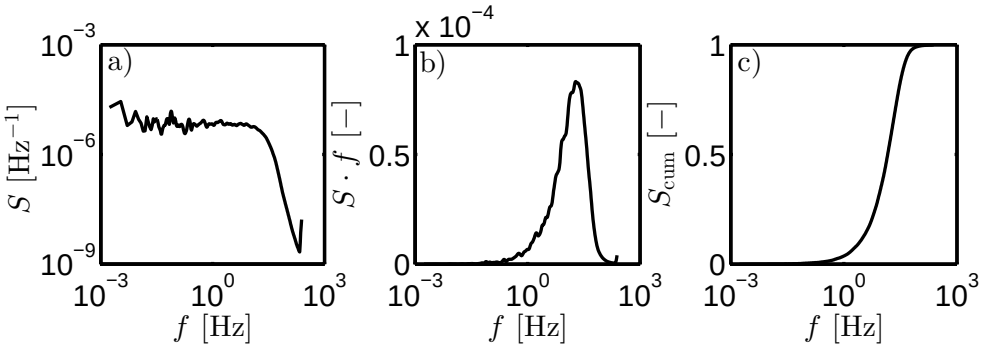

Figure 2.2: Power spectra of the scintillometer signal visualized as (a) loglog representation, (b) semi-log representation using $S \cdot f$, and (c) semi-log representation using the normalized cumulative spectrum (S_{cum}).

where $x(t)$ is the value of x at time t, $x(t + \Delta t)$ is the value of x at time $t + \Delta t$, and U is the horizontal wind speed.

2.2 Power spectra

In this thesis spectral analysis of the scintillometer signal is used to obtain $\overline{U_{\perp}}$. Note that a scintillometer is sensitive to fluctuations in the refractive index (n), thus the scintillation spectra is influenced by the structure parameter of n (C_{n^2}). In the following sections the spectral visualizations used in this thesis are discussed as are the two methods by which the power spectra are calculated (fast Fourier transformation and wavelet transformation).

2.2.1 Spectral visualizations

A power spectrum shows how much the duration of a certain eddy (time-scale) or a certain eddy size (length-scale) contribute to the measured signal, making a power spectrum a valuable tool when measuring turbulence. There are different ways by which a power spectrum can be visualized. In this thesis three visualizations of the scintillation spectra are used, which are shown in Fig. 2.2.

Figure 2.2a depicts a loglog-representation, which has the benefit of showing the inertial sub-range as a linear line, as stated by Eq. 2.1. Figure 2.2b shows $S \cdot f$ on the y-axis against f on a logarithmic x-axis, where the height of the spectrum is proportional to the contribution of the total variance in the signal. Therefore,

one can immediately spot the frequency that contributes most to the variance of the signal. The cumulative spectrum is plotted in Fig. 2.2, which is obtained by the integrating the spectrum depicted in Fig. 2.2b from low to high frequencies (i.e., from left to right). In this thesis the cumulative spectrum is normalized by dividing the cumulative spectrum by the total variance. By normalizing the spectrum, the height is no longer influenced by the value of C_{n^2}.

2.2.2 Fast Fourier transform

A Fourier transform enables users to convert a signal in time to a signal in frequency (or signal in space to a signal in wavenumber). The base function of a Fourier transformation is a sine wave. A range of periods, and thereby different frequencies, are given to the sine wave to calculate the contribution of each frequency to the measurement signal. The Fourier transformation ($F(f)$) is given by:

$$F(f) = \frac{1}{2\pi} \int_0^\infty x(t) e^{ift} dt \tag{2.5}$$

The spectral density ($S(f)$) then follows from:

$$S(f) = \frac{1}{f_{\text{meas}} N} |FF(f)|^2, \tag{2.6}$$

where N is the amount of data points and $FF(f)$ is $F(f)$ folded around the Nyquist frequency ($\frac{1}{2} f_{\text{meas}}$). The total variance of a signal is given by integrating $S(f)$ over all frequencies.

A fast Fourier transformation (FFT) assumes that there is no trend in the measured data (i.e., there is no jump in the data between the beginning and the end of the time series). Therefore, before applying the FFT the linear trend is removed from the signal, as depicted in Fig. 2.3.

When using an FFT the resulting $S(f)$ tends to show scatter especially at high frequencies (as shown in Fig. 2.4a). In order to minimize the scatter, $S(f)$ is smoothed. The smoothing procedure follows Hartogensis (2006); each point in the scintillation spectra weighted by a fixed number of neighboring points using a bell-shaped function. The result of smoothing a spectrum is shown in Fig. 2.4b.

2.2.3 Wavelet transform

A wavelet transformation enables users to convert a time signal to a time-frequency domain. Unlike the Fourier transformation, the wavelet transformation therefore also provides local information about spectral characteristics. A wavelet ($\Psi_0(\eta)$) is a

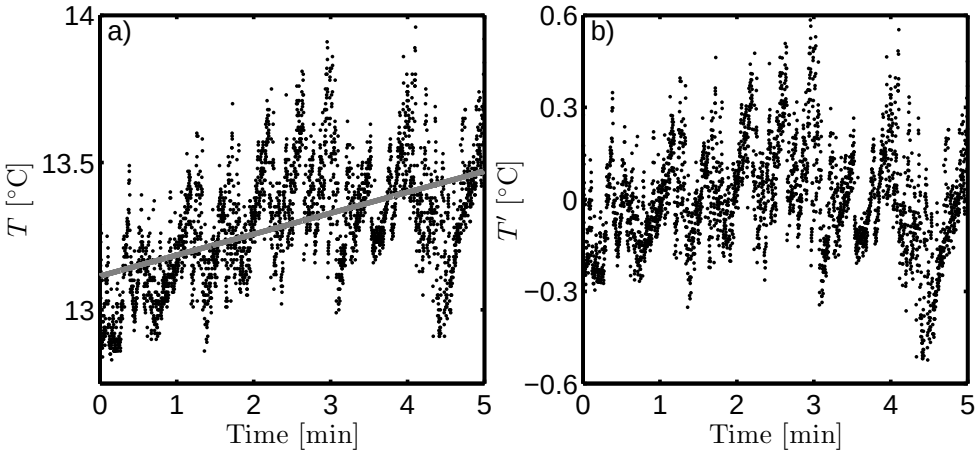

Figure 2.3: (a) Temperature (T) signal with a linear trend, indicated by the grey line. (b) Temperature fluctuations (T') after removing the trend and the mean of the T signal.

generalized local base function, that depends on a non-dimensional time parameter (η). The mean of $\Psi_0(\eta)$ is zero and it is localized in both space and time (Farge, 1992). A wavelet can be stretched in both frequency and time, making it possible to adapt to the entire time-frequency domain, which narrows when focusing on high-frequency signals. This domain widens when focused on the low-frequency ones (Lau & Weng, 1995).

Different types of wavelets exist (e.g., Morlet wavelet, Mexican hat wavelet, Paul wavelet). Although the choice of the wavelet should not influence the result of a true physical signal, in reality the best results are achieved when the wavelet used resembles the form of the signal (Lau & Weng, 1995). In Chapter 3 of this thesis, a Paul wavelet is used. The Paul wavelet is defined as (Torrence & Compo, 1998):

$$\Psi_0(\eta) = \frac{2^m i^m m!}{\sqrt{\pi(2m)!}}(1 - i\eta)^{-(m+1)}, \tag{2.7}$$

where m is the order of the wavelet. In this thesis a 6-th order Paul wavelet is used (see Fig. 2.5a). The best results of the crosswind were obtained when using this wavelet (not shown in this thesis), though the results were not influenced significantly by choosing a different wavelet.

The wavelet transform ($W_n(s)$) of a quantity x_n is defined by (Torrence & Compo,

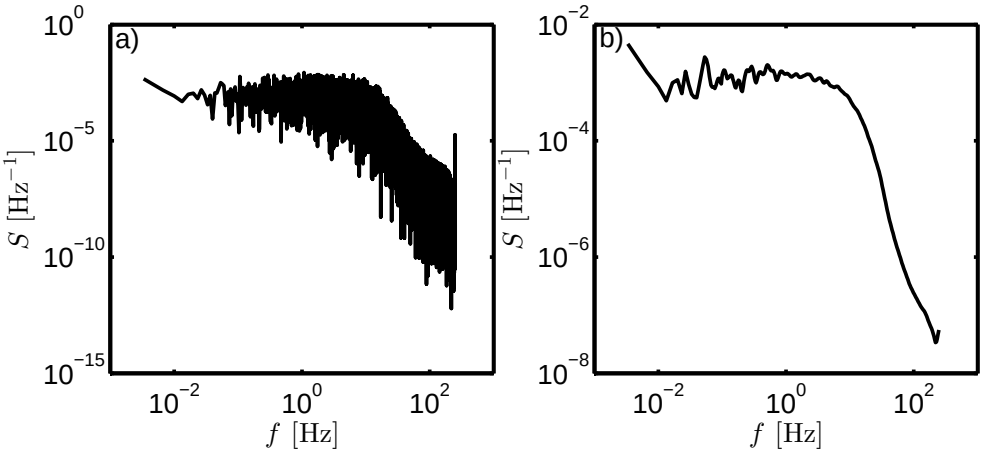

Figure 2.4: Power spectra obtained using fast Fourier transformation of a 500 Hz scintillation signal (a) without smoothing and (b) with smoothing.

1998):

$$W_n(s) = \sum_{n'=0}^{N-1} x_{n'} \widehat{\Psi^*} \left[\frac{(n'-n)\delta t}{s} \right], \tag{2.8}$$

where n is the localized time index, N is the number of points in the time series, s the wavelet scale, and $\widehat{\Psi^*}$ is the complex conjugate (denoted by *) of the normalized wavelet (denoted by $\widehat{\ }$). The wavelet needs to be normalized to ensure that its transform can be compared with each other at each wavelet scale. The normalized form of the Paul wavelet is given by (Torrence & Compo, 1998):

$$\widehat{\Psi_0}(s,\omega) = \frac{2^m}{\sqrt{m(2m-1)!}} H(\omega)(s\omega)^m e^{-s\omega}, \tag{2.9}$$

where ω is the frequency window, and $H(\omega)$ is the Heaviside step function which is defined as $H(\omega) = 1$ if $\omega > 0$, and $H(\omega) = 0$, otherwise. The shape of $\widehat{\Psi_0}$ is given in Fig. 2.5b.

In order to obtain the power spectrum from the wavelet transform, the transformation needs to be rescaled with a constant (C_R) given by (Torrence & Compo, 1998):

$$C_\mathrm{R} = \frac{\delta j \delta t^{1/2}}{\Psi_0} = \sum_{j=0}^{J} \frac{\Re\left(\frac{1}{N} \sum_{f_i=0}^{N-1} \widehat{\Psi_*}(s_j \omega_k) \right)}{s_j^{1/2}}, \tag{2.10}$$

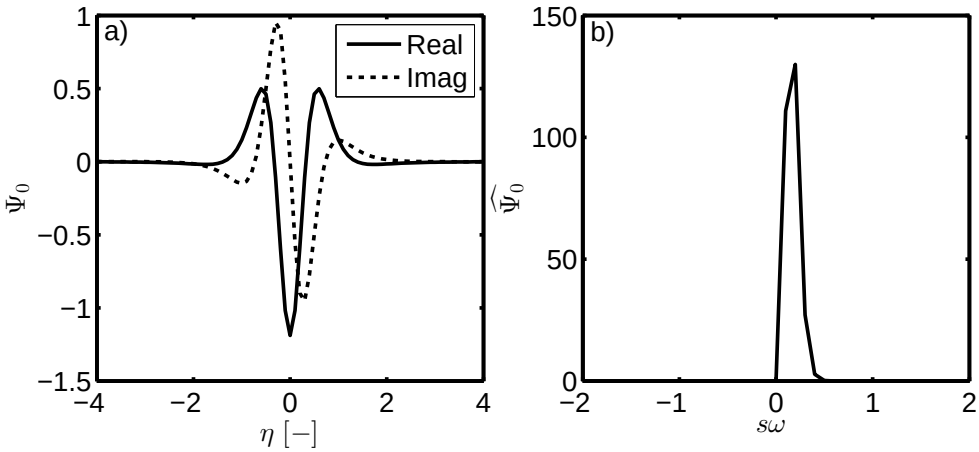

Figure 2.5: (a) The shape of a basis Paul 6 wavelet given the real (solid black line) and imaginary part. (b) Shape of the basis normalized Paul 6 wavelet.

where f_i is the frequency index given by $f_i = 0...N-1$, and j gives s taking

$$s_j = s_0 2^{j\delta j}, \tag{2.11}$$

for $j = 0, 1, ..., J$ and $J = \delta j^{-1} \log_2(N\delta t/s_0)$. The s_0 is the smallest resolvable scale, which should be equivalent to the Fourier period. The power spectrum follows through (Torrence & Compo, 1998)

$$S(f) = \frac{\delta j \delta t}{f C_{\mathrm{R}} N} \sum_{n=0}^{N-1} \sum_{j=0}^{J} \frac{|W_n(s_j)|^2}{s_j}. \tag{2.12}$$

The result of a wavelet transform on a one dimensional time-series is a two-dimensional time-frequency image (Torrence & Compo, 1998), such an image is given in Fig 2.6a. Besides giving insight into which frequency contributes most to the signal a wavelet transform also shows at which time a certain frequency contributes to the signal. Therefore, every line across the x-axis represents one power spectrum, which is shown by the purple line in Fig 2.6b.

2.3 Scintillometry

In the following sections the theoretical framework of scintillometry is given. In this thesis the theoretical models are expressed in terms of variance of the log amplitude

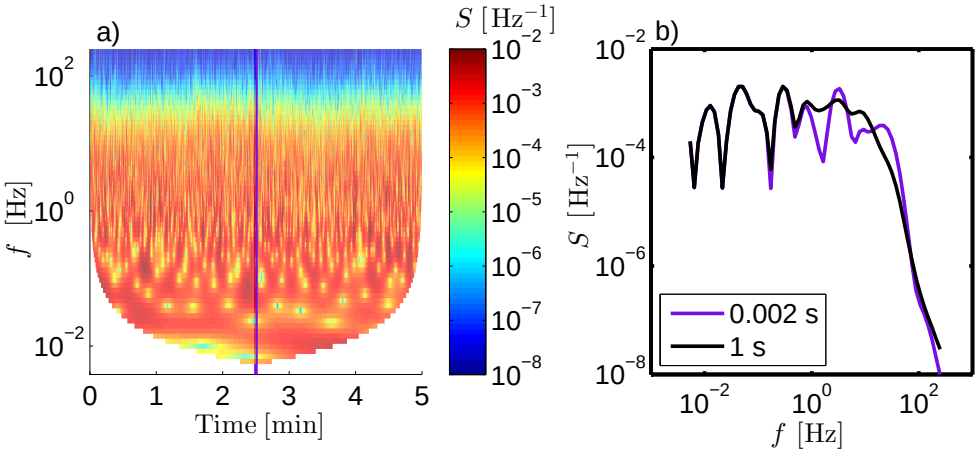

Figure 2.6: (a) Results of a wavelet transformation from the scintillation signal in color $S(f)$ (note plotted on log scale). (b) $S(f)$ calculated with a wavelet transformation for 0.002 s (purple line) and averaged over 1 s (black line).

intensity fluctuations. The models can also be expressed in terms of the variance of the log amplitude of the fluctuations, which is a factor four lower than the intensity fluctuations (intensity is the square of the amplitude). Further, the theoretical models given here are given for a large aperture scintillometer (LAS), since this is the type of scintillometer used in this thesis.

2.3.1 Scintillation (co)variance function

Lawrence *et al.* (1972) describe a theoretical model of the time-lagged covariance function ($C_{12}(\tau)$), where the covariance is given by two spatially separated scintillometers. This model reads after including LAS aperture averaging terms of Wang *et al.* (1981) as:

$$C_{12}(\tau) = 4\pi^2 k^2 \int_0^1 \int_0^\infty K \underbrace{\phi_n(K)}_{\mathrm{I}} \underbrace{\sin^2\left[\frac{K^2 L x(1-x)}{2k}\right] J_0\{K[s(x) - U_\perp(x)\tau]\}}_{\mathrm{II}}$$
$$\underbrace{\left[2\frac{J_1(0.5KD_\mathrm{R}x)}{0.5KD_\mathrm{R}x}\right]^2 \left\{2\frac{J_1[0.5KD_\mathrm{T}(1-x)]}{0.5KD_\mathrm{T}(1-x)}\right\}^2}_{\mathrm{III}} dK dx, \quad (2.13)$$

where τ is the time-lag, k is the wavenumber of the emitted radiation, K is the turbulent spatial wavenumber, L is the scintillometer path length, x is the relative location

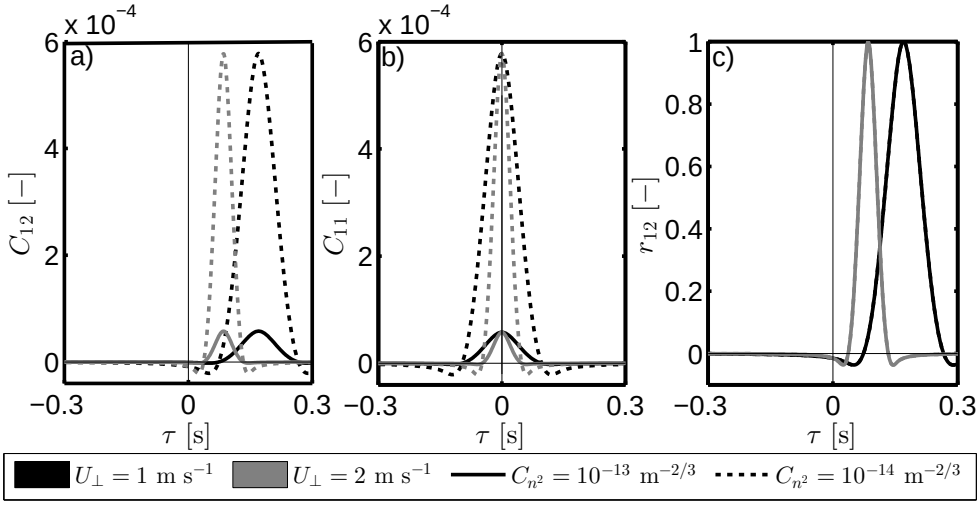

Figure 2.7: (a) Theoretical time-lagged covariance function (C_{12}), (b) theoretical time-lagged variance function (C_{11}), and (c) theoretical time-lagged correlation function (r_{12}) for a dual large-aperture scintillometer given two crosswinds ($U_\perp$, assumed homogeneous along the path) and structure parameters of the refractive index (C_{n^2}) conditions.

on the scintillometer path, J_0 is the zero-order Bessel function, $s(x)$ is the separation between the two scintillometer beams at location x, $U_\perp(x)$ is the crosswind at location x, J_1 is the first-order Bessel function, D_R is the aperture diameter of the receiver, D_T is the aperture diameter of the transmitter, and $\phi_n(K)$ is the three-dimensional spectrum of the refractive index in the inertial range given by (Kolmogorov, 1941):

$$\phi_n(K) = 0.033 C_{n^2} K^{-11/3}, \tag{2.14}$$

where C_{n^2} is the structure parameter of the refractive index. Note that for the Kolmogorov law of a three-dimensional spectrum, as given in Eq. 2.14, the slope of the energy spectrum in the inertial subrange is $K^{-11/3}$, while for a one-dimensional spectrum the slope is $K^{-5/3}$ (see Eq. 2.1).

In the model given by Eq. 2.13 there are three terms contributing to $C_{12}(\tau)$; (I) the turbulence intensity, (II) the wave propagation theory terms, and (III) the aperture-averaging terms.

In Eq. 2.13 all variables are dependent on the type of the scintillometer used and the experimental setup, except for ϕ_n and $U_\perp(x)$ which both change in time. The value of ϕ_n is related to the amount of turbulence in the atmosphere, through Eq.

2.14. The more turbulence, the higher C_{n^2}, the higher ϕ_n, and therefore the higher $C_{12}(\tau)$, as is visualized in Fig. 2.7a. The value of $U_\perp$ determines the location of the peak in C_{12} on the τ-axis. The stronger $U_\perp$ the more the peak in C_{12} moves towards a smaller τ, see Fig. 2.7a. In order to remove the dependence on C_{n^2}, $C_{12}(\tau)$ can be normalized by the variances of the signals (C_{11} and C_{22}), and thereby we end up with the time-lagged correlation function ($r_{12}(\tau)$). It is visible in Fig. 2.7c, that $r_{12}(\tau)$ is as expected not dependent on C_{n^2} (the two lines are not distinguishable from one another), but only on $U_\perp$.

The theoretical values of $C_{11}(\tau)$ are also given by Eq. 2.13 by taking $s(x) = 0$, leading to:

$$C_{11}(\tau) = 4\pi^2 k^2 \int_0^1 \int_0^\infty K\phi_n(K) \sin^2\left[\frac{K^2 Lx(1-x)}{2k}\right] J_0\{-KU_\perp(x)\tau\} \left[2\frac{J_1\big(0.5KD_\mathrm{R}x\big)}{0.5KD_\mathrm{R}x}\right]^2 \left\{2\frac{J_1\big[0.5KD_\mathrm{T}(1-x)\big]}{0.5KD_\mathrm{T}(1-x)}\right\}^2 dKdx. \quad (2.15)$$

The influence of C_{n^2} and $U_\perp$ on $C_{11}(\tau)$ is plotted in Fig. 2.7c. Just as for $C_{12}(\tau)$ the height of $C_{11}(\tau)$ is influenced by C_{n^2} as a consequence; the higher C_{n^2} the higher $C_{11}(\tau)$. The crosswind influences the width of $C_{11}(\tau)$; the higher $U_\perp$ the less wide $C_{11}(\tau)$.

The total variance in a scintillation signal (C_{11}) is given at $\tau = 0$ s (explained in more detail in Section 2.3.3). When the dual-aperture scintillometer has the same aperture diameter for the two receivers and/or two transmitters $C_{11} = C_{22}$. In that way, $r_{12}(\tau)$ can be calculated using $r_{12}(\tau) = \frac{C_{12}(\tau)}{C_{11}}$. In Chapter 4 different methods are explained and tested to retrieve $\overline{U_\perp}$ from $r_{12}(\tau)$.

2.3.2 Scintillation power (co)spectra

Tatarskii (1961) suggested that a theoretical model of the power spectrum ($S_{11}(f)$) is obtained by applying a Fourier transformation to Eq. 2.15 leading to

$$S_{11}(f) = 4\pi^2 k^2 \int_0^\infty \int_0^1 \int_{2\pi f/U_\perp}^\infty K\phi_n(K) \sin^2\left(\frac{K^2 Lx(1-x)}{2k}\right) \cos(2\pi f\tau) \left[(KU_\perp)^2 - (2\pi f)^2\right]^{-1/2} \left(\frac{2J_1(0.5KD_\mathrm{R}x)}{0.5KD_\mathrm{R}x}\right)^2 \left(\frac{2J_1(0.5KD_\mathrm{T}(1-x))}{0.5KD_\mathrm{T}(1-x)}\right)^2 dKdxd\tau, \quad (2.16)$$

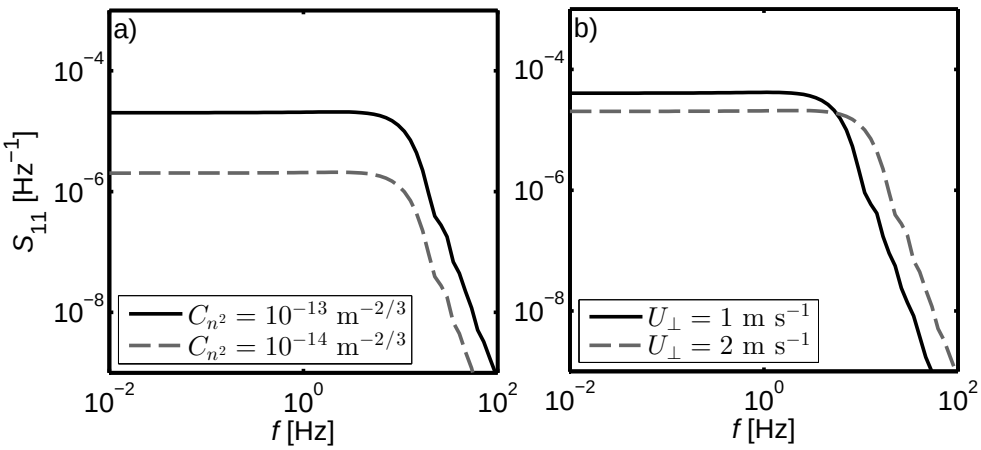

Figure 2.8: Theoretical scintillation spectra using the model of Clifford (1971) given different values of (a) C_{n^2} and (b) $U_\perp$

where f is the frequency for which $S_{11}(f)$ is representative. Similarly to Clifford (1971) integrating Eq. 2.16 over the time-lag gives:

$$S_{11}(f) = 4\pi^2 k^2 \int_0^1 \int_{2\pi f/U_\perp}^{\infty} K\phi_n(K) \sin^2\left(\frac{K^2 L x(1-x)}{2k}\right) \left[(KU_\perp(x))^2 - (2\pi f)^2\right]^{-1/2} \left(\frac{2J_1(0.5KD_\mathrm{R}x)}{0.5KD_\mathrm{R}x}\right)^2 \left(\frac{2J_1(0.5KD_\mathrm{T}(1-x))}{0.5KD_\mathrm{T}(1-x)}\right)^2 dK dx. \tag{2.17}$$

The theoretical model of Clifford (1971), given in Eq. 2.17, assumes that $U_\perp(x)$ is the only phenomenon driving the change in the turbulent eddy field. All of the parameters given in Equation 2.17 depend on the scintillometer setup, except C_{n^2} (note that C_{n^2} influences Eq. 2.17 through ϕ_n given by Eq. 2.14) and $U_\perp$. The influence of these two variables on $S_{11}(f)$ is visible in Fig. 2.8. The value of C_{n^2} influences the height of $S_{11}(f)$, the higher C_{n^2} the higher $S_{11}(f)$. The crosswind influences the location of $S_{11}(f)$ along the frequency axes; the higher $U_\perp$ the more $S_{11}(f)$ shifts to higher frequencies. Note that the slight change in height between the two spectra with different $U_\perp$ is a result of the fact that the area underneath the curve is the same, since C_{n^2} and therefore C_{11} does not change. The shift along the frequency axis scales linearly with $\overline{U_\perp}$, making it possible to obtain $\overline{U_\perp}$ by deriving the location of a characteristic point on the scintillation spectra. More details on how $\overline{U_\perp}$ can be obtained from scintillation spectra are given in Chapter 3 of this thesis.

In a similar way as $S_{11}(f)$, $S_{12}(f)$ can be obtained from Eq. 2.13 by taking $\tau = 0$, leading to:

$$S_{12}(f) = 4\pi^2 k^2 \int_0^1 \int_{2\pi f/U_\perp}^{\infty} K\phi_n(K) \sin^2\left(\frac{K^2 Lx(1-x)}{2k}\right) J_0[Ks(x)]$$
$$\left[(KU_\perp(x))^2 - (2\pi f)^2\right]^{-1/2} \left(\frac{2J_1(0.5KD_\mathrm{R}x)}{0.5KD_\mathrm{R}x}\right)^2 \left(\frac{2J_1(0.5KD_\mathrm{T}(1-x))}{0.5KD_\mathrm{T}(1-x)}\right)^2 dK dx. \tag{2.18}$$

2.3.3 Scintillation (co)variance

The total variance in a scintillation signal can be obtained from Eq. 2.15 and 2.17. From Eq. 2.15 C_{11} is obtained by taking $\tau = 0$ s (making the J_0-term equal to one), and from Eq. 2.17 by integrating over all frequencies. This gives:

$$C_{11} = 4\pi^2 k^2 \int_0^1 \int_0^{\infty} K\phi_n(K) \sin^2\left[\frac{K^2 Lx(1-x)}{2k}\right]$$
$$\left[2\frac{J_1\big(0.5KD_\mathrm{R}x\big)}{0.5KD_\mathrm{R}x}\right]^2 \left\{2\frac{J_1\big[0.5KD_\mathrm{T}(1-x)\big]}{0.5KD_\mathrm{T}(1-x)}\right\}^2 dK dx. \tag{2.19}$$

Note that Eq. 2.19 is no longer dependent on $U_\perp(x)$, and thereby ϕ_n is the only quantity variable in time that introduces changes in C_{11}.

Equation 2.19 can be analytically solved which gives (Wang *et al.*, 1978):

$$C_{11} = 0.893 C_{n^2} D^{-7/3} L^3. \tag{2.20}$$

where D is the aperture diameter of the transmitter and receiver of the scintillometer, which is assumed to be the same. Equation 2.20 can also be obtained from Eq. 2.17, since C_{11} is given by integrating $S_{11}(f)$ over the entire frequency domain.

In scintillometry Eq. 2.20 is often used to obtain C_{n^2} from C_{11} measured by the scintillometer. The resulting C_{n^2} can be used to calculate a path-averaged value of the surface fluxes (among others Green *et al.*, 2001; Meijninger *et al.*, 2002a).

In the same way as C_{11}, C_{12} can be obtained from Eq. 2.13 and Eq. 2.18, which gives:

$$C_{12} = 4\pi^2 k^2 \int_0^1 \int_0^{\infty} K\phi_n(K) \sin^2\left[\frac{K^2 Lx(1-x)}{2k}\right] J_0\{K[s(x)]\}$$
$$\left[2\frac{J_1\big(0.5KD_\mathrm{R}x\big)}{0.5KD_\mathrm{R}x}\right]^2 \left\{2\frac{J_1\big[0.5KD_\mathrm{T}(1-x)\big]}{0.5KD_\mathrm{T}(1-x)}\right\}^2 dK dx. \tag{2.21}$$

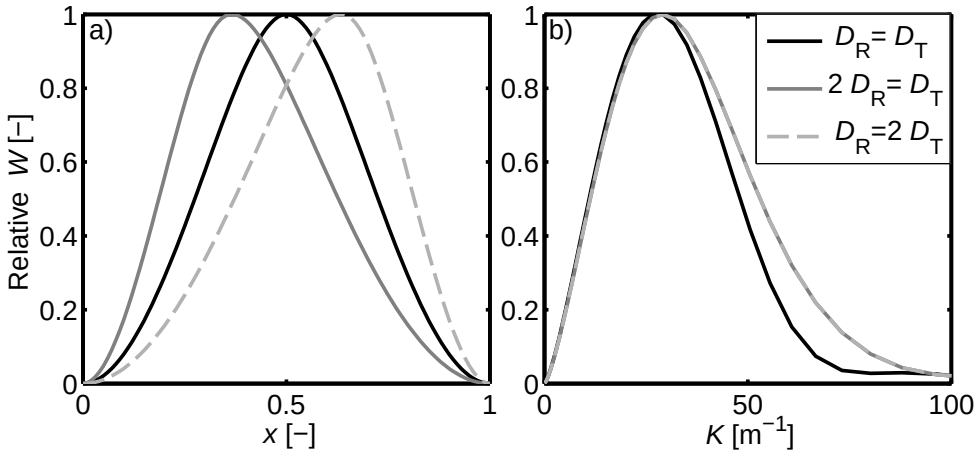

Figure 2.9: (a) Relative W as a function of x, (b) and a function of K. For the black solid line and the light grey dashed line $D_{\mathrm{R}} = 0.15$ m is used, and for the black solid line and dark grey solid line $D_{\mathrm{T}} = 0.15$ m is used.

For Eq. 2.21 no analytical solution exists, since the $J_0[Ks(x)]$ term in Eq. 2.21 is not removed when taking $\tau = 0$ s. Therefore, the value of C_{n^2} cannot be obtained directly from C_{12} measurements.

2.3.4 Scintillation weighting functions

A scintillometer has different sensitivities to changes in the eddy field along its path (i.e., the contributions to the scintillometer signal changes along the scintillometer path). The path-weighting function ($W(x)$) describes the contribution of each point along the path to the scintillation signal. For a LAS it is given by Eq. 2.19, but only integrating over K (Wang *et al.*, 1978). Some examples of $W(x)$ are given in Fig. 2.9, note that $x = 0$ is the location of the transmitter and $x = 1$ the location of the receiver. For a LAS, with $D_{\mathrm{R}} = D_{\mathrm{T}}$, $W(x)$ is bell-shaped, with the highest contributions in the middle of the path (see Fig. 2.9a). The beginning and the end of the scintillometer path do not contribute to the scintillation signal. Therefore, disturbances due to masts where the transmitter and receiver are mounted on do not influence the scintillation signal. If $D_{\mathrm{R}} \neq D_{\mathrm{T}}$, $W(x)$ becomes higher closer to the smallest aperture.

Besides different contributions along the path, a scintillometer is also sensitive to different sizes of eddies (i.e., eddies with different wavenumbers). A rule of thumb is that a scintillometer is most sensitive to eddies which have the size of the aperture

diameter or the Fresnel zone (F, which is given by $\sqrt{L\lambda}$), which ever of the two is largest (Wang *et al.*, 1978). A LAS emits light with a wavelength in the near infrared (for the scintillometer used in this thesis λ =880 nm), measures over a path of 500–5000 m, and has a D ∼10 cm, thus D is larger than F. The eddy-size sensitivity (i.e., K) for a LAS are also given by Eq. 2.19, but only integrating over x from 0 to 1 (Wang *et al.*, 1978). The contributions are depicted in Figure 2.9b. A LAS with an aperture diameter of 0.15 m both for the receiver and transmitter is most sensitive to eddies with a K of around 30 m^{-1}, which is somewhat lower than the aperture diameter ($\frac{2\pi}{0.15}$ = 42 m^{-1}). When $D_{\mathrm{R}} \neq D_{\mathrm{T}}$ eddies with a higher K also contribute more to the scintillometer signal. However, for a LAS it is irrelevant if D_{R} or D_{T} is higher.

3

Crosswind from a Single-Aperture Scintillometer using Spectral techniques

In this study, spectral techniques to obtain crosswinds from a single-large-aperture scintillometer (SLAS) time series are investigated. The crosswind is defined as the wind component perpendicular to a path. A scintillometer obtains a path-averaged estimate of the crosswind. For certain applications this can be advantageous (e.g., monitoring the crosswind along airport runways). The essence of the spectral techniques lies in the fact that the scintillation power spectrum shifts linearly along the frequency domain as a function of the crosswind. Three different algorithms are used, which are called herein the corner frequency (CF), maximum frequency (MF), and the cumulative spectrum (CS) techniques. The algorithms track the frequency shift of a characteristic point in different representations of the scintillation power spectrum. The spectrally derived crosswinds compare well with sonic anemometer estimates. The CS algorithm obtained the best results for the crosswind when compared with the sonic anemometer. However, the MF algorithm was most robust in obtaining the crosswind. Over short time intervals (<1 min) the crosswind can be obtained with the CS algorithm using wavelet instead of fast Fourier transformation to calculate the power scintillation spectra.

This chapter is published as van Dinther *et al.* (2013).

3.1 Introduction

In this study we are interested in obtaining the wind component perpendicular to a path, the so-called crosswind ($U_\perp$), using scintillometer measurements. A scintillometer is a device that consists of a transmitter and receiver. The transmitter and receiver are placed over a path of 0.1-10 km. The transmitter emits a light beam that is refracted in the turbulent atmosphere, causing light intensity fluctuations that are measured by the receiver. The scintillometer is best known for measuring area-averaged surface fluxes (see, e.g., Meijninger *et al.*, 2002a,b; Green *et al.*, 2001; Beyrich *et al.*, 2002), but it can also obtain the path averaged crosswind (among others Lawrence *et al.*, 1972; Heneghan & Ishimaru, 1974; Wang *et al.*, 1981; Poggio *et al.*, 2000).

An application of line-averaged crosswinds obtained from scintillometers is in use at airports. Strong crosswinds along airport runways can introduce a serious safety risk to airplanes taking off or landing. Therefore, takeoffs and landings at airports are restricted by a crosswind limit of 20 kt (10 m s^{-1}). When crosswind limitations are exceeded, the result is often a loss in the available operational capacity of the airport. Airports typically use cup anemometers and wind vanes to measure the crosswind. The disadvantage of these devices is that their measurements are representative of a small part of the runway, while the scintillometer averages the crosswind over a path. Other transportation sectors can also benefit from crosswind measurements. Strong crosswinds on trains can lead to instability and even derailments (Baker *et al.*, 2004). Furthermore, strong crosswinds on bridges can also cause vehicle accidents (Chen & Cai, 2004). We can also envision the use of crosswind measurements for military defense applications. The along-a-line averaging of a scintillometer also makes it suitable for measuring valley winds (Furger *et al.*, 2001).

The application of a scintillometer to measure crosswinds is not new. Lawrence *et al.* (1972) constructed an optical wind sensor that consisted of a dual laser scintillometer, which used the motion of the scintillation pattern to obtain the crosswind. They used the time lag from the covariance function between the two signals to determine the crosswind by assuming Taylor's frozen turbulence hypothesis.

Wang *et al.* (1981) constructed a dual large-aperture scintillometer (DLAS). For this DLAS they presented a technique where the frequency corresponding to the width of the autocovariance function is used to obtain the crosswind. This frequency technique, as they called it, can also be applied to a single-aperture scintillometer. They concluded that the frequency technique obtained the best results for the crosswind. However, the crosswind direction is not known with this technique.

Poggio *et al.* (2000) evaluated three techniques based on the covariance of a DLAS, and three techniques based on characteristic frequencies of intensity fluctuations of a single large-aperture scintillometer (SLAS). They compared the results of these six techniques with cup anemometer and wind vane measurements. They found, contrary to Wang *et al.* (1981), that the covariance techniques obtained better results than the frequency techniques.

The techniques suggested by Lawrence *et al.* (1972), Wang *et al.* (1981), and Poggio *et al.* (2000) all rely on experimental calibration. This calibration is necessary to find the constant describing the relation between the crosswind and the covariance or frequency point used by the technique.

Clifford (1971) developed a theoretical model for the scintillation power spectrum. In this model the crosswind over the scintillometer path determines its position along the frequency axis of the spectrum. Nieveen *et al.* (1998) used the theoretical scintillation spectra of Clifford (1971) to distinguish absorption from refraction fluctuations in the scintillometer signal. They noted that a characteristic frequency point in the spectrum, in their case the upper corner frequency, scales linearly with the crosswind. However, because the focus of Nieveen *et al.* (1998) was not on obtaining the crosswind no validation was made of the crosswind obtained from the upper corner frequency against another measurement instrument.

Ward *et al.* (2011) investigated the consequences of variable, both in space and time, crosswinds along the scintillometer path on the spectrum of the scintillometer signal. They used the theoretical model of Clifford (1971) and found that a variable crosswind causes the spectrum of the scintillometer signal to be altered from the theoretical scintillation spectra of the weighted path-averaged crosswind.

The work presented here is divided into two parts. First, we explore three algorithms to obtain the crosswind from spectra of the signal of an SLAS (Section 3.2 and 3.3), though the techniques are applicable to any single-aperture scintillometer. Second, we evaluate the spectral techniques with experimental data retrieved with a BLS900 (commercially available DLAS, manufactured by Scintec, Rottenburg, Germany) at a flat grassland site in the Netherlands (Section 3.4 and 3.5). Although the BLS900 is a DLAS, we will use it as an SLAS; that is, we will use only one of the two signals.

The three algorithms, used in this study, are named after the characteristic points in different representation in the spectra, notably, the corner frequency (CF), maximum frequency (MF), and cumulative spectrum (CS) algorithms. The characteristic points shift linearly along the frequency domain as a function of $U_{\perp}$. The CF algorithm is similar to the upper corner frequency described by Nieveen *et al.* (1998). The MF algorithm is similar to the fast Fourier transform (FFT) technique described

in Poggio *et al.* (2000). The CS algorithm is a new technique devised to obtain the crosswind from scintillation spectra and uses Ogives described by Oncley *et al.* (1996). Another new aspect in our approach is that we will use the theoretical model for the scintillation spectra of Clifford (1971) to establish the relation between the location of the different characteristic points and the crosswind, unlike the frequency techniques described by Wang *et al.* (1981) and Poggio *et al.* (2000), which relied on experimental calibration.

The scintillation spectra can be obtained from the scintillometer signal intensity measurements using a FFT. However, with the FFT approach we need at least 5 min of data to represent the scintillation spectrum well enough to determine the crosswind from the spectrum (see Section 3.3.4.1). To obtain the crosswind from scintillation spectra for shorter time intervals ($\leq$ 1 minute) we will use spectra calculated with wavelets. The use of FFT and wavelets to obtain scintillation spectra is examined in Section 3.3. The results are discussed in Section 3.5, where we we will also briefly review the result of Scintec's BLS900 output of the crosswind, which uses a dual-aperture approach. In Section 3.6, the conclusions from this study are drawn.

3.2 Theory

A scintillometer sends a monochromatic light beam from a transmitter to a receiver, with the devices typically a few hundred meters to a few kilometers spaced apart. This light is scattered by turbulent eddies, which are advected through the scintillometer path by the wind. Therefore, the amount of scattering varies in time, causing the measured light intensity to fluctuate. Assuming Taylor's frozen turbulence hypothesis, the wind advecting the eddies through the path is the only phenomenon driving the light intensity fluctuations. If this assumption is not valid, the decay of eddies also contributes to the intensity fluctuations.

The amount and strength of the fluctuations of the scintillometer signal, caused by the difference in refractive indices of the eddies, are expressed as the variance of the log of the intensity of the light ($\sigma^2_{\ln I}$). Therefore, the structure parameter of the refractive index (C_{n^2}) is linked to $\sigma^2_{\ln I}$ (Wang *et al.*, 1978; Clifford & Churnside, 1987; Churnside *et al.*, 1988). Here, C_{n^2} is a measure of the spatial variation of the refractive index.

A large-aperture Scintillometer (LAS) is an optical scintillometer that is typically sensitive to eddies the size of its aperture diameter (D) (Wang *et al.*, 1978). In this section we will focus on a LAS. Therefore, the equations given below are valid for

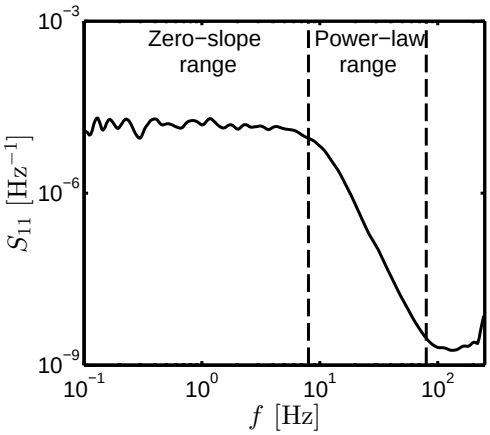

Figure 3.1: Measured scintillation power spectrum with the zero-slope and power-law range indicated.

a LAS. The relationship between $\sigma^2_{\ln I}$ and C_{n^2} for a LAS is given by (Wang *et al.*, 1978):

$$\sigma^2_{\ln I} = 0.89 C_{n^2} D^{-\frac{7}{3}} L^3, \tag{3.1}$$

where L is the pathlength of the scintillometer.

A scintillation spectrum shows how much each frequency contributes to $\sigma^2_{\ln I}$. Figure 3.1 shows a typical measured spectrum of a LAS signal, which has been smoothed. We divided the spectrum into two ranges: the zero-slope range and the power-law range. These two ranges are perceptible by their slopes. The slope in the zero-slope range is, as the name already suggests, zero. For a LAS the slope in the power-law range is $-\frac{12}{3}$. At low frequencies the slope of the spectrum is fluctuating (Fig. 3.1), which is caused by the fact that these points are determined from only a few data points. Integrating the spectrum over all frequencies results in $\sigma^2_{\ln I}$.

Clifford (1971) describes a theoretical model, based on earlier work of Tatarskii (1961), that represents the spectrum of intensity fluctuations measured by a scintillometer for spherical waves. Wang *et al.* (1978) added terms to include the spatially incoherent transmitting and receiving optics in the theoretical model (i.e., the step from a point source to a finite aperture). The theoretical power spectrum ($S_{11}(f)$)

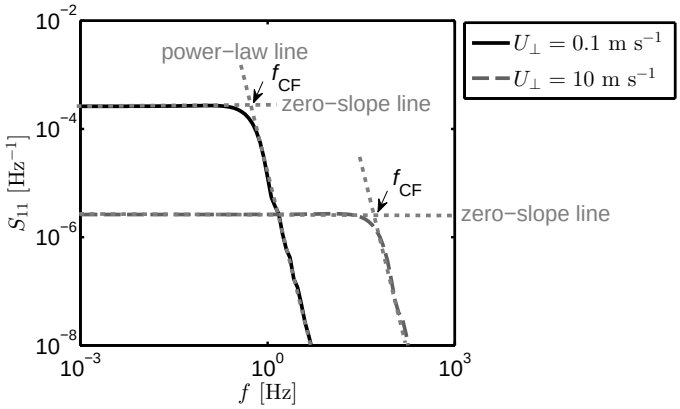

Figure 3.2: Theoretical scintillation spectra with a crosswind of 0.1 m s^{-1} (solid black line) and 10 m s^{-1} (dashed grey line) in loglog representation. The zero-slope line and power-law line are indicated for both crosswinds, as is the corner frequency (f_{CF}).

for a LAS is then defined by (Nieveen *et al.*, 1998):

$$S_{11}(f) = 16\pi^2 k^2 \int_0^1 \int_{2\pi f/U_\perp}^{\infty} K\phi_n(K) \sin^2\left(\frac{K^2 Lx(1-x)}{2k}\right) \left[(KU_\perp)^2 - (2\pi f)^2\right]^{-1/2} \left(\frac{2J_1(0.5KD_{\mathrm{R}}x)}{0.5KD_{\mathrm{R}}x}\right)^2 \left(\frac{2J_1(0.5KD_{\mathrm{T}}(1-x))}{0.5KD_{\mathrm{T}}(1-x)}\right)^2 dK dx, \quad (3.2)$$

where f is the frequency, k is the wavenumber of the emitted radiation, K is the turbulent spatial wavenumber, x is the relative location on the path, J_1 is the first-order Bessel function, D_{R} is the aperture diameter of the receiver, D_{T} is the aperture diameter of the transmitter, and $\phi_n(K)$ is the three-dimensional spectrum of the refractive index in the inertial range given by (Kolmogorov, 1941)

$$\Phi_n(K) = 0.033 C_{n^2} K^{-11/3}. \quad (3.3)$$

For a given scintillometer setup, all variables except $U_\perp$ and C_{n^2} are constant in Eq. 3.2. Therefore, these two variables influence the location of the spectrum, but when they are constant along the path, they do not alter the shape of the spectrum. Here, C_{n^2} determines the height of the spectrum, since it is proportional to $\sigma^2_{\ln I}$ (see Eq. 3.1). In addition, $U_\perp$ influences the location of the spectra on the frequency axis, without influencing $\sigma^2_{\ln I}$. In a log-log representation of the spectrum (as in Fig. 3.1) the height of the spectrum is also influenced by $U_\perp$.

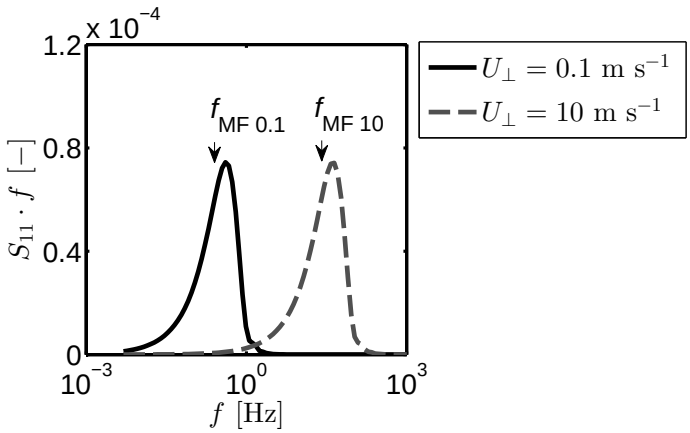

Figure 3.3: Theoretical energy conserved representation of the scintillation spectra with a crosswind of 0.1 m s^{-1} (solid black line) and 10 m s^{-1} (dashed grey line), with the maximum frequencies indicated by f_{MF}.

In Fig. 3.2 the theoretical scintillation power spectra are plotted with crosswinds of 0.1 and 10 m s^{-1}. From Fig. 3.2 it is apparent that a stronger crosswind causes the spectrum to shift to higher frequencies (to the right). This relation can be qualitatively explained as follows; the higher the crosswind the faster the eddies are advected through the scintillometer path. The signal intensity fluctuations are not influenced by the crosswind, but the fluctuations will be squeezed in time when the crosswind is higher. Therefore, the higher frequencies contribute more to the variance of the signal when the crosswind is higher. An important feature is that the frequency shift scales linearly with the crosswind; that is, a characteristic point in the spectrum moves linearly across the frequency domain as a function of the crosswind. We will use the theoretical model of Clifford to establish the factor describing the relation between $U_\perp$ and the characteristic frequency point. In this study we used three different characteristic points employing different representations of the scintillation spectrum, which will be discussed in Section 3.3.2.

Although the crosswind and C_{n^2} both influence the spectra, these two quantities do not influence each other, so the crosswind does not change $\sigma^2_{\ln I}$ and vice versa. This is also visible in Fig. 3.3 (semilog representation of the theoretical scintillation spectrum given two different crosswinds), where the area underneath the curve stays the same for the two different crosswinds.

3.3 Method

3.3.1 Determination of scintillation power spectra

3.3.1.1 FFT

To be able to obtain the characteristic frequency points from the FFT spectra, the data were detrended and spectra smoothed following Hartogensis (2006). Smoothing was applied by weighting each point in the scintillation spectrum by a fixed number of neighboring points using a bell-shaped function. The FFT spectra were determined over 10 min data blocks. Consequently, the results we discuss in this study for $U_\perp$ based on FFT spectra represent an average value over 10 min. The shorter the time over which the spectra are determined, the higher the minimum crosswind that can be determined from the spectra (see Section 3.3.4.1). For application at airports, we would like to be able to obtain the crosswinds from scintillometers over reasonably short intervals ($\leq$ 1 min). Therefore, we will investigate the use of wavelets over 5-min time blocks to obtain the spectra for 1-s intervals.

3.3.1.2 Wavelet

A wavelet spectrum, when properly scaled, yields a power spectrum for every data point (Torrence & Compo, 1998). Therefore, with 500-Hz data a spectrum is obtained for every 0.002 s. In this study we obtained the spectra with wavelets over 5-min data blocks. However, for the first and last minute of these data blocks, the 0.002-s spectra at lower frequencies ($<$ 0.1 Hz) are lacking. Therefore, these spectra are not taken into account. To obtain the crosswind over every second, we averaged the 0.002-s spectra obtained by wavelets to 1 s. Due to the fact that 500 spectra were averaged to obtain the 1-s spectra, no additional smoothing was applied.

Different types of wavelets can be used to obtain the spectra. In this study we used the Paul 6 wavelet (Torrence & Compo, 1998). Using another type did not alter the results significantly. This outcome has previously been suggested by Torrence & Compo (1998), who stated that the choice of the wavelet function is not critical for the power spectra.

In Fig. 3.4 the spectrum calculated with FFT and wavelet approach is plotted for the same data series of 5 min. From this figure it is apparent that the FFT and wavelet methods yield similar results.

A disadvantage of wavelets is that considerably more computing power is needed than for an FFT. In this study we will therefore obtain $U_\perp$ from the FFT for the 10-min time intervals for 7 days and obtain $U\perp$ from wavelets for 1-s time intervals for one specific day only.

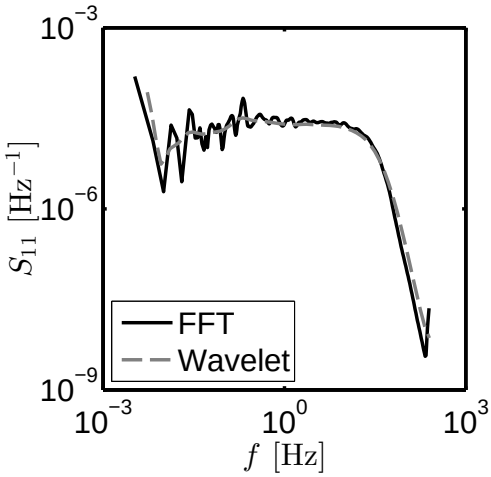

Figure 3.4: Measured scintillation power spectrum calculated with FFT (solid black line) and wavelet (dashed grey line) over 5 minutes of data.

3.3.2 Crosswind algorithms based on scintillation spectra

In this section we will describe the three algorithms we used to obtain the crosswind from measured scintillation spectra: CF, MF, and CS. The algorithms indicate characteristic points in different representations of the spectra that can easily be traced by a computer algorithm. The characteristic points in the spectrum shift linearly along the frequency domain as a function of the crosswind, so:

$$U_{\perp} = C_{\text{algorithm}} D f_{\text{algorithm}}, \tag{3.4}$$

where $C_{\text{algorithm}}$ is a constant depending on the algorithm used and $f_{\text{algorithm}}$ is the frequency corresponding to the characteristic points of the different algorithms. The values of $C_{\text{algorithm}}$ will be determined from the theoretical model for the scintillation spectrum of Clifford (1971). A LAS is sensitive to eddies the size of D. Other types of scintillometers are sensitive to other sizes of eddies (see Table 3.1, adopted from information specified in Nieveen *et al.* (1998)). The spectral techniques can be used for these scintillometers, but D in Eq. 3.4 needs to be replaced by the first Fresnel zone (F) or in the case of a laser scintillometer $C_{\text{algorithm}}$ needs to be determined as a function of f and the inner scale (l_0). The spectral representations used in this study are log-log, semilog, and the cumulative spectrum for the CF, MF, and CS algorithms respectively.

Table 3.1: Types of scintillometer with the abbreviation, eddy size to which they are sensitive, and slope in the power-law range.

Scintillometer type	Abbreviation	Sensitive eddy size	Slope power-law range
Large Aperture	LAS	Aperture diameter	$-\frac{12}{3}$
Micro Wave	MWS	First Fresnel zone	$-\frac{8}{3}$
Laser	-	Inner scale	$-\frac{8}{3}$

3.3.2.1 Corner frequency (CF)

The corner frequency is the inflection point in the log-log representation of the scintillation spectrum. In literature, different definitions of the corner frequency (f_{CF}) are given. Medeiros Filho *et al.* (1983) state that f_{CF} is the point of intersect between the zero-slope line and the power-law line. Nieveen *et al.* (1998) defines f_{CF} as the frequency where the spectrum has dropped to half of the value of that at the zero-slope line. Ward *et al.* (2011) use yet another definition and state that f_{CF} is at the same frequency location as the maximum frequency in the semilog representation of the spectrum. We will use the definition of Medeiros Filho *et al.* (1983), so f_{CF} is the point of intersect between the zero-slope line and the power-law line (see Fig. 3.2). The slope of the power-law line is given in Table 3.1 for different types of scintillometers. From the theoretical spectra in Fig. 3.2 it is apparent that a higher crosswind also lowers the spectra. However, this lowering is only caused by the log-log representation of the spectra. The integral over scintillation spectra, $\sigma^2_{\ln I}$, will not change as a result of a different crosswind.

The algorithm we developed to routinely find f_{CF} from measured spectra consisted of finding the zero-slope line and the power-law line (see Fig. 3.2). To find these lines, a smoothing was applied on the spectra (see Section 3.3.1). After smoothing, the slopes were calculated over four spectral points. From these slopes the variance was calculated over five points. The following criteria were set to determine the zero-slope and the power-law lines:

- The variance had to be below a threshold value, we used 0.15, for four consecutive points.
- The slope of the zero-slope line had to be between -0.3 and 0.3.
- The slope in the power-law line had to be between -3.2 and -4.8.
- At least four consecutive points had to belong to the zero-slope line or power-law line.

Over the points that met the zero-slope line criteria mentioned above, a line was fitted. A line was also fitted through the points that met the power-law line criteria. The intersection between these two lines defines the corner frequency as used in this study. A high-pass filter (HPF) of 0.1 Hz (discussed in more detail in Section 3.3.4.2) on the spectrum was used to make sure absorption did not influence the results. The routine above was also performed on the theoretical spectra to obtain the constant C_{CF} in Eq. 3.4, which was 1.38. This is higher than the 1.25 found by Nieveen *et al.* (1998), but they used a different definition of f_{CF} than we did.

3.3.2.2 Maximum frequency (MF)

The maximum frequency (f_{MF}) is the frequency where the maximum of the energy conserved representation of the scintillation spectrum is located (Fig. 3.3). The routine used to obtain f_{MF} is straightforward and consists of simply determining the maximum of the spectrum (see Fig. 3.3). The constant C_{MF} in Eq. 3.4, obtained from the theoretical model, is 1.59. This value is similar to the 1.63 value found by Ward *et al.* (2011).

The MF algorithm is sensitive to errors when there are unwanted contributions to the scintillation spectra. Therefore, it is advisable to use a HPF and a low-pass filter (LPF) (see Section 3.3.4.2). A HPF of 0.1 Hz and a LPF of 90 Hz were used in this study, with corresponding to $U_{\perp}$ values of 0.024 and 21 m s^{-1}, respectively. The LPF is set to a lower value than is discussed in Section 3.3.4.2, since the MF algorithm is susceptible to noise in the high-frequency domain (>90 Hz), which could give unrealistic high values of the crosswinds. Unlike the other two algorithms, the MF algorithm takes into account one point in the spectrum that is typically not at a high frequency. Therefore, removing the high frequencies with the LPF only influences the results when noise is present in these frequencies.

3.3.2.3 Cumulative spectrum (CS)

The cumulative spectrum, also known as Ogives (Oncley *et al.*, 1996), is obtained by integrating a spectrum from high to low frequencies. However, we integrate the spectrum from low to high frequency (left to right) and normalize the spectra with the variance ($\sigma^2_{\ln I}$). The CS is a new algorithm we propose to obtain $U_{\perp}$ from a scintillation spectrum. Unlike the previously discussed algorithms, the CS algorithm takes into account the complete shape of the spectrum.

We used five frequency points, which corresponded to the following points in the cumulative spectrum: 0.5, 0.6, 0.7, 0.8, and 0.9 (see Fig. 3.5). The constants C_{CS} obtained from the theoretical spectra corresponding to these frequency points are

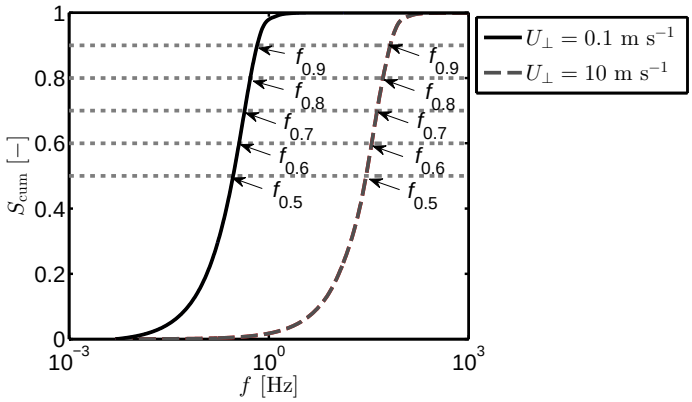

Figure 3.5: Theoretical cumulative scintillation spectra with a crosswind of 0.1 m s^{-1} (solid black line) and 10 m s^{-1} (dashed grey line). The frequencies where the cumulative spectrum is 0.5, 0.6, 0.7, 0.8, and 0.9 are indicated by $f_{0.5}$, $f_{0.6}$, $f_{0.7}$, $f_{0.8}$, and $f_{0.9}$ respectively.

2.31, 1.88, 1.55, 1.27, and 1.00, respectively. The crosswinds obtained, by applying Eq. 3.4, for these five points are averaged to obtain one crosswind per scintillation spectrum.

The CS algorithm is also sensitive to errors due to unwanted contributions to the scintillation spectrum. Therefore, data where the maximum frequency (as stated in Section 3.3.2.2 without the HPF and LPF) was below 0.1 Hz or above 90 Hz were filtered out.

3.3.3 Crosswind algorithm used by SRun

The exact algorithm that SRun, the processing software provided by Scintec, uses to retrieve the crosswind from the BLS900 data is unknown. However, in the manual it is stated that the time-lagged-cross-covariance function is used ($C_{12}(\tau)$). This function is in theory defined by (Clifford, 1971), here added with aperture averaging terms given by (Wang *et al.*, 1978)

$$C_{12}(\tau) = 4\pi^2 k^2 \int_0^1 \int_0^\infty K\phi_n(K) \sin^2\left[\frac{K^2 Lx(1-x)}{2k}\right] J_0\{K[s(x) - U_\perp(x)\tau]\} \left[2\frac{J_1(0.5KD_{\mathrm{R}}x)}{0.5KD_{\mathrm{R}}x}\right]^2 \left\{2\frac{J_1[0.5KD_{\mathrm{T}}(1-x)]}{0.5KD_{\mathrm{T}}(1-x)}\right\}^2 dK dx, \quad (3.5)$$

Table 3.2: Scintillometer set-ups used to calculate the minimum and maximum resolvable crosswind

Scintillometer	D [m]	F [m]	λ [m]	L [m]	l_0 [mm]
LAS	0.15	0.03	$8.8 \cdot 10^{-7}$	1000	7
LAS	0.30	0.03	$8.8 \cdot 10^{-7}$	1000	7
MWS	0.25	6	$1.9 \cdot 10^{-3}$	1900	7
MWS	0.25	10	$1.9 \cdot 10^{-3}$	5300	7
Laser	0.0025	0.01	$6.7 \cdot 10^{-7}$	150	2
Laser	0.0025	0.01	$6.7 \cdot 10^{-7}$	150	7
Laser	0.0025	0.01	$6.7 \cdot 10^{-7}$	150	15

where J_0 is the Bessel function of the first kind and zeroth order, τ is the time-lag between the two signals, $s(x)$ is the spacing in between the two apertures as a function of x, D_{R} is the aperture diameter of the receiver, and D_{T} is the aperture diameter of the transmitter. The crosswind is derived from Eq. 3.5 by applying a stepwise deconvolution technique.

3.3.4 Validity of the spectral techniques

For which crosswinds the spectral techniques are valid is determined by the measurement frequency and the record length. The minimum and maximum crosswinds resolvable with different scintillometer setups are discussed in Section 3.3.4.1.

Errors can occur in the crosswind if the scintillation spectra are not obtained correctly. The spectra can be influenced by unwanted contributions to the spectra, a low signal or signal-to-noise ratio, and variability of $U_{\perp}$ along the path. In Sections 3.3.4.2, 3.3.4.3 and 3.3.4.4 the influence these phenomena have on the spectra and how their influence can be minimized are discussed.

3.3.4.1 Minimum and maximum crosswind resolvable with spectral techniques

The minimum crosswind resolvable by the spectral techniques is determined by the sample length taken, while the sample frequency determines the maximum crosswind that can be resolved. The scintillometer type and setup also determine the maximum and minimum crosswinds that are resolvable. In this section five typical scintillometer setups were investigated (see Table 3.2). The theoretical spectrum for laser scintillometers (not given in this paper) also includes the inner scale. Typical values of l_0 range from 2 to 20 mm Hartogensis (2006), we used values of 2, 7, and 15 mm. The theoretical spectra were calculated for the different setups and crosswind values.

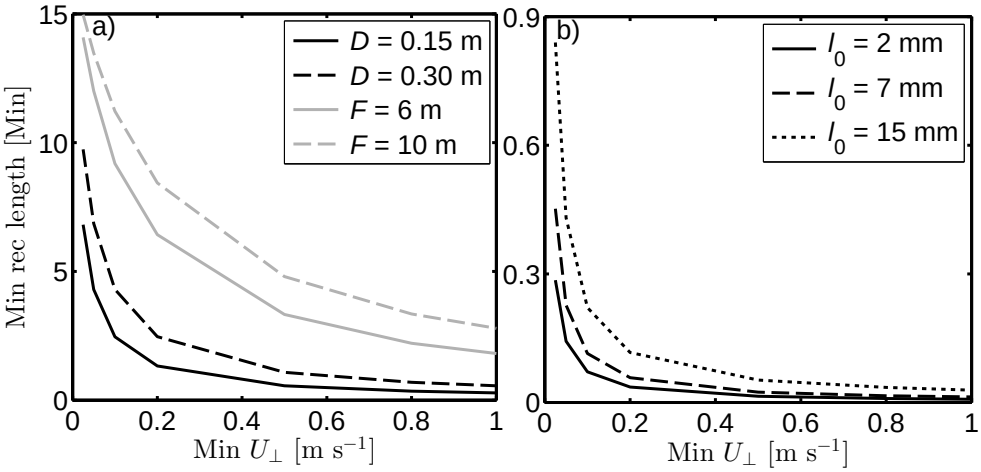

Figure 3.6: Minimum record length necessary to solve at least 1 % of the scintillation spectra for minimum crosswind for different scintillation set-ups (LAS (black in a), MWS (grey in a) and laser scintillometer (black in b)).

We define the minimum sample length by the frequency where the cumulative spectrum was 0.01 (i.e., at least 1 % of the scintillations contributions to the spectra are accounted for). The results for the minimum sample lengths are plotted in Fig. 3.6. Note that the spectra should be determined over blocks of at least 10 times the minimum sample length, since the value of the power spectrum is then represented by at least 10 data points. The lines in Fig. 3.6 are not linear, because the frequencies are converted to minutes. For the BLS900 used in this study (D = 0.15 m), the minimum sample length required to measure crosswinds as low as 0.5 m s^{-1} is 30 s. Therefore, we should determine the scintillation power spectra over data blocks of at least 5 min. For a laser scintillometer the minimum record length necessary to resolve the same minimum crosswind is one order of magnitude lower than that of an LAS and a microwave scintillometer (MWS).

The maximum crosswind resolvable is determined by the crosswind where the sample frequency is located at the 0.99 point of the cumulative spectrum. The results for the maximum crosswind resolvable for a given sample frequency are plotted in Fig. 3.7. The frequency up to which the spectra can be calculated is half of the measurement frequency. For the BLS900 the measurement frequency is 500 Hz and D is 0.15 m. Therefore, the maximum crosswind that can be resolved is 20 m s^{-1}. From Fig. 3.7 it is apparent that the measurement frequency necessary to be able to resolve the same maximum crosswind is lower for an MWS than for an LAS. However,

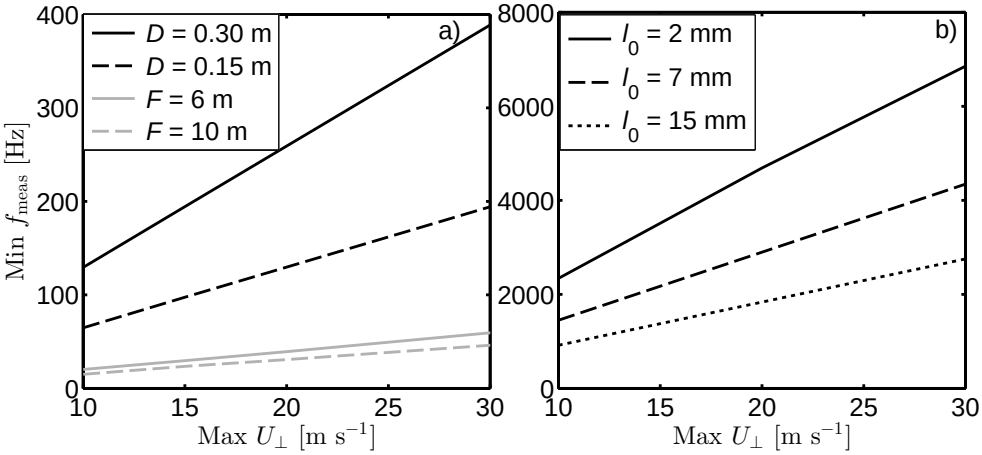

Figure 3.7: Minimum measurement frequency necessary to solve at least 99 % of the scintillation spectra for maximum crosswind for different scintillation set-ups (LAS (black in a), MWS (grey in a) and laser scintillometer (black in b)).

in Fig. 3.7 the slope of an MWS is less steep than that of an LAS, indicating that the scintillation spectra of an MWS shifts less in the frequency domain due the crosswind than for an LAS. Therefore, it is more difficult to distinguish one crosswind from the other with an MWS than an LAS. An MWS is therefore less suitable than an LAS for determining the crosswind using spectral techniques. For the laser scintillometer (Fig. 3.7b) the minimum measurement frequency has to be very high (>2500 Hz) to be able to obtain the crosswind till 30 m s^{-1}. The results of the minimum and maximum resolvable crosswinds vary for different values of l_0. To use the spectral techniques for scintillometers that are sensitive to the eddy sizes of the inner scale, $C_{\mathrm{algorithm}}$ needs to be determined as a function of f and l_0.

3.3.4.2 Unwanted contributions to the scintillation spectra

Fluctuations caused by sources other than scintillations (e.g., absorption, electronic noise, and tower vibrations) can also contribute to $\sigma^2_{\ln I}$, and, thereby, alter the scintillation spectra. Alterations to the spectra can potentially influence the crosswind obtained from them.

Errors due to absorption fluctuations can be circumvented relatively easily, as absorption of an LAS signal occurs at frequencies lower than those associated with refraction (Nieveen *et al.*, 1998). A correctly chosen HPF will suffice. One has to make sure not to set the HPF on a too high frequency since, especially for the CS

Table 3.3: Constants describing the relation between $U_\perp$ and the characteristic frequency point for the three algorithms when the DLAS correction is applied.

Algorithm	Constant
CF	1.24
MF	1.45
$CS_{0.5}$	1.95
$CS_{0.6}$	1.64
$CS_{0.7}$	1.40
$CS_{0.8}$	1.18
$CS_{0.9}$	0.96

algorithm, the complete scintillation spectrum contributing to $\sigma^2_{\ln I}$ is necessary. The lower the crosswind, the greater the contribution of the lower frequencies to $\sigma^2_{\ln I}$, and the more critical the HPF choice becomes. We would like to resolve crosswinds from 0.5 to 20 m s^{-1} using a LAS with a D of 0.15 m. A HPF of 0.1 Hz will suffice in this case.

Electronic noise can also cause unwanted fluctuations in the scintillometer signal. This noise is in general in the high-frequency domain. Therefore, an LPF on frequency can help to eliminate fluctuations caused by noise. For our purposes an LPF of 280 Hz would allow crosswinds up to 20 m s^{-1} to be measured. However, the measurement frequency of the BLS900 is 500 Hz, so the spectral density can be determined till 250 Hz. Therefore, a LPF cannot be applied on our scintillometer data.

Unwanted contributions to the fluctuations of the scintillometer signal can be removed relatively easily for a DLAS. Absorption fluctuations are nearly identical for the two beams, since the homogeneities have a spatial scale on the order of the path-length. For electronic noise and tower vibrations we also expect the fluctuations to be nearly identical for the two signals, though this is not necessarily the case and also depends upon the scintillometer setup. Therefore, we propose a new method for eliminating the unwanted contributions to the spectra by subtracting the cospectra of two signals from one of the spectra. However, due to this subtraction the theoretical scintillation spectrum is slightly altered, which alters the constants of the algorithm describing the relation between the crosswind and the characteristic frequency point. This alteration implies that it is not only the unwanted contributions to the scintillation spectra that are eliminated, but also part of the scintillation contribution is removed as well eliminated. In Table 3.3 the values of the constants are given for a DLAS with correction where the two apertures are spaced 17 cm apart (as is the case for a BLS900 of Scintec).

3.3.4.3 Scintillometer signal threshold and signal-to-noise ratio

The scintillometer intensity signal (I) drops drastically when it is foggy. The light emitted by the transmitter is spread under large angles due to the fog particles; therefore, only a small portion or even none of the light arrives at the receiver (Earnshaw *et al.*, 1978) resulting in loss of $U_\perp$ data. In general, the wind speed is low during foggy conditions; therefore, this drop in signal will not influence the application at airports. This drop in signal intensity can even be considered to be an advantage, since the light intensity measured by the receiver can be a measure of the visibility along the scintillometer path (Beyrich *et al.*, 2002). Moreover, the visibility along the runway also induces a safety risk for airport operations. In this study, we used an $I_{\text{threshold}}$ of 20 000 ($\frac{2}{3}$ of the clear-sky signal), so data where I was below 20 000 were filtered out. The value of $I_{\text{threshold}}$ is dependent on the scintillometer type and setup used.

A low signal-to-noise ratio (SNR) can result in errors in the crosswind obtained with the spectral techniques. Here, signal does not refer to the mean signal, but to the scintillation signal, $\sigma^2_{\ln I}$. A low SNR, therefore, means that the $\sigma^2_{\ln I}$ due to scintillations is relatively small in relation to $\sigma^2_{\ln I}$ because of noise from any source. Low SNR mainly occurs in near-neutral conditions. In these conditions the sensible heat flux is small, which is associated with small fluctuations in the refractive index (De Bruin *et al.*, 2002). Therefore, the spectrum of the scintillometer signal is less reliable in near-neutral conditions.

3.3.4.4 Variability of $U_\perp$ along the scintillometer path

In practice the height of a scintillometer is often not constant along its path (Hartogensis *et al.*, 2003). In the appendix we specify how the effective height of the crosswind measurement can be obtained. A varying beam height influences the scintillation spectra, since the crosswind and C_{n^2} will vary along a slant scintillometer path due to their vertical profile.

In the appendix we investigate the influence of a slant path on $U_\perp$ obtained with the CF, MF, and CS algorithms. From the results we conclude that measuring along slant paths only results in a small error in the crosswind obtained by the CF and CS algorithm. Even when the scintillometer path is very slanted (from 2 to 100 m) the error for these two methods is less than 4 %. For the MF algorithm the error in the crosswind is somewhat bigger (up to 8 %). This larger error is caused by the fact that this algorithm focuses on one specific frequency (the maximum frequency), while the other two algorithms take the overall shape of the spectrum into account.

Although a slant path does not influence the results of $U_\perp$ substantially, a strong variability of $U_\perp$ along the path might do so. Ward *et al.* (2011) investigated the influence of a non-uniform crosswind on the scintillation spectra. They found that under extreme conditions where the crosswind on one half of the path was substantially different (≥ 2 m s^{-1}) from that on the other half of the path, the scintillation spectrum was a combination of two spectra of the two crosswinds. For the MF algorithm this combined spectrum will exhibit two peaks. Therefore, the crosswind obtained with the MF algorithm will be representative of only half of the path, that with the lowest crosswind. The CF and CS algorithms take into account the general shape of the spectrum, which probably will result in a better average of the crosswind along the path. That the CF and CS algorithms obtain a better average of the crosswind under variable wind conditions is visible in the appendix, where the error for these two algorithms for a variable crosswind due to a slant path is lower than that of the MF algorithm. Therefore, a wind gust for example at an airport runway will leave a trace in the scintillation spectrum, while a point measurement can miss this fine structure. However, the amplitude of the gust remains unknown with scintillometer measurements, since it depends on where in the scintillometer path the gust is located, due to the path weighting.

Variability of the wind along the scintillometer path can be an issue affecting the accuracy of the crosswind determined with the spectral techniques, but variability in time can also be an issue. The scintillation spectrum is determined over a certain time interval. If the crosswind changes during that time interval, the scintillation spectrum will be influenced by the different crosswinds. Therefore, it is advisable not to take the time intervals too long (>10 min), to ensure as much as possible a stable wind regime.

3.4 Experimental set-up

The data studied in this paper were collected at the meteorological site at the Haarweg, Wageningen, the Netherlands from 13 to 19 May 2010 (DOY 133 until 139). This site is a flat, homogeneous grassland. An aerial photo of the experimental setup is presented in Fig. 3.8.

We deployed a boundary layer scintillometer (BLS900, Manufacturer Scintec, Rottenburg, Germany). The BLS900 was installed at a height of 3.53 m with a pathlength of 426 m. The geographical orientation of the BLS900 was 338° N. We stored the raw 500-Hz intensity signal from the fitted processing unit (running SRun software version 1.07 from Scintec). The BLS900 is a DLAS; it has two transmitters and one receiver with aperture diameters of 15 cm. Even though the BLS900 is a DLAS, we

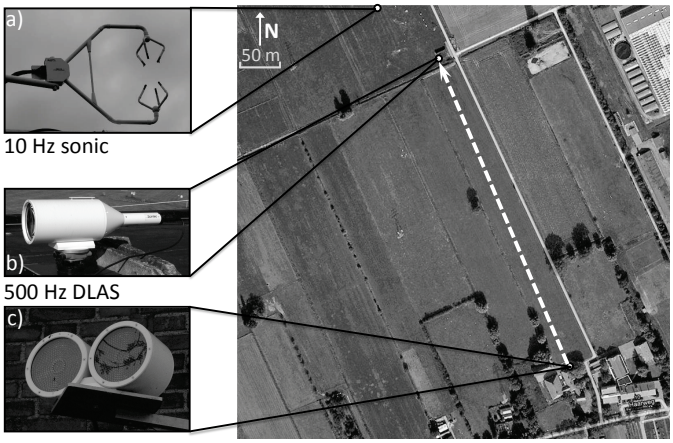

Figure 3.8: Aerial photo (Google Maps) of the experimental set-up, with (a) sonic anemometer, (b) receiver of the BLS900, and (c) transmitters of the BLS900 indicated. The path of the scintillometer is indicated with the dotted white line.

will use it as an SLAS; that is, we will use only one of the two signals in our study. However, we will shortly discuss the results of the crosswind given by SRun.

The output of the BLS900 was validated against a CSAT3 sonic anemometer manufactured by Campbell Scientific (Logan, Utah, United States of America), which was also located at the meteorological site at the Haarweg. The sonic anemometer was not located in the center of the scintillometer path, but at a distance of roughly 300 m from its center. Assuming a homogeneous wind field, this should not result in a substantial difference in wind speeds measured by the BLS900 and the sonic anemometer, given the short distance between the scintillometer and the sonic anemometer and the relatively short scintillometer path. The sonic anemometer was installed at a height of 3.44 m and sampled at 10 Hz. The wind components measured by the sonic anemometer were aligned with the flow using a planar fit correction (Wilczak *et al.*, 2001) and the horizontal wind components were then used to calculate the wind perpendicular on the scintillometer path. The spectral techniques obtain the absolute crosswind; that is, the sign of the crosswind is unknown. Therefore, the crosswind from the SLAS was compared to the absolute value of the crosswind from the sonic.

In Fig. 3.9 the wind measurements (speed and direction) of the sonic anemometer during the measurement period are plotted. In stable conditions during nighttime the 2-m wind speed was suppressed and therefore relatively low (in general < 2 m s^{-1}).

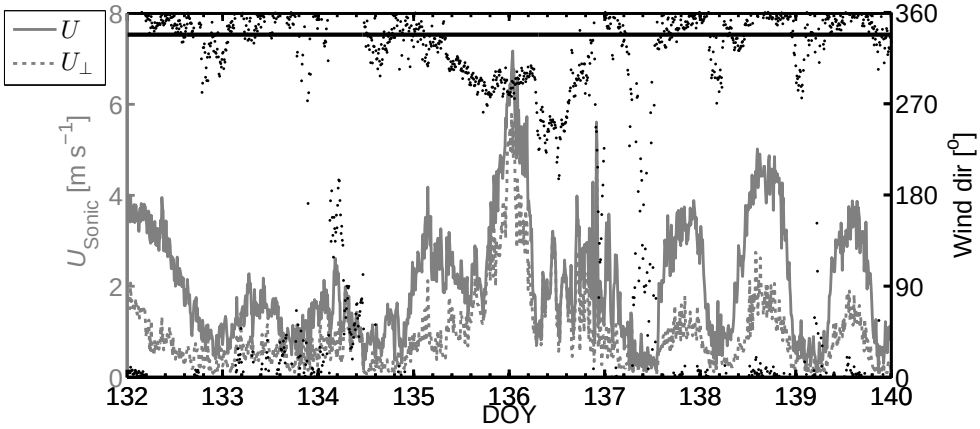

Figure 3.9: Wind conditions on the Haarweg from DOY 133 till 140, with horizontal wind speed (grey solid line) and crosswind on the scintillometer path (grey dotted line) from the sonic anemometer on the left y-axis, and wind direction of the sonic anemometer (black dots) on the right y-axis, the orientation of the scintillometer path is given as a black line.

In unstable conditions during day time the wind speed is in general higher with a maximum of 7 m s^{-1} on DOY 136. The wind direction during the measurement period was variable, but mainly from the north-northwest , which was unfortunately not very perpendicular to the scintillometer path, resulting in an average $U_\perp$ of 1 m s^{-1}.

3.5 Results and discussion

In this section, results of the spectral techniques are compared to sonic anemometer estimated crosswinds. In Section 3.5.1 the results obtained from FFT spectra are discussed, and the absorption correction (using two apertures) is briefly covered. In Section 3.5.2 results obtained from wavelet spectra are presented. In Section 3.5.3 the results of Scintec's BLS900 algorithm, using a dual aperture approach, are discussed.

3.5.1 Crosswinds from FFT spectra

In Fig. 3.10 typical measured FFT spectra calculated over a 10 minute time interval are shown for the spectral techniques used in this study. The measured scintillation spectra in Fig. 3.10 have the same shape as the theoretical scintillometer spectra (see Fig. 3.2, 3.3 and 3.5).

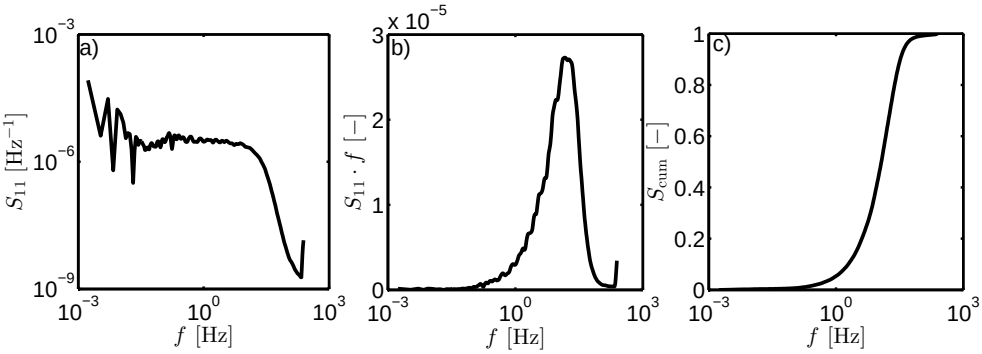

Figure 3.10: Measured scintillation spectrum plotted as (a) loglog representation used by CF algorithm, (b) semilog representation used by the MF algorithm, and (c) cumulative spectrum used by CS algorithm for DOY 136 at 12:00 UTC.

Table 3.4: Regression equations, R^2, and RMSE for $U_{\perp\mathrm{SLAS}}$ with $U_{\perp\mathrm{Sonic}}$ for CF, MF, and CS algorithm with different filters.

Algorithm	Filter	Regression eq.	R^2	RMSE [m s^{-1}]	N [%]
CF	HPF	$y = 0.95x + 0.23$	0.81	0.50	80
MF	HPF & LPF	$y = 0.83x + 0.14$	0.70	0.56	83
CS	$90 < f_{\mathrm{MF}} < 0.1$	$y = 0.95x + 0.22$	0.87	0.41	75
	$U_{\mathrm{CS}} < 0.5$	$y = 0.93x + 0.26$	0.85	0.43	64

In Fig. 3.11, scatter plots are given of the crosswind measured by the sonic anemometer ($U_{\perp\mathrm{Sonic}}$) against crosswind determined with the BLS900 (used as a SLAS - $U_{\perp\mathrm{SLAS}}$) for the three algorithms obtained from FFT spectra over 10 minute time intervals. The points are color coded with SNR. The noise level was determined in the field as the standard deviation of the light intensity measured by the receiver when the transmitter was switched off, which was for our set-up 15 arbitrary units.

Figure 3.11 indicates that all spectral techniques obtained similar results as $U_{\perp\mathrm{Sonic}}$. This similarity between the spectral techniques and the sonic anemometer is also visible in the regression statistics outlined in Table 3.4. In this table the filters applied, linear regression parameters, and corresponding squared of the correlation coefficient (R^2), root mean square error (RMSE), and the percentage of data points left after filtering (N) are shown. In total 1007 data points were considered. However, 17 % of the data were already lost due to $I_{\mathrm{threshold}}$. This high percentage is mainly caused by fog in the morning during this particular measurement period. The fit of $U_{\perp\mathrm{CS}}$

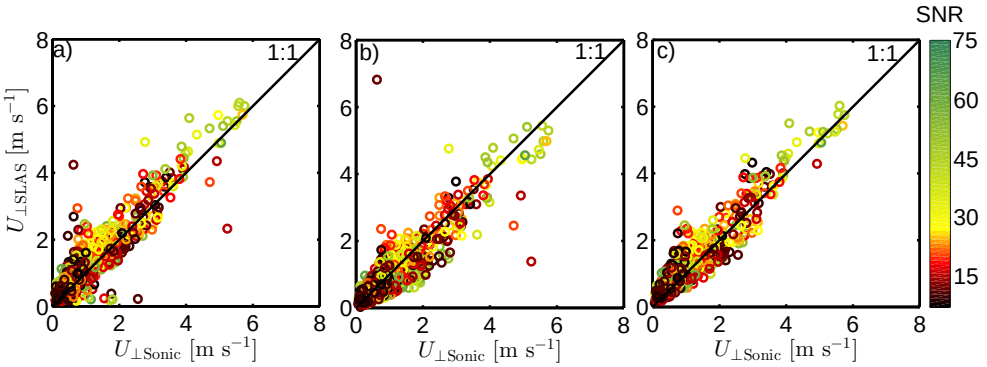

Figure 3.11: Scatter plots of 10 minute crosswinds ($U_{\perp\mathrm{SLAS}}$ against $U_{\perp\mathrm{Sonic}}$) for (a) CF, (b) MF, and (c) CS algorithm colored according to SNR.

with $U_{\perp\mathrm{Sonic}}$ is best, with a regression slope of 0.95 and a RMSE of 0.41 m s^{-1}. However, the number of data points is smallest for this algorithm, with a N of only 75 %. For the CF algorithm the fit with the sonic anemometer is also very good (with a regression slope of 0.95). However, the scatter is somewhat higher than that of the CS algorithm (R^2 of 0.81 in comparison to 0.87, and a RMSE of 0.50 m s^{-1} in comparison to 0.41 m s^{-1}). We assumed that the CS algorithm would not be valid for crosswinds below 0.5 m s^{-1}. However, restricting $U_{\perp CS}$ to values higher than 0.5 m s^{-1} did not improve the results, but did result in an extra loss of data of 11 %. The fit of the MF algorithm with the sonic anemometer is worst of the three spectral techniques (regression slope of 0.83 and RMSE of 0.56 m s^{-1}). On the other hand all the data points, where the I is above $I_{\mathrm{threshold}}$, result in a value for the crosswind. Therefore, the MF algorithm is most robust to determine the crosswind. From Fig. 3.11b it is apparent that some outliers in U_{MF} occur when the SNR is low (< 10).

The CF algorithm has a built-in data quality check, since the zero-slope and power-law range need to be well defined in the scintillation spectrum. Without taking into account $I_{\mathrm{threshold}}$ this built-in quality check resulted in a data loss of 22 % from the total number of points. Most of this data loss (80 %) occurred when I was below $I_{\mathrm{threshold}}$, indicating that a drop in the intensity signal of a scintillometer results in a scintillation spectrum which differs from its theoretical shape. The other 20 % of rejected data can partly be explained by low SNR values. Half (49 %) of this data loss occurs when the SNR is low (<10). Therefore, 90 % of the data lost due to the built-in quality check of the CF algorithm occurs when the signal intensity is low ($<I_{\mathrm{threshold}}$)

or the SNR is low (<10), thereby making this built-in quality check useful to quality control the scintillometer data.

Poggio *et al.* (2000) compared results of the crosswind of DLAS and SLAS approaches with winds of nine cup anemometers placed along the scintillometer path. They found for ten minute averaging intervals correlation coefficients varying from 0.94 to 0.99, which is higher than our correlation coefficients of 0.90, 0.84, and 0.94 for the CF, MF, and CS algorithm respectively. However, this higher correlation coefficient is expectable, since they use a spatially averaged crosswind along the scintillometer path. Furthermore, they only investigated a 12 hour time period where the crosswind was reasonably low varying from 0 to 3 m s^{-1}. In these low wind conditions the correctness of the cup anemometer measurements may be questionable due to their threshold velocity. However, the horizontal wind speed may be significantly higher than the crosswind, but the values of the horizontal wind speeds are not mentioned by Poggio *et al.* (2000).

We also tested the results when the DLAS absorption correction was applied. In theory this correction should eliminate fluctuations of absorption from the scintillation spectra. Therefore, only $I_{\text{threshold}}$ was applied on the data. The results were not as expected. There were some outliers of $U_{\perp}$ calculated with the MF and CS algorithm, which resulted in an overestimation of the crosswind. Apparently, the fluctuations in the intensity signal due to electronic noise were not filtered out by subtracting the co-spectrum of the two signals from the spectrum of one signal. The crosswind of the CF algorithm was more similar to $U_{\perp\text{Sonic}}$, although there was an overestimation of 10 % which was not the case without the absorption correction.

3.5.2 Crosswinds from wavelet spectra

As previously mentioned, the crosswind can be calculated using wavelets for every second. For this analysis we used data of only one day, which was 16 May 2010 (DOY 136). To compare the crosswinds for every second does not make sense, since the clocks of the BLS900 and sonic anemometer were not synchronized to the second and the location of the two instruments was not the same. Therefore, in order to validate the BLS900 with the sonic anemometer crosswinds obtained from 1 second wavelet spectra were averaged over 10 minutes. At least 70 % of the 1 second data had to be present to average over 10 minutes.

Results for the wavelets for DOY 136 are plotted in Fig. 3.12, and regression statistics are shown in Table 3.5. From these we conclude that the three algorithms all yield similar results as the 10 minute FFT spectra for $U_{\perp\text{SLAS}}$ compared to $U_{\perp\text{Sonic}}$ when wavelets are used, although the RMSE is higher for the CF and CS algorithm.

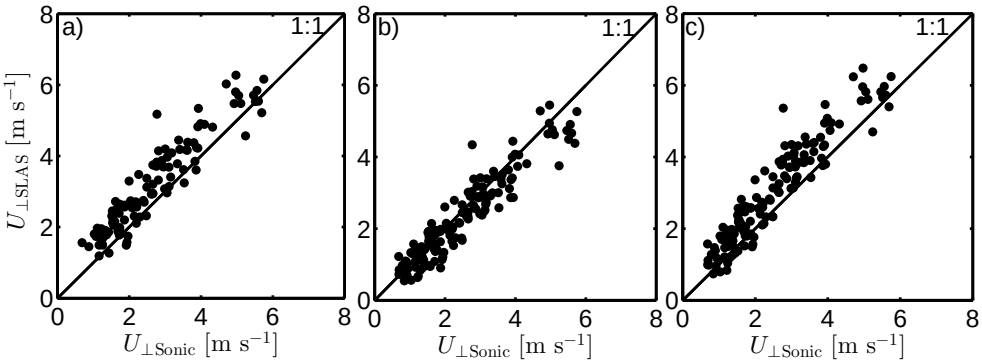

Figure 3.12: Scatter plots of 10 minute crosswinds averages obtained of 1 second wavelets for (a) CF, (b) MF, and (c) CS algorithm, on DOY 136.

Table 3.5: Regression equations, R^2, and RMSE for $U_{\perp\mathrm{SLAS}}$ with $U_{\perp\mathrm{Sonic}}$ for CF, MF, and CS algorithm with wavelets for DOY 136.

Comparison	Algorithm	Regression eq.	R^2	RMSE	N [%]
$U_{\perp\mathrm{SLAS}}$	CF	$y = 0.97x + 0.58$	0.88	0.69	78
vs.	MF	$y = 0.89x + 0.12$	0.89	0.46	100
$U_{\perp\mathrm{Sonic}}$	CS	$y = 1.06x + 0.37$	0.89	0.70	100
$\mathrm{STD}_{U_{\perp\mathrm{SLAS}}}$	CF	$y = 0.82x + 0.30$	0.87	0.21	78
vs.	MF	$y = 0.96x + 0.30$	0.88	0.30	100
$\mathrm{STD}_{U_{\perp\mathrm{Sonic}}}$	CS	$y = 0.58x + 0.17$	0.82	0.21	100

Even though it does not make sense to compare $U_{\perp\mathrm{SLAS}}$ with $U_{\perp\mathrm{Sonic}}$ for every second, the 1 second crosswinds enables us to calculate the standard deviation (STD) for every 10 minute interval which can be compared with each other. It is important to note here that the SLAS measures a path averaged crosswind, while the wind of the sonic anemometer is a point measurement. We therefore expect the standard deviation of $U_{\perp\mathrm{SLAS}}$ to be lower than that of $U_{\perp\mathrm{Sonic}}$, since crosswind extremes are already averaged out by a SLAS because of its path weighting.

We present the results for the 10 minute standard deviations in Fig. 3.13 and the regression statistics are shown in Table 3.5. Unexpectedly, the standard deviations for the CF and MF algorithm are even somewhat overestimated compared to the standard deviations of $U_{\perp\mathrm{Sonic}}$. For the MF algorithm, this is probably caused by the fact that this method takes into account only one point in the spectrum. Only considering one point can introduce extra noise when the location of this point is not well defined, resulting in a larger $\mathrm{STD}_{\mathrm{U}_{\perp\mathrm{MF}}}$. The CF algorithm takes into account multiple points

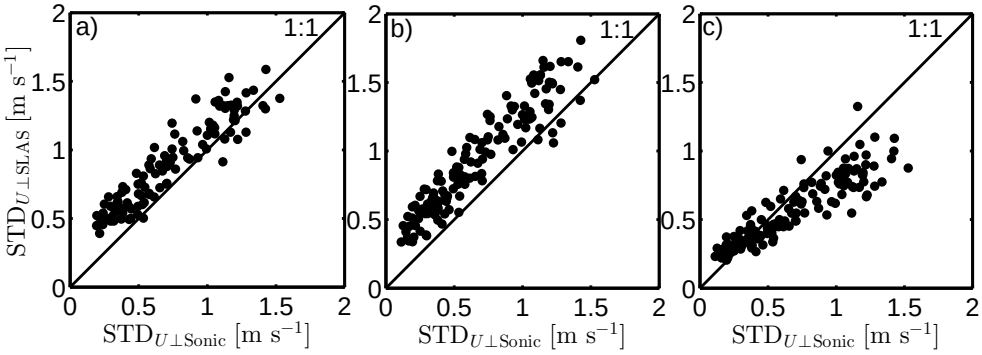

Figure 3.13: Scatter plots of 10 minute standard deviations from 1 second crosswinds from wavelets with on the x-axis $\mathrm{STD}_{U\perp\mathrm{Sonic}}$ and on the y-axis $\mathrm{STD}_{U\perp\mathrm{SLAS}}$ for (a) CF, (b) MF, and (c) CS algorithm, on DOY 136.

in the spectrum, since the corner frequency is determined from the zero-slope line and power-law line. The zero-slope line is located at low frequencies, and the power-law line is located at high frequencies. Therefore, the power-law line can fluctuate for the different 1 second spectra, while the zero-slope line is more fixed, which can cause the overestimation of $\mathrm{STD}_{U_{\perp\mathrm{CF}}}$. The CS algorithm takes into account the whole shape of the spectrum. The standard deviations of the crosswind of this algorithm are, as expected, lower than that of the sonic. This lower standard deviation enhances our trust in this algorithm to obtain the crosswind over short averaging times using wavelets.

3.5.3 Crosswind with Scintec's BLS900 algorithm

Scintec also implemented an algorithm to obtain the crosswind. They use a DLAS approach, which has the advantage that the sign of the crosswind is known. The 10 minute results of this DLAS approach are plotted against $U_{\perp\mathrm{Sonic}}$ in Fig. 3.14, without (a) and with (b) an $I_{\mathrm{threshold}}$. $U_{\perp\mathrm{DLAS}}$ overestimates $U_{\perp\mathrm{Sonic}}$ considerably (regression slope of 1.19). Apparently, there is a difference in time lag between Eq. 3.5 and the measured time lagged cross-covariance. A possible explanation for this difference is longitudinal wind on the scintillometer path. Potvin *et al.* (2005) investigated the effect of longitudinal wind on the scintillation decorrelation times. They found that the longitudinal wind alters the scintillation de-correlation time, since the longitudinal component of the wind constantly introduces new turbulent air at one end of the path and expels turbulent air at the other end of the path. Thereby, the longitudinal

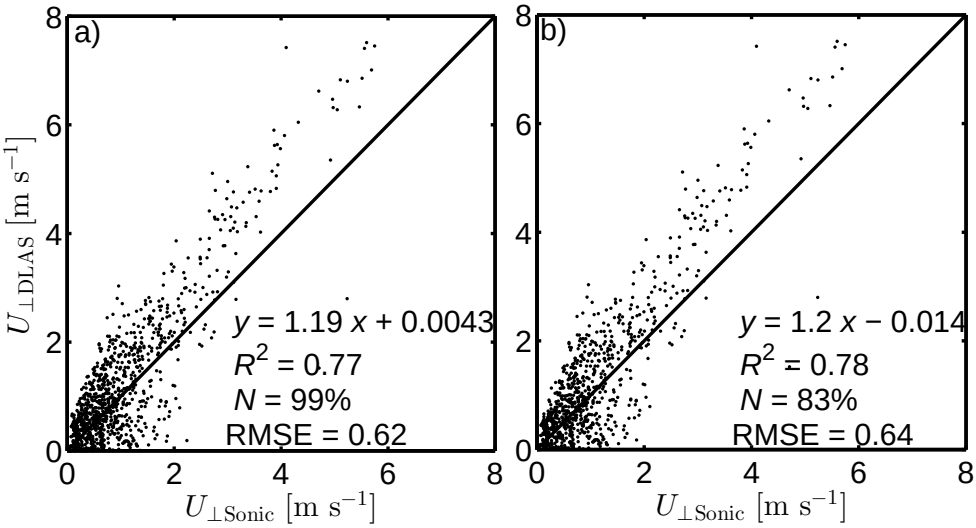

Figure 3.14: Scatter plots of 10 minute averaged crosswinds with on the x-axis $U_{\perp\mathrm{Sonic}}$ and on the y-axis $U_{\perp\mathrm{DLAS}}$ of Scintec's algorithm with corresponding regression equation, R^2, percentage of data, and RMSE (a) without and (b) with an $I_{\mathrm{threshold}}$.

component of the wind causes the scintillation signal to be decorrelated faster (Potvin *et al.*, 2005). The longitudinal wind is not taken into account in Eq. 3.5, but if it causes the signal to decorrelate faster this will also be the case for the cross-signal of the two apertures. Therefore, the time-lag measured will be smaller than the theoretical time-lag, which will cause an overestimation of $U_\perp$. During the experiment the wind was not very perpendicular to the path (Fig. 3.9). Therefore, there is a longitudinal component on the scintillometer path present in the data.

Although there is a reasonable overestimation of $U_{\perp\mathrm{DLAS}}$ the scatter of $U_{\perp\mathrm{DLAS}}$ with $U_{\perp\mathrm{Sonic}}$ is reasonably low (R^2 of 0.77). However, the scatter of $U_{\perp\mathrm{DLAS}}$ with $U_{\perp\mathrm{Sonic}}$ is slightly higher than that of $U_{\perp\mathrm{SLAS}}$ using our three algorithms (R^2 of 0.88 and 0.89). This reasonably low scatter indicates that there is information about the crosswind in the time-lagged covariance function, but SRun's algorithm is not able to obtain an accurate value of the crosswind compared to our sonic.

Although the fit is not very good of Scintec's algorithm with the sonic, the amount of data points is higher for their algorithm than the spectral techniques. Apparently, Scintec's algorithm is able to obtain the crosswind also when the scintillometer signal is low, albeit not the correct value of $U_\perp$. Using $I_{\mathrm{threshold}}$ did not improve the results of Scintec's algorithm.

3.6 Conclusions

We obtained the crosswind from a single large aperture scintillometer (SLAS) signal using three different algorithms, which are based on scintillation spectra without a calibration in the field. These algorithms are: the corner frequency (CF), maximum frequency (MF) and cumulative spectrum (CS). All three algorithms obtained similar results for the crosswind compared with a sonic anemometer, thereby demonstrating that the three algorithms are able to obtain the crosswind from a scintillometer signal. However, some filters needed to be applied to obtain these results. A threshold on the scintillometer intensity signal ($I_{\text{threshold}}$) was applied to all algorithms.

The CF algorithm has the disadvantage that it does not yield a result when the zero-slope and power-law line are not clearly present in the scintillometer spectrum. On the other hand this does serve as a quality check for how well the spectrum of the scintillometer signal is defined. This built-in quality check is why this method achieves good results, also without additional filtering. Applying a high-pass filter did improve the results of the CF algorithm.

The MF algorithm was most robust in obtaining the crosswind, only an additional high-pass filter and low-pass filter were applied. These filters did not result in a loss of data. For the MF algorithm it was also possible to use a less strict $I_{\text{threshold}}$ (5 000 instead of 20 000) and still achieve similar results for the regression statistics as with the strict $I_{\text{threshold}}$ (not shown in this paper). In this study we also investigated a signal-to-noise filter, but in the end we did not apply this filter to our data.

The CS algorithm, a new algorithm we introduced in this paper, achieved the best result. The fit of this algorithm with the sonic anemometer was best, and the root mean square error was smallest. On the other hand, the amount of data points of the CS algorithm was smallest, since all the data points where the maximum frequency was below 0.1 Hz or above 90 Hz were filtered out.

For short time intervals ($\leq$ 1 minute) we recommend using wavelets in combination with the CS algorithm. The ten minute average of crosswinds obtained from wavelet spectra averaged over 1 second showed similar results as the sonic anemometer. We expected the 10 minute standard deviations of the crosswind of the SLAS to be lower than that of the sonic anemometer, since the scintillometer levels out the extremes due to its path averaging. For the CS algorithm this expectation held. However, the standard deviations of the CF and MF algorithm were similar to that of the sonic anemometer. Probable cause for the MF algorithm is that it only uses one point, which can introduce extra noise when the maximum frequency point is not well defined, and thereby lead to a higher standard deviation. For the CF algorithm the high standard deviation of the crosswind is probably caused by strong variation in the

location of the power-law line. Fluctuations in the crosswind and structure parameter of the refractive index will influence the location of the power-law line. Fluctuations in the structure parameter can therefore be misinterpreted as fluctuations in the crosswind, causing an overestimation of the standard deviation of the crosswind of the CF algorithm.

From the results we obtained, we conclude that the CS algorithm is best qualified to obtain crosswinds. First, because it is the algorithm with the best fit and lowest scatter with the sonic anemometer. Second, the results of the wavelet spectra also indicated that this method is best suited to obtain the crosswind over 1 second.

In this study we used the BLS900, a commercial dual large aperture scintillometer (DLAS) manufactured by Scintec (Rottenburg, Germany), which for our analysis we treated as a SLAS. Scintec's SRun software (version 1.07) provides a crosswind estimate. The crosswind obtained from the SRun algorithm showed a clear overestimation of almost 20 %, which is possibly caused by the appreciable longitudinal wind component in our study resulting in a faster decorrelation of the two signals (Potvin *et al.*, 2005). Also the scatter of $U_{\perp\mathrm{DLAS}}$ with $U_{\perp\mathrm{Sonic}}$ was higher than that of $U_{\perp\mathrm{SLAS}}$ with $U_{\perp\mathrm{Sonic}}$. These results imply that our spectral techniques achieve better crosswind results than that of Scintec's SRun algorithm. A disadvantage of the spectral techniques is that the sign of the crosswind is not known. We suggest to use the value of the crosswind of a spectral technique in combination with the sign information from a DLAS algorithm.

More data are needed to test the spectral techniques more extensively, especially, the one minute crosswind obtained from wavelets. This can be achieved by measuring the wind along the scintillometer path with a high amount of cup anemometers and wind vanes. The crosswind on the scintillometer path of these cups and wind vanes can be path weighted according to the scintillometer path weighting, which enables a direct validation of the 1 minute crosswind of the scintillometer.

Acknowledgment

The authors would like to thank Frits Antonysen and Willy Hillen for their assistance with the BLS900 set-up and the reviewers for their valuable comments. This study was funded by Knowledge for Climate project HSMS01.

3A Appendix: Varying scintillometer beam height and crosswind

In practice the height of a scintillometer beam is often not constant along its path (Hartogensis *et al.*, 2003), in which case it is not straightforward for which height the measured crosswind is representative. In this Appendix we will first describe how the effective crosswind height of a scintillometer ($z_{\text{eff_}U\perp}$) can be calculated. Second, we will investigate to what extend the spectral techniques are still applicable for a scintillometer with variable beam height. To facilitate this validity study, we will consider a slant scintillometer path.

3A.1 The effective crosswind height of a scintillometer

To calculate $z_{\text{eff_}U\perp}$ one has to account for its path weighting function and the logarithmic wind profile. We follow the same method as suggested by Hartogensis *et al.* (2003), who obtained the effective height of the structure parameter of temperature of a scintillometer. However, where they use the vertical profile of the structure parameter of temperature we will use the vertical profile of wind.

The path weighting function $W(x)$ of a LAS is given by:

$$W(x) = 16\pi^2 k^2 L \int_0^\infty K\phi_n(K)\sin^2\left[\frac{K^2 Lx(1-x)}{2k}\right]\left[\frac{2J_1(y_1)2J_1(y_2)}{y_1 y_2}\right]^2 dK, \quad \text{(3A.1)}$$

where x is the relative location on the scintillometer path, $J_1(y_1)$ and $J_1(y_2)$ are Bessel functions of the first kind with $y_1 = KD_{\text{R}}x/2$ and $y_2 = KD_{\text{T}}(1-x)/2$.

The crosswind measured by the scintillometer is equal to the integral of the crosswind along the path times its relative weighting function G(x). Therefore we can write:

$$U(z_{\text{eff_}U\perp}) = \int_0^1 U(z(x))G(x)dx, \quad \text{(3A.2)}$$

where $z(x)$ is the height at location x, and $G(x)$ is given by $G(x) = W(x)/\int_0^1 W(x)dx$.

For simplicity we assume that the wind direction is constant over the height range along the scintillometer beam, which allows us to describe the crosswind profile by the wind profile relation of Businger *et al.* (1971):

$$U(z) = \frac{u_*}{\kappa}\left[\ln\left(\frac{z}{z_0}\right) - \Psi_m\left(\frac{z}{L_O}\right) + \Psi_m\left(\frac{z_0}{L_O}\right)\right], \quad \text{(3A.3)}$$

where $U(z)$ is the wind speed at height z, u_* is the friction velocity, κ is the von Kármán constant (0.4), z_0 is the roughness length, L_O is the Obukhov length and

Ψ_m is the integrated stability function of momentum, given by the Businger-Dyer expression (Businger, 1988).

To obtain $z_{\text{eff_}U\perp}$ the expressions of $U(z_{\text{eff_}U\perp})$ and $U(z(x))$ given by Eq. 3A.3 are inserted into Eq. 3A.2. For neutral conditions Ψ_m is zero, which leads to:

$$z_{\text{eff_}U\perp} = z_0 \exp\left[\int_0^1 \ln\left(\frac{z(x)}{z_0}\right) G(x)dx\right] \tag{3A.4}$$

For stable conditions we inserted Ψ_m given by Dyer (1974) into Eq. 3A.2 and 3A.3, which led to the following equation, which can be solved by iteration:

$$\ln\left(\frac{z_{\text{eff_}U\perp}}{z_0}\right) + 5\left(\frac{z_{\text{eff_}U\perp}}{L_O}\right) = \int_0^1 \left[\ln\left(\frac{z(x)}{z_0}\right) + 5\frac{z(x)}{L_O}\right] G(x)dx. \tag{3A.5}$$

For unstable conditions we inserted Ψ_m given by Paulson (1970) leading to:

$$\ln\left(\frac{z_{\text{eff_}U\perp}}{z_0}\right) + 2\ln\left(\frac{1+y\left(\frac{z_{\text{eff_}U\perp}}{L_0}\right)}{2}\right) + \ln\left(\frac{1+y\left(\frac{z_{\text{eff_}U\perp}}{L_0}\right)^2}{2}\right)$$
$$- 2\arctan\left(y\left(\frac{z_{\text{eff_}U\perp}}{L_0}\right)\right) = \int_0^1 \left[\ln\left(\frac{z(x)}{z_0}\right)\right.$$
$$\left. + 2\ln\left(\frac{1+y\left(\frac{z(x)}{L_0}\right)}{2}\right) + \ln\left(\frac{1+y\left(\frac{z(x)}{L_0}\right)^2}{2}\right) - 2\arctan\left(y\left(\frac{z(x)}{L_0}\right)\right)\right] G(x)dx, \tag{3A.6}$$

where y is given by $y\left(\frac{z}{L_0}\right) = (1 - 16\frac{z}{L_O})^{1/4}$.

3A.2 Validity of the spectral techniques to obtain $U_\perp$ with a scintillometer over a slant path

In this section we will investigate the influence of a slant path on the crosswind obtained with the spectral techniques. Scintillation spectra are influenced by a variable $U_\perp$ and C_{n^2} when the scintillometer measures over a slant path, because these quantities are not constant with height. The stability of the atmosphere influences the vertical profile of $U_\perp$ and C_{n^2}. Therefore, we tested the influence of a slant path on the crosswind obtained by the spectral techniques for seven stability regimes. These regimes are outlined in Table 3A.1. For neutral conditions L_O is specified as ∞, but in these conditions the equations are independent of L_O.

The value of $U_\perp$ at a position along the scintillometer beam in relation to the value of $U_\perp$ at a reference height ($U(z_{\text{ref}})$) is given by:

$$U(z(x)) = \frac{\left[\ln\left(\frac{z(x)}{z_0}\right) - \Psi_m\left(\frac{z(x)}{L_O}\right) + \Psi_m\left(\frac{z_0}{L_O}\right)\right]}{\ln\left(\frac{z_{\text{ref}}}{z_0}\right) - \Psi_m\left(\frac{z_{\text{ref}}}{L_O}\right) + \Psi_m\left(\frac{z_0}{L_O}\right)} U(z_{\text{ref}}). \tag{3A.7}$$

Table 3A.1: Stability regimes with corresponding abbreviations and L_O values

Regime	Abbreviation	L_O
Very unstable	vu	-75
Unstable	u	-150
Neutral-unstable	nu	-350
Neutral	n	∞
Neutral-stable	ns	350
Stable	s	120
Very stable	vs	30

We used a reference height of 1 m and a value of $U_\perp$ of 3 m s^{-1}. For stable conditions we used the function of Ψ_m described by Dyer (1974). For unstable conditions we used the function of Ψ_m described by Paulson (1970).

The value of C_{n^2} at a position along the scintillometer beam in relation to the value of C_{n^2} at a reference height is given by:

$$C_{n^2}(z(x)) = \frac{z_{\mathrm{ref}}^{2/3} f_T(\frac{z(x)}{L_O})}{z(x)^{2/3} f_T(\frac{z_{\mathrm{ref}}}{L_O})} C_{n^2}(z_{\mathrm{ref}}), \tag{3A.8}$$

where f_T is the Monin-Obukhov stability function for C_{n^2}. For f_T we used the relations given by Andreas (1989). We used a reference value of C_{n^2} of $1 \cdot 10^{-14}$ m$^{-2/3}$ at 1 m height.

We used measurement heights of the transmitter (z_{T}) and receiver (z_{R}) of 2, 10, 25, 50, and 100 m. The height along the scintillometer path is for $z_{\mathrm{T}} > z_{\mathrm{R}}$ given by $z(x) = \frac{z_{\mathrm{T}} - z_{\mathrm{R}}}{L} x + z_{\mathrm{R}}$ for $z_{\mathrm{T}} < z_{\mathrm{R}}$ it is given by $z(x) = \frac{z_{\mathrm{R}} - z_{\mathrm{T}}}{L} x + z_{\mathrm{T}}$, the value of L does not influence the results.

The values of $U_\perp$ and C_{n^2} were calculated using Eq. 3A.7 and 3A.8 finely discretized (100 points) for the different slant paths. These finely discretized values were averaged to 10 points along the path, since a considerable amount of computation power is needed to calculate the theoretical scintillation spectra. Instead of integrating the theoretical spectra of Eq. 3.2 over the complete scintillometer path the integrations were carried out over 10 parts of the path with the different values of $U_\perp$ and C_{n^2}. These spectra were combined to form one theoretical scintillation spectrum over a slant path, from which $U_\perp$ was obtained using the CF, MF and CS algorithm. We define the error as the percentage difference between $U_\perp$ obtained from the spectra and the weight averaged $U_\perp$.

In Fig. 3A.1 error plots are shown for the CF, MF and CS algorithm over a slant path in very unstable conditions, which had the largest errors from the cases we tested. The error in $U_\perp$ is larger when the scintillometer path is steeper. It is apparent that the MF algorithm shows most sensitivity to a slant path with an error

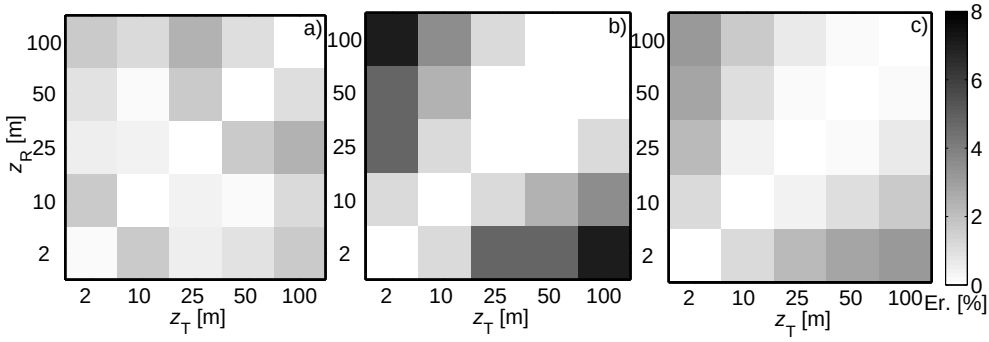

Figure 3A.1: Error in gray scale of $U_\perp$ obtained from the theoretical scintillation spectra with the (a) CF, (b) MF, and (c) CS algorithm over a slant scintillometer path in very unstable conditions.

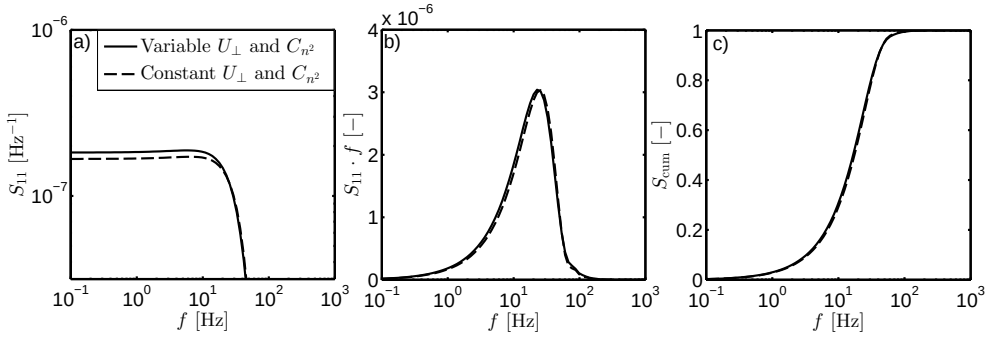

Figure 3A.2: Theoretical scintillation spectra with a variable (due to slant path) and weight averaged $U_\perp$ and C_{n^2} along the scintillometer path used by (a) CF, (b) MF, and (c) CS algorithm in very unstable conditions.

in $U_\perp$ up to 8 %. This algorithm takes into account a single point in a spectrum, which is apparently located at frequencies that are affected by the slant path of a scintillometer.

In Fig. 3A.2 we plotted the theoretical spectra of a very slant path (from 2 to 100 m) together with the theoretical spectra of its weight averaged $U_\perp$ and C_{n^2} in very unstable conditions. The slant path does not influence the scintillation spectra severely. However, the maximum frequency is slightly shifted when the scintillometer measures over a slant path. The CF and CS algorithm are able to obtain $U_\perp$ with a maximum error of only <4 % along a very steep scintillometer path, since the shape of the scintillation spectra did not change severely.

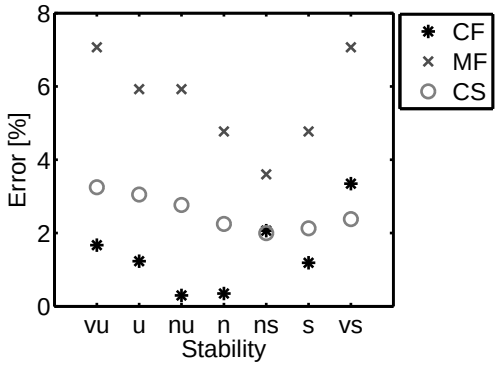

Figure 3A.3: Error in $U_\perp$ with $z_\mathrm{T} = 2$ m and $z_\mathrm{R} = 100$ m in the different stability regimes.

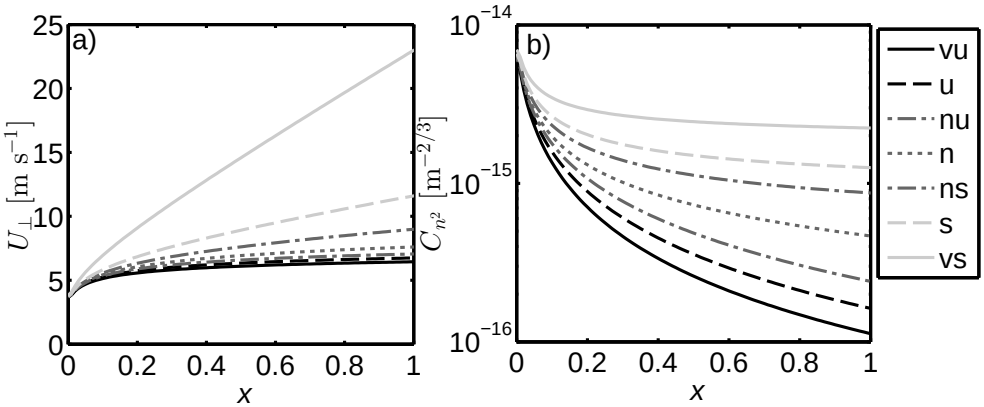

Figure 3A.4: (a) Variable $U_\perp$ and (b) C_{n^2} on a slant scintillometer path ranging from 2 to 100 m in different stability regimes.

In Fig. 3A.3 the error is plotted of a scintillometer with a slant path from 2 to 100 m in the seven stability regimes specified in Table 3A.1. It is apparent that for all the stability regimes the error is largest for the MF algorithm. The errors are smallest in neutral-stable conditions ranging from 2 to 4 %. These small errors are caused by the fact that $U_\perp$ changes most in stable conditions, while C_{n^2} changes most in unstable conditions (see Fig. 3A.4). Therefore, the overall change in spectra due to $U_\perp$ and C_{n^2} is smallest in neutral-stable conditions.

From these results we conclude that the spectral techniques can be used to obtain

$U_\perp$ along a slant scintillometer path. Especially the CF and CS algorithms are suitable to obtain the $U_\perp$ along a slant path. However, the steeper the scintillometer path and the more unstable or stable the atmosphere the larger the error in $U_{\perp\mathrm{SLAS}}$ will be.

4

Using the Time-Lag Correlation Function of Dual-Aperture Scintillometer measurements to Obtain the Crosswind

In this study the crosswind ($U_\perp$) is determined from the time-lag correlation function ($r_{12}(\tau)$) measured by a dual large-aperture scintillometer; $U_\perp$ is defined as the wind component perpendicular to a path- in this case, the scintillometer path. A scintillometer obtains a path-averaged $U_\perp$, which for some applications is an advantage compared to other wind measurement devices. Four methods were used to obtain $U_\perp$; the peak method, the Briggs method, the zero-slope method, and the lookup table method. This last method is a new method introduced in this paper, which obtains $U_\perp$ by comparing $r_{12}(\tau)$ of a measurement to $r_{12}(\tau)$ of a theoretical model. $U_\perp$ values obtained from the scintillometer were validated with sonic anemometer measurements. The best results were obtained by the zero-slope method, for $U_\perp < 2$ m s^{-1} and by the lookup table method for $U_\perp > 2$ m s^{-1}. The Briggs method also showed promising results, but it is not always able to obtain $U_\perp$. The results showed that a high parallel wind component (> 2.5 m s^{-1}) on the scintillometer path can cause an overestimation of $U_\perp$ mainly for low $U_\perp$ values (< 2 m s^{-1}).

This chapter is published as van Dinther & Hartogensis (2014).

4.1 Introduction

The wind component perpendicular to airport runways, the so-called crosswind ($U_\perp$), introduces a safety risk for airplanes landing and taking off. The $U_\perp$ on the runway is in general measured by cup anemometers and wind vanes, which are point measurements. A scintillometer consists of a transmitter and a receiver spaced hundreds of meters to a few kilometers apart and obtains a path-averaged $U_\perp$ (among others Lawrence *et al.*, 1972; Wang *et al.*, 1981; Poggio *et al.*, 2000). The $U_\perp$ measured by a scintillometer can also be applied to increase safety for other transportation sectors, for example, trains (Baker *et al.*, 2004) and bridges (Chen & Cai, 2004). Furger *et al.* (2001) used a scintillometer to measure valley winds. Another application of $U_\perp$ scintillometer measurements is along rivers in urban environment to measure the ventilation of cities (Wood *et al.*, 2013c).

Briggs *et al.* (1950) suggested that $U_\perp$ can be determined from two spatially separated radio wave scintillometers spaced apart. The time lag (τ) between the two scintillation signals is a measure of $U_\perp$. Two methods were suggested by Briggs *et al.* (1950) that use the time-lag correlation function ($r_{12}(\tau)$) to find the following specific τ values. The first is defined as τ where the maximum in $r_{12}(\tau)$ is located. The second is defined as τ where the intersect between $r_{12}(\tau)$ and the time-lagged autocorrelation function ($r_{11}(\tau)$) is located.

Lawrence *et al.* (1972) developed a theoretical scintillation model, that describes $r_{12}(\tau)$ as a function of $U_\perp$ and a given scintillometer setup defined by the path length, separation distance between the two scintillometers, and the aperture size of the scintillometer. This model can be used to find the constants that describe the relation between $U_\perp$ and the specific τ, such as the two described by Briggs *et al.* (1950). Lawrence *et al.* (1972) used their model and the maximum τ suggested by Briggs *et al.* (1950) to obtain $U_\perp$ from a dual-laser scintillometer. They also tested a method that uses the slope of $r_{12}(\tau)$ at zero time lag to obtain $U_\perp$. They claimed that their zero-slope method was also able to obtain $U_\perp$, also when $U_\perp$ was variable along the scintillometer path.

Wang *et al.* (1981) obtained $U_\perp$ from a dual large-aperture scintillometer (DLAS), using the methods suggested by Briggs *et al.* (1950) and Lawrence *et al.* (1972). They also introduced the frequency technique, which uses the width of $r_{11}(\tau)$ to obtain $U_\perp$. This frequency technique uses only one scintillometer signal, and can therefore also obtain $U_\perp$ from single-aperture scintillometer measurements, while methods using $r_{12}(\tau)$ need dual aperture scintillometer measurements. Wang *et al.* (1981) concluded that their frequency technique obtained better results than the methods that use $r_{12}(\tau)$.

More recently Poggio *et al.* (2000) investigated the three $r_{12}(\tau)$ methods and three methods based on the frequency technique by Wang *et al.* (1981). They found that all methods gave similar results. The methods based on the frequency technique, however, tended to give unrealistic high values during the transition periods from day to night and during the nighttime periods. These results are contrary to the results of Wang *et al.* (1981), who found that their frequency technique gave better results than the methods based on $r_{12}(\tau)$.

van Dinther *et al.* (2013) discussed three spectral methods that use scintillation power spectra to obtain $U_\perp$. The theoretical model of the scintillation power spectrum by Clifford (1971) is used by van Dinther *et al.* (2013) for calibration of the spectral methods. A new spectral method introduced in van Dinther *et al.* (2013), the so-called cumulative spectrum method, showed the best results. The spectral methods have the disadvantage of needing a significantly long time interval ($\sim$ 10 min) to obtain the scintillation power spectra and thereby $U_\perp$. The fact that these techniques do not obtain the sign of $U_\perp$ is also a disadvantage. The main advantage of the spectral techniques is that they can be used for a single-aperture scintillometer, which are the most common scintillometers on the market today.

In this study we will focus on the techniques that use $r_{12}(\tau)$ to obtain $U_\perp$. To measure $r_{12}(\tau)$ we use a DLAS manufactured by Scintec (Rottenburg, Germany) that consists of two transmitters spaced 0.17 m apart and one receiver. We will compare four methods: the peak method (Briggs *et al.*, 1950), the Briggs method (Briggs *et al.*, 1950), the zero-slope method (Lawrence *et al.*, 1972), and the lookup table method. This last method is a new method introduced in this paper and obtains $U_\perp$ from the $r_{12}(\tau)$ model of Lawrence *et al.* (1972). In addition we will investigate the influence of the wind component parallel to the scintillometer path ($U_\parallel$) on $r_{12}(\tau)$. The model of Lawrence *et al.* (1972) assumes that there is no influence of $U_\parallel$ on r_{12}, however, in reality $U_\parallel$ also advects eddies into the scintillometer path and thereby has an influence on $r_{12}(\tau)$. In this paper we will investigate the impact of $U_\parallel$ on $U_\perp$ obtained by a DLAS.

4.2 Theory

A scintillometer consists of a transmitter and receiver. The transmitter emits light with a certain wavelength that is scattered by the varying refractive indexes of turbulent eddies in the atmosphere caused by the transport of heat and water vapor. Eddy fields that are advected through the scintillometer path cause intensity fluctuations in the scintillometer signal. Assuming Taylor's frozen turbulence hypothesis the advection of eddies is the only phenomenon causing the light intensity fluctuations.

Another consequence of Taylor's frozen turbulence hypothesis is that for two scintillometers installed next to each other, the intensity fluctuations will be the same except for a time shift between the two signals. The time shift is related to $U_\perp$: the higher $U_\perp$, the faster the eddy field is advected from one scintillometer to the other, so the smaller the time shift between the two signals will be. The time shift can be obtained from the time-lagged correlation function between the two signals ($r_{12}(\tau)$).

Lawrence *et al.* (1972) described a model of the time-lagged covariance function ($C_{12}(\tau)$) of the log-intensity fluctuations for a dual-laser scintillometer. The model as given here is adapted for a large-aperture scintillometer (LAS) by including the aperture averaging terms of an LAS, which are given by Wang *et al.* (1981). The function $C_{12}(\tau)$ then reads

$$C_{12}(\tau) = 16\pi^2 k^2 \int_0^1 \int_0^\infty K\phi_n(K) \sin^2\left[\frac{K^2 Lx(1-x)}{2k}\right] J_0\{K[s(x) - U_\perp \tau]\} \left[2\frac{J_1\big(0.5KD_\mathrm{R}x\big)}{0.5KD_\mathrm{R}x}\right]^2 \left\{2\frac{J_1\big[0.5KD_\mathrm{T}(1-x)\big]}{0.5KD_\mathrm{T}(1-x)}\right\}^2 dK dx, \quad (4.1)$$

where k is the wavenumber of the emitted radiation, K the turbulent spatial wavenumber, L is the scintillometer path length, x is the relative location on the path, J_0 is the zero-order Bessel function, $s(x)$ is the separation distance between the two beams at location x on the path, J_1 is the first-order Bessel function, D_R is the aperture diameter of the receiver, D_T is the aperture diameter of the transmitter, and $\phi_n(K)$ is the three-dimensional spectrum of the refractive index in the inertial range given by (Kolmogorov, 1941)

$$\Phi_n(K) = 0.033 C_{n^2} K^{-11/3}, \quad (4.2)$$

where C_{n^2} is the structure parameter of the refractive index.

For the DLAS used in this study, which has two transmitters and one receiver, $s(x)$ in Equation 4.1 is given by : $s(x) = (1-x)d_\mathrm{T}$, where d_T is the separation distance between the transmitters. The theoretical model of the time-lagged autovariance function ($C_{11}(\tau)$) is given by Equation 4.1 taking $s(x) = 0$.

The correlation coefficient (r_{12}) is defined as the covariance (C_{12}) normalized by the variance of the two signals (C_{11} and C_{22}) - that is, $r_{12} = \frac{C_{12}}{\sqrt{C_{11}C_{22}}}$. The variance of a signal is given by $C_{11}(0)$. Assuming frozen turbulence, the variances of the two beams of a DLAS are identical - that is, $C_{11}(0) = C_{22}(0)$. The $r_{12}(\tau)$ is therefore given by

$$r_{12}(\tau) = \frac{C_{12}(\tau)}{C_{11}(0)}. \quad (4.3)$$

The modeled $r_{12}(\tau)$ is calculated from Equation 4.3 by using $C_{12}(\tau)$ and $C_{11}(0)$ from Equation 4.1.

The measured $r_{12}(\tau)$ is obtained from the signal intensity measurements of a DLAS through

$$r_{12}(\tau) = \frac{\overline{[I_1(t+\tau) - \overline{I_1}][I_2(t) - \overline{I_2}]}}{\sqrt{\overline{[I_1(t+\tau) - \overline{I_1}]^2}\ \overline{[I_2(t) - \overline{I_2}]^2}}}, \tag{4.4}$$

where I_1 is the signal intensity of scintillometer beam 1, I_2 is the signal intensity of scintillometer beam 2, and t is time. The term $r_{11}(\tau)$ follows from Equation 4.4 by replacing I_2 with I_1. Note that for the measured $r_{12}(\tau)$, C_{11} is determined over the time-lagged I_1, while for the modeled $r_{12}(\tau)$, $C_{11}(0)$ is used. Therefore, we assume that $U_\perp$ is constant over the time window used to calculate the measured $r_{12}(\tau)$.

In the appendix three approaches are discussed by which I_1 and I_2 can be shifted with respect to each other to determine $r_{12}(\tau)$. The following time scales are relevant: the time window of I_1 and I_2 used ($\bar{t}$), the total time window taken into account (T), and the time lag (τ) (in Fig. 4A.1 of the appendix the definitions of $\bar{t}$, T, and τ are illustrated in more detail) The best results were achieved with approach 3, which has a constant $\bar{t}$ and a relatively short T. In this study we will, therefore, use this approach to calculate $r_{12}(\tau)$.

Related to the performance of the three time-shift approaches is the length of $\bar{t}$. Fluctuations in the scintillometer signal due to scintillations, so fluctuations in C_{n^2}, are necessary to find a correlation between the DLAS signals which is related to $U_\perp$. For small C_{n^2} (neutral conditions), random errors may deteriorate or become dominant over the DLAS signal, so that $U_\perp$ cannot be obtained reliably from $r_{12}(\tau)$. The length of $\bar{t}$ also determines the influence of random errors: the smaller the $\bar{t}$, the higher the chance to sample a calm C_{n^2} period, which increases the influence of random errors. Therefore, $\bar{t}$ should be sufficient to ensure that there are enough statistics and significant fluctuations in C_{n^2}. In the appendix we tested the influence of the length of $\bar{t}$ on $r_{12}(\tau)$. Although a long $\bar{t}$ (e.g., 1 min) better ensures that there are significant fluctuations in the DLAS signal, for the application at the airport we would like to obtain the crosswind over short time windows ($\sim 10^0$ seconds). An optimum $\bar{t}$ between the two constraints is evaluated in the appendix, which resulted in $\bar{t} = 10$ s.

The $U_\perp$ is positive or negative depending on which side the wind blows into the scintillometer path. In this study we define signal 1 as the signal on the left-hand side, looking from transmitters to receiver. The sign of $U_\perp$ is defined as positive when signal 1 is leading to signal 2 (i.e., $U_\perp$ blows from the left-hand side into the scintillometer path when looking from the transmitters to receiver). The sign of $U_\perp$

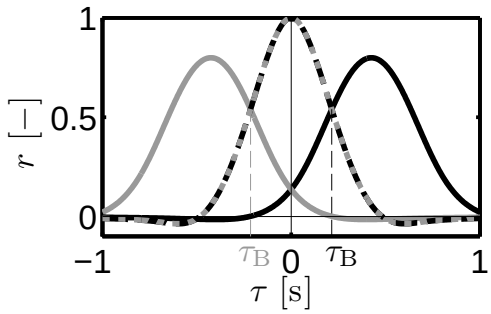

Figure 4.1: Modeled $r_{12}(\tau)$ (solid line) and $r_{11}(\tau)$ (dotted line) for $U_\perp = 0.2$ m s^{-1} (black line) and $U_\perp = -0.2$ m s^{-1} (grey line), with the Briggs time lag (τ_B) indicated.

is defined as negative when signal 1 is trailing signal 2 (i.e., $U_\perp$ blows from the right-hand side into the scintillometer path when looking from the transmitters to receiver). The sign of $U_\perp$ can be obtained from $r_{12}(\tau)$, since it determines whether the peak in $r_{12}(\tau)$ is located at positive or negative τ (see Fig. 4.1). The sign of $U_\perp$ does not influence $r_{11}(\tau)$; therefore, the sign cannot be obtained from $r_{11}(\tau)$ (see Fig. 4.1).

The value of $r_{12}(\tau)$ is determined by $U_\perp(x)$, $s(x)$, and the path-weighting function ($W(x)$). In the following paragraphs we will discuss the effect on $r_{12}(\tau)$ of a varying $U_\perp(x)$ and a varying $s(x)$ along the scintillometer path. We will start by considering a scintillometer with a constant $s(x)$ (0.17 m) and a $U_\perp(x)$ that varies over two halves of the path with 3 and 5 m s^{-1} (see top and middle panels in Fig. 4.2, respectively). This is not a typical example, but it demonstrates the effect of $U_\perp(x)$ on $r_{12}(\tau)$. The middle panels in Fig. 4.2b and Fig. 4.2c indicate that the overall $r_{12}(\tau)$ in this case is clearly a combination of the $r_{12}(\tau)$ of the two halves of the path. The peak of $r_{12}(\tau)$ is, for the varying $U_\perp$, therefore clearly lower (0.62) than the peak of $r_{12}(\tau)$ for a constant $U_\perp$ of 4 m s^{-1} along the scintillometer path (1.0, see middle panels in Fig. 4.2a). The location along the path of the varying $U_\perp$ does not influence the shape of $r_{12}(\tau)$ when $s(x)$ is constant along the path (see middle panels in Fig. 4.2b and 4.2c).

Next we varied $s(x)$, by having two transmitters spaced 0.17 m apart and one receiver (the scintillometer setup used in this study). We kept $U_\perp(x)$ constant along the path with a value of 4 m s^{-1} (see Fig. 4.2a, bottom panel). Although $U_\perp(x)$ is constant, $r_{12}(\tau)$ differs for the two halves of the path. When $s(x)$ is higher (side of the two transmitters) it takes longer for the eddy field to be transported from one signal to the other; therefore, the peak in $r_{12}(\tau)$ is located at a higher τ (light gray line in Fig. 4.2a, bottom panel). The overall $r_{12}(\tau)$ is again a combination of $r_{12}(\tau)$ of the two halves of the path. Varying $s(x)$ along the scintillometer path therefore

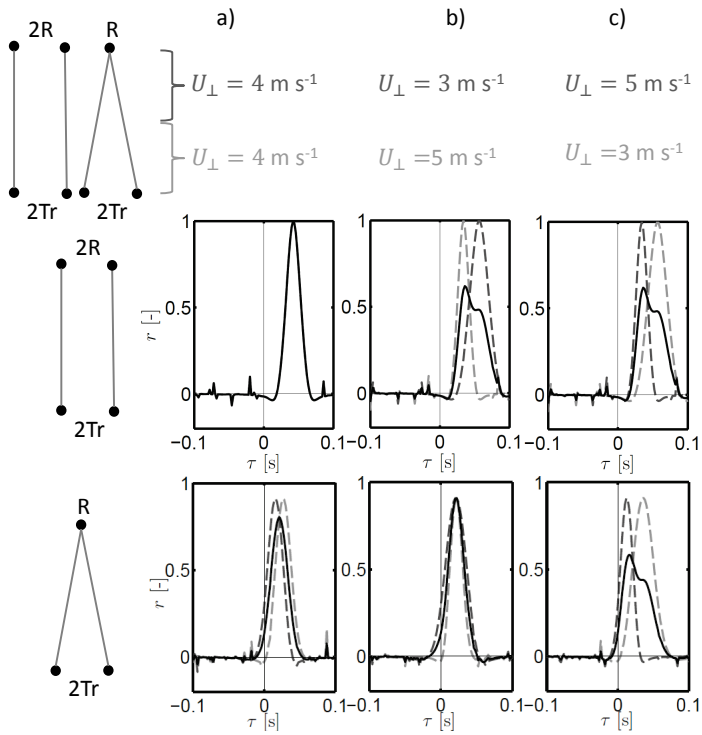

Figure 4.2: Time-lagged correlation function ($r_{12}(\tau)$) for a scintillometer with two transmitters and two receivers (middle panels), and two transmitters spaced 0.17 m apart and one receiver (bottom panels) with different crosswinds ($U_\perp$) along the scintillometer path. Solid black line represents $r_{12}(\tau)$ over the complete scintillometer path, while dashed lines represent $r_{12}(\tau)$ on one-half of the path (light gray near the transmitters and dark gray near the receiver(s)).

results in a lower peak in $r_{12}(\tau)$ (0.80 instead of 1.0) and the peak is located at a lower τ (0.022 instead of 0.042 s). From this example, it can be concluded that the scintillometer setup should be taken into account when $U_\perp$ is determined from $r_{12}(\tau)$.

The results of $r_{12}(\tau)$ for a varying $s(x)$ and a varying $U_\perp(x)$ are plotted in Fig. 4.2b and c (bottom panels). When $s(x)$ varies along the scintillometer path $r_{12}(\tau)$ is affected by where on the scintillometer path the higher $U_\perp$ (5 m s^{-1}) and the lower $U_\perp$ (3 m s^{-1}) are located. In Fig. 4.2b (bottom panel) $r_{12}(\tau)$ of the two halves of the path are similar: a higher $U_\perp$ at the transmitters side causes a peak at a lower τ, while the higher $s(x)$ at the transmitters side causes a peak at higher τ. This results in an overall $r_{12}(\tau)$ that is higher and narrower than $r_{12}(\tau)$ for $U_\perp(x) = 4$ m s^{-1}. In

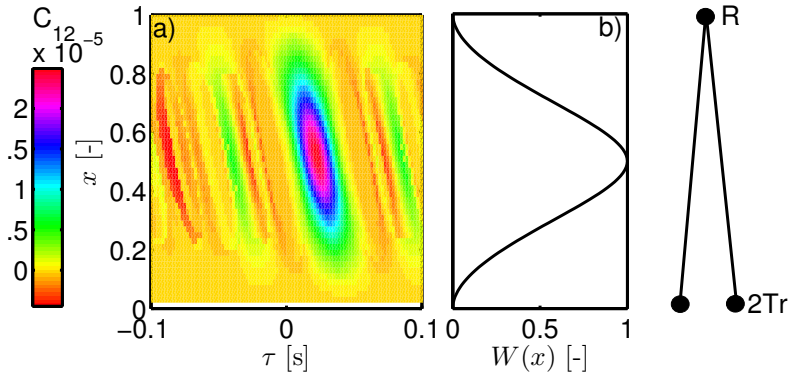

Figure 4.3: (a) Covariance (C_{12}) along the scintillometer path for different time lags (τ), given a scintillometer with two transmitters (2Tr), spaced 0.17 m apart, and one receiver (R). (b) Path weighting ($W(x)$) along the scintillometer path.

Fig. 4.2c (bottom panel) the opposite occurs: $r_{12}(\tau)$ is lower and wider than $r_{12}(\tau)$ for $U_\perp(x) = 4$ m s^{-1}. In reality $U_\perp$ will not vary this extremely over the path; however, this example shows that a variable $U_\perp$ lowers the peak in $r_{12}(\tau)$ and also influences the shape of $r_{12}(\tau)$.

The term $W(x)$ is defined by integrating Equation 4.1 only over K. Fig. 4.3 visualizes $W(x)$ for a scintillometer setup with two transmitters and one receiver, and $D_\mathrm{T} = D_\mathrm{R}$; $W(x)$ is clearly largest in the middle of the scintillometer path, so this area contributes most to the scintillometer signal. Near the transmitters' and receiver's side, $W(x)$ is very low (< 0.1), which is beneficial since the flow can be distorted due to a mast or a building upon which the scintillometer is mounted. The influence of $s(x)$ on the DLAS signal is also visible in Fig. 4.3a, where the higher C_{12} values are clearly seen at higher τ values at the transmitters' side than at the receiver's side. This is as expected, since $s(x)$ is larger at the transmitters side than at the receiver side. We can conclude that $s(x)$, and thereby the scintillometer setup, influences the shape of $r_{12}(\tau)$. Therefore, when calculating $U_\perp$ from $r_{12}(\tau)$ one has the take into account the specific scintillometer setup, concerning $s(x)$ and D.

4.3 Methods

We use four methods to obtain $U_\perp$ from measured $r_{12}(\tau)$; the peak method, the Briggs method, the zero-slope method, and the lookup table method. All methods, except the lookup table method, obtain $U_\perp$ by a typical point in $r_{12}(\tau)$ that is either

multiplied or divided by a constant. In former studies (e.g. Poggio *et al.* (2000)) this constant was determined through experimental calibration, by fitting the constant between measured $U_\perp$ and the typical point in $r_{12}(\tau)$. The measured $U_\perp$ is typically obtained by a series of cup anemometers and wind vanes along the scintillometer path, making the experimental calibration time consuming and expensive. In this study we obtain the constant for the different methods from the model of $r_{12}(\tau)$ (Equation 4.1) where we prescribe $U_\perp$ and a scintillometer setup and calculate the constants from the resulting $r_{12}(\tau)$ values. More details on how these methods obtain $U_\perp$ from $r_{12}(\tau)$ are discussed in this section.

4.3.1 Peak method

Briggs *et al.* (1950) found that in theory $U_\perp$ can be determined from a radio wave scintillometer with two spatially separated receivers and one transmitter. The $U_\perp$ is related to the time lag where the peak in $r_{12}(\tau)$ (τ_P) is located (see Fig. 4.4). The relation between $U_\perp$ and τ_P is given by

$$U_\perp = \frac{\overline{s(x)}}{\tau_\mathrm{P}}, \tag{4.5}$$

where $\overline{s(x)}$ is the average separation distance between the two beams. The sign of $U_\perp$ is obtained for this method by the location of the peak - that is, the sign of τ_P determines the sign of $U_\perp$ (see Fig. 4.4).

Lawrence *et al.* (1972) tested if the peak method of Briggs *et al.* (1950) can be applied to dual-laser scintillometers. They found that this method is also applicable to laser beams but that an overestimation of $U_\perp$ occurred mainly for low values. They attributed this overestimation to the decay of eddies- that is, the violation of Taylor's frozen turbulence hypothesis. When eddies decay in the time interval it takes for an eddy to travel from one light beam to the other light beam, the two signals are no longer correlated. Therefore, violation of Taylor's frozen turbulence hypothesis lowers $r_{12}(\tau)$. For lower $U_\perp$ values, it takes more time to travel from one scintillometer path to the other scintillometer path; therefore, the violation of Taylor's frozen turbulence hypothesis is more likely under these conditions.

4.3.2 Briggs method

Besides the peak method, Briggs *et al.* (1950) also suggested using the time lag where $r_{12}(\tau)$ intersects with $r_{11}(\tau)$, which we will refer to as the Briggs method. This point

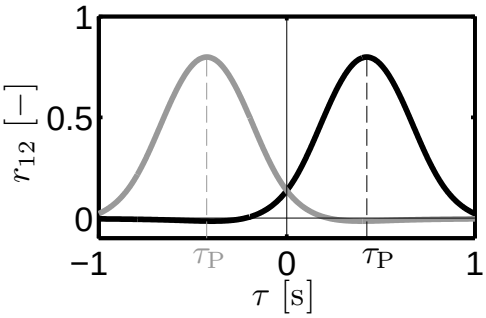

Figure 4.4: Modeled $r_{12}(\tau)$ for $U_\perp = 0.2$ m s^{-1} (black line) and $U_\perp = -0.2$ m s^{-1} (grey line), with the time lag of the peak (τ_P) indicated.

of intersect is indicated in Fig. 4.1 by τ_B and is related to $U_\perp$ following

$$U_\perp = \frac{c_B(\overline{s(x)}, D)}{\tau_B}, \tag{4.6}$$

where c_B is a constant depending on $\overline{s(x)}$ and the aperture diameter (D) of the scintillometer. In literature c_B is assumed constant for a given scintillometer setup (Briggs *et al.*, 1950; Poggio *et al.*, 2000). The modeled $r_{12}(\tau)$ and $r_{11}(\tau)$, however, indicate that c_B is not constant, but varies for different $U_\perp$ values. For our scintillometer setup ($\overline{s(x)}$ is 0.085 m and D is 0.15 m) c_B is 0.043 for 0.2 m s^{-1} $\leq |U_\perp| \leq$ 5 m s^{-1} and c_B increases from 0.043 to 0.049 for 5 m s^{-1} $< |U_\perp| \leq$ 10 m s^{-1} (see Fig. 4.5). This increase makes the Briggs method less suitable to obtain $U_\perp$, especially for high $U_\perp$ values ($>$ 5 m s^{-1}). In this study we used a c_B of 0.043, since $U_\perp$ is rarely above 5 m s^{-1} in our dataset (for the sonic anemometer only 1% of the time for the 10 s data). The value of c_B for a scintillometer setup is dependent on $\overline{s(x)}$ and D; c_B can range for typical scintillometer setups from 0.015 ($\overline{s(x)} = 6.0$ cm and $D = 5.0$ cm) to 0.043 ($\overline{s(x)} = 7.0$ cm and $D = 15.0$ cm).

Another issue with the Briggs method is that when the measured $r_{12}(\tau)$ and $r_{11}(\tau)$ are disturbed in some way, multiple intersects between the two functions can be found. To find τ_B, we therefore only looked for intersects between $\tau = 0$ and $\tau = \tau_P$. For some data there were, however, still multiple intersects or no intersects for $0 \leq \tau_B \leq \tau_P$. To obtain $U_\perp$ for as many situations as possible, we also looked at the results when τ_B was taken as the first or last intersect in case there were multiple intersects. The results of these approaches to obtain τ_B are discussed in Section 4.5.2.

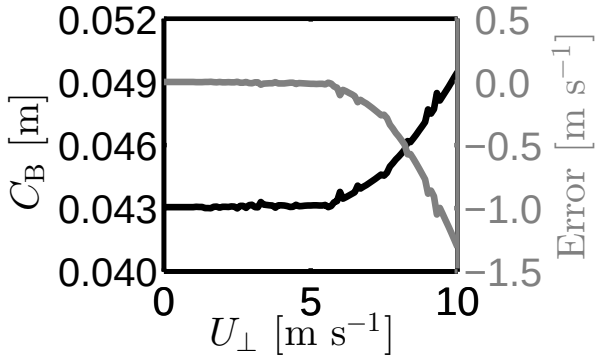

Figure 4.5: Value of the Briggs constant (C_B) (left y axis) given homogeneous $U_\perp$ along the scintillometer path for a scintillometer setup with two transmitters, spaced 0.17 m apart, and one receiver. Error of assuming $C_B = 0.043$ is given in gray on the right y axis.

4.3.3 Zero-slope method

Lawrence *et al.* (1972) suggested that the slope at $\tau = 0$ s of $r_{12}(\tau)$, denoted by S_0, is related to $U_\perp$ (see Fig. 4.6) following

$$U_\perp = c_S(\overline{s(x)}, D) \cdot S_0, \tag{4.7}$$

where c_S is a constant depending on $\overline{s(x)}$ and D.

For our scintillometer setup ($\overline{s(x)}$ is 0.085 m and D is 0.1 m) c_S is -0.165. The value of c_S is highly dependent on $\overline{s(x)}$ and D; it can for typical scintillometer setups range from -0.060 ($\overline{s(x)} = 6.0$ cm and $D = 5.0$ cm) to -8.0 ($\overline{s(x)} = 50$ cm and $D = 30$ cm). The value of c_S also depends on over which τ S_0 is determined. In this study S_0 is determined between τ is -0.1 s and 0.1 s. The sign of $U_\perp$ is defined by the sign of S_0.

4.3.4 Lookup table method

The model of $r_{12}(\tau)$ (Equation 4.1) can, for a given scintillometer setup, be solved for a range of $U_\perp$ and τ, thereby creating a lookup table that can be compared to measured $r_{12}(\tau)$ values. We created a lookup table for -10 m s^{-1} $\leq$ U$_\perp$ $\leq$ 10 m s^{-1} with a resolution of 0.1 m s^{-1} and -1 s $\leq \tau \leq$ 1 s with a resolution of 0.002 s (related to the measurement frequency of 500 Hz) given the scintillometer setup (D and $s(x)$) used in this study (see Section 4.4). The measured $r_{12}(\tau)$, calculated over τ varying from -1 to 1 s, is compared to all the modeled $r_{12}(\tau)$ with different $U_\perp$ values. The

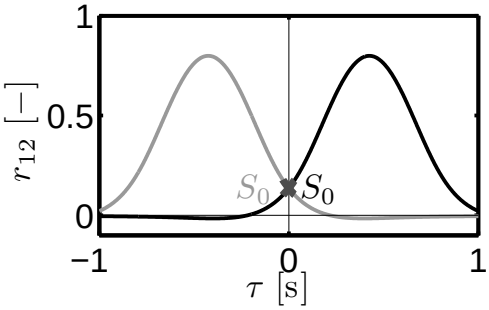

Figure 4.6: Modeled $r_{12}(\tau)$ for $U_\perp = 0.2$ m s^{-1} (black line) and $U_\perp = -0.2 =$ m s^{-1} (grey line), with the zero-slope (S_0) indicated.

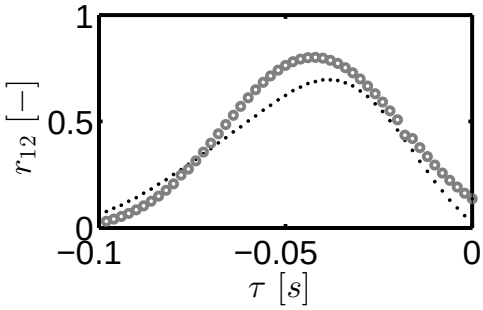

Figure 4.7: Theoretical time-lagged correlation function (black dots) and measured time-lagged correlation function (gray circles) for a $U_\perp$ of -2.0 m s^{-1}.

modeled $r_{12}(\tau)$ that has the best fit with the measured $r_{12}(\tau)$ is the $U_\perp$ representative for the time window over which the measurements were taken. An example is given in Fig. 4.7, where a measured $r_{12}(\tau)$ is plotted along with the theoretical $r_{12}(\tau)$, which has the best fit with the measured $r_{12}(\tau)$. As can be seen in Fig. 4.7, the measured $r_{12}(\tau)$ and the theoretical $r_{12}(\tau)$ are both calculated with a resolution for τ of 0.002 s. The best fit is determined over -1 s $\leq \tau \leq$ 1 s. This fit can be found using different criteria - for example, smallest difference, highest correlation, and smallest root-mean-square error (RMSE). We decided to use the highest correlation to determine the best fit.

Potentially the lookup table method can also be used to investigate the variability of $U_\perp$ along the path. This can be achieved by adding heterogeneous wind fields to the lookup table. It is also possible to incorporate specific path characteristics in

the lookup table (e.g., height variation of the beam along the scintillometer path). However, in this study the scintillometer that was installed is measuring over a short path of only 426 m over a homogeneous grass field. Therefore, strong heterogeneity of $U_\perp$ is unlikely to occur and we created a lookup table for homogeneous wind fields only.

4.4 Experimental setup and data treatment

4.4.1 Experimental setup

The data analyzed in this paper are the same as in van Dinther *et al.* (2013), which was collected at a flat grassland site at the Haarweg, Wageningen, The Netherlands. We will, therefore, only briefly outline the most important aspects of the experimental setup. For more details see van Dinther *et al.* (2013). A Scintec BLS900 measured the scintillation signal with a frequency of 500 Hz over a 426-m path at a height of 3.53 m with an angle relative to north of 338° (see Fig. 8 in van Dinther *et al.* (2013)). The BLS900 is a DLAS with two transmitters (spaced 0.17 m apart) and one receiver, all with an aperture diameter of 0.15 m. As already specified in Section 4.2, $U_\perp$ of the DLAS ($U_{\perp\mathrm{DLAS}}$) is defined positive when, looking from the transmitters' side to the receiver's side, the wind blows from the left side into the scintillometer path. For the scintillometer setup in this study (roughly a south-north orientation), this implies that $U_\perp$ is positive when the wind is blowing from the west, and $U_\perp$ is negative when the wind is blowing from the east.

In this study, $U_{\perp\mathrm{DLAS}}$ is validated with sonic anemometer measurements (CSAT3, Campbell Scientific, Utah). This anemometer measured at a height of 3.44 m, with a frequency of 10 Hz, and it was located roughly 300 m from the middle of the scintillometer path (see Fig. 8 in van Dinther *et al.* (2013)). The wind direction and horizontal wind speed of the sonic anemometer were used to calculate $U_\perp$ on the scintillometer path, which was used for validation.

The DLAS and sonic anemometer measurements ran from 13 to 19 May 2010. The wind directions at the Haarweg during this measurement period according to the sonic anemometer were not very perpendicular to the scintillometer path, with wind directions mainly from the north/northwest (see Fig. 9 in van Dinther *et al.* (2013)). Consequently, the longitudinal wind component is considerable during the measurement period (up to 4 m s^{-1}).

4.4.2 Noise filtering

White noise by, for example, the sensor electronics introduces uncorrelated intensity fluctuations in the scintillometer signal. This noise, therefore, lowers $r_{12}(\tau)$ of the DLAS signal, which affects some of the $U_\perp$ retrieval algorithms. The effect of noise is strongest when the scintillations are weak - that is, conditions where the structure parameter of the refractive index (C_{n^2}) is low. For the peak method, the location of τ_P will not change due to noise; therefore, this method is not susceptible to noise. For the Briggs and zero-slope method, τ_B and S_0 are, however, affected by noise (Wang *et al.*, 1981): S_0 will be lower when the peak in $r_{12}(\tau)$ is reduced due to noise, leading to an underestimation in $U_\perp$; τ_B will be higher when the peak in $r_{12}(\tau)$ is reduced due to noise, also leading to an underestimation in $U_\perp$. We expect that $U_\perp$ of the lookup table method will not be affected by noise, since the shape of $r_{12}(\tau)$ does not change as a result of noise (see Fig. 9 in Wang *et al.* (1981)).

The spectral techniques given by van Dinther *et al.* (2013) use the power spectrum of the scintillometer signal, which is affected by noise. Lowering of the measured intensity signal (e.g., due to fog) to a level lower than $\frac{2}{3}$ of the undisturbed signal will cause an incorrect $U_\perp$ to be obtained by the spectral techniques. Therefore, for the spectral techniques, van Dinther *et al.* (2013) had to apply a filter on signal intensity, causing a data loss of 17%. The $U_\perp$ retrieval methods that rely on $r_{12}(\tau)$ should not be affected by a lowering of the signals, as long as this effect is the same for both signals. Fog (as occurred on some of the mornings during the experiment) should affect both signals in the same way; therefore, for this study no additional filter on signal intensity was necessary. We only filtered out data when the signal intensity was zero, which occurred when the data were transferred from the DLAS to the computer (which took 1 s every minute).

4.5 Results and discussion

In this section the results of the crosswind ($U_\perp$) of the dual large-aperture scintillometer ($U_{\perp\mathrm{DLAS}}$) are validated with $U_\perp$ calculated from the sonic anemometer measurements ($U_{\perp\mathrm{Sonic}}$). We will first discuss the results of $U_{\perp\mathrm{DLAS}}$ obtained from $r_{12}(\tau)$ using the methods discussed in Section 4.3. For every 10-s time window $U_{\perp\mathrm{DLAS}}$ is determined (see the appendix). However, $U_{\perp\mathrm{DLAS}}$ cannot be compared for every 10 s to $U_{\perp\mathrm{Sonic}}$ because the measurement locations of the DLAS and sonic anemometer were not the same and their clocks were not synchronized to the second. Assuming a homogeneous wind field across the flat grass site, the 10-min averaged $U_\perp$ values are used to validate the DLAS measurements with the sonic anemometer measurements.

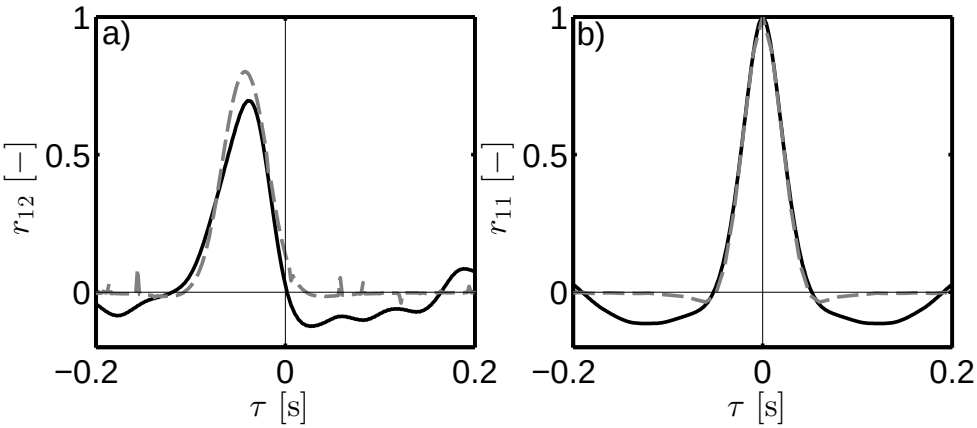

Figure 4.8: Measured (black solid line) and theoretical (gray dashed line) (a) time-lagged correlation function and (b) time-lagged autocorrelation function for $U_\perp = -2.0$ m s^{-1} on DOY 136 at 0:05 UTC.

We will also discuss the results of $U_{\perp\mathrm{DLAS}}$ when using the Briggs method as a quality check. In addition we also compared the 10-min standard deviation of $U_\perp$ ($\mathrm{STD}_{U\perp}$) of the DLAS with that of the sonic anemometer, in order to validate the fluctuations of $U_{\perp\mathrm{DLAS}}$ given by the four methods.

The software of the DLAS used in this study (SRun, Scintec) also uses an algorithm based on $r_{12}(\tau)$ to calculate $U_\perp$. van Dinther *et al.* (2013) reported that SRun version 1.07 overestimates $U_\perp$ with 20%. In this study we will shortly discuss the results of the latest software version of SRun (version 1.14).

4.5.1 Mean crosswind

In Fig. 4.8 the modeled and the measured time-lagged correlation function ($r_{12}(\tau)$) and the time-lagged autocorrelation function ($r_{11}(\tau)$) are plotted for $U_\perp$ = -2.0 m s^{-1}. The modeled and measured functions are similar in shape. The model of Equation 4.1 can, therefore, be used to obtain the constants c_B and c_S, and the lookup table, as was suggested in Section 4.3.

The results of $U_{\perp\mathrm{DLAS}}$ of the four methods are shown in Fig. 4.9. The results are color coded with the longitudinal wind ($U_\parallel$). Note that all the methods obtain a similar $U_\perp$ as the sonic anemometer, but they all tend to overestimate $U_\perp$ when $U_\parallel$ is high ($>$ 2.5 m s^{-1}, orange and red colors in Fig. 4.9) and $U_\perp$ is low ($<$ 2 m s^{-1}). The model of Equation 4.1 assumes that there is no influence of $U_\parallel$ on $r_{12}(\tau)$. However, in

reality $U_{\parallel}$ influences the DLAS signal by advecting eddies into the scintillometer path. The influence of $U_{\parallel}$ is, however, much smaller than that of $U_{\perp}$, since the scintillometer path ($\sim 10^2$ m) is several orders of magnitude higher than the spacing between the DLAS beams ($\sim 10^{-1}$ m). Eddies that are advected into the scintillometer path by $U_{\parallel}$ are uncorrelated for the two signals. Potvin *et al.* (2005) found that $r_{11}(\tau)$ decorrelates faster in time as a result of $U_{\parallel}$. Therefore, $r_{12}(\tau)$ also decorrelates faster in time, leading to an overestimation of $U_{\perp\mathrm{DLAS}}$. However, if $U_{\perp}$ is high (> 2 m s^{-1}), then there is no clear overestimation of $U_{\perp\mathrm{DLAS}}$ for the four methods also not when $U_{\parallel}$ is high (> 2.5 m s^{-1}), which indicates that $U_{\perp}$ indeed has a bigger influence on $r_{12}(\tau)$ than $U_{\parallel}$ for this dataset. The DLAS data used in this study are obtained over a relatively short scintillometer path of only 426 m. For a longer scintillometer path (e.g., microwave scintillometer), the influence of $U_{\parallel}$ should be even lower. For a shorter scintillometer path (e.g., laser scintillometer), the influence of $U_{\parallel}$ should be higher.

The corresponding regression statistics of Fig. 4.9 are given in Table 4.1, where the RMSE is defined by the error of DLAS compared to the sonic anemometer. This table also shows the regression statistics for when we use a Briggs quality check (QC), which will be discussed later. For now we focus on the results without the Briggs-quality check (i.e., Briggs quality check is "none"). The peak method has the hgihest scatter, with an R^2 of 0.80 leading to a high RMSE of 0.82 m s^{-1}. The peak method uses only one point, the time lag of the peak (τ_{P}), in the measured $r_{12}(\tau)$. As our measurement frequency was 500 Hz, τ_{P} is determinable with a resolution of 0.002 s, which means that $U_{\perp}$ can only be solved for specific values. For higher $U_{\perp}$ values (> 4 m s^{-1}) corresponding to a low τ_{P} (< 0.022 s), these specific $U_{\perp}$ values have a limited resolution (see Fig. 4.10). For example $\tau_{\mathrm{P}} = 0.014$ s corresponds to $U_{\perp} = 7.2$ m s^{-1}, while $\tau_{\mathrm{P}} = 0.012$ s corresponds to $U_{\perp} = 6.1$ m s^{-1}; thus, for one 0.002-s step, the difference in $U_{\perp}$ is 1.1 m s^{-1}. The limited resolution for high $U_{\perp}$ makes the peak method less practical than the other methods. The solution is to increase the measurement frequency. To resolve $U_{\perp}$ values up to 15 m s^{-1} with a resolution of 0.2 m s^{-1} a measurement frequency of 1.3 kHz is necessary for the scintillometer setup of this study ($\overline{s(x)} = 0.085$ m).

The zero-slope method and the lookup table method show similar results, with a low amount of scatter ($R^2 = 0.86$ for both) and both with a low RMSE (of 0.59 m s^{-1} and 0.61 m s^{-1}). The fit of $U_{\perp\mathrm{DLAS}}$ and $U_{\perp\mathrm{Sonic}}$ is better for the lookup table method than for the zero-slope method (regression slope of 0.88 compared to 0.76); this is especially the case for higher $U_{\perp}$ values (> 3 m s^{-1}, see Fig. 4.9c and Fig. 4.9d).

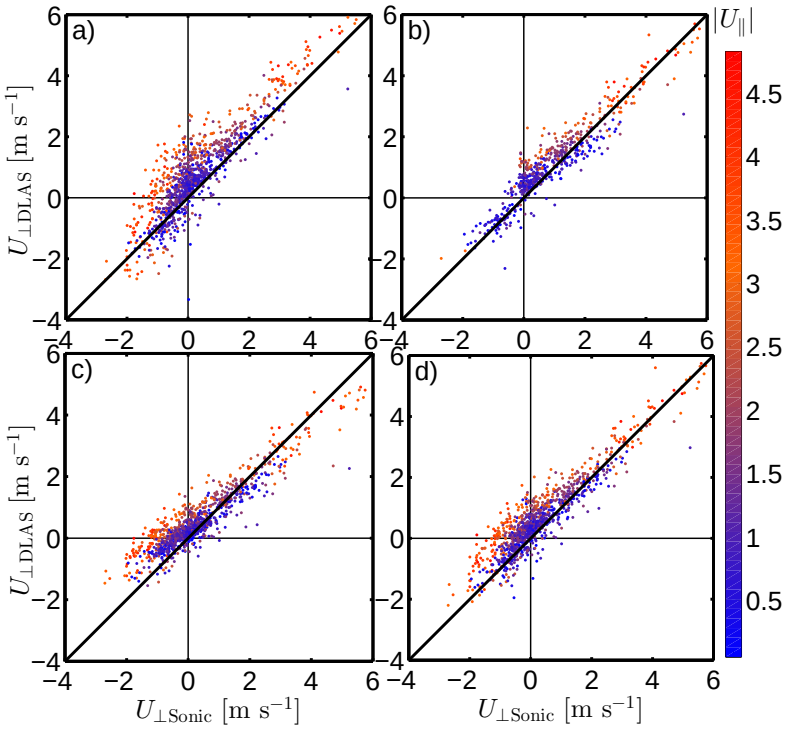

Figure 4.9: Results showing $U_{\perp\mathrm{DLAS}}$ for (a) the peak method, (b) the Briggs method, (c) the zero-slope method, and (d) the lookup table method plotted against $U_{\perp\mathrm{Sonic}}$ over 10 minutes, colored with $U_{\parallel}$.

The Briggs method implicitly uses a quality check. In the next section we will discuss this quality check in more detail. For now we focus on the results of the Briggs method with the strict quality check as is (see Fig. 4.9b and Table 4.1). The results of the Briggs method compare best with those of the sonic anemometer, with a regression slope of 0.89 and an RMSE of only 0.52 m s^{-1}. However, the Briggs method is also the method with the lowest data availability of only 56%. From Fig. 4.9 it is apparent that most data where the Briggs method is not able to find a solution occur when $U_{\parallel}$ is high ($>$ 2.5 m s^{-1}, orange colors in Fig. 4.9). These are also the data points where the other three methods show the most scatter with $U_{\perp\mathrm{Sonic}}$. In the next section, we will discuss in more detail when the Briggs method does not find a solution. Further, we will investigate the usability of the Briggs method as a quality check for the other methods.

van Dinther *et al.* (2013) used the same dataset as the one used in this study.

Table 4.1: Regression equations, R^2, RMSE, and data availability (N) validating $U_{\perp\mathrm{DLAS}}$ with $U_{\perp\mathrm{Sonic}}$ with or without applying the QC.

Method	QC	Regression equation	R^2	RMSE (m s^{-1})	N (%)
Peak	None	$y = 1.01x + 0.48$	0.80	0.82	100
Peak	Loose	$y = 1.07x + 0.34$	0.88	0.67	67
Peak	Strict	$y = 1.06x + 0.37$	0.88	0.70	56
Briggs	Loose	$y = 0.89x + 0.28$	0.88	0.51	67
Briggs	Strict	$y = 0.89x + 0.31$	0.88	0.52	56
Zero slope	None	$y = 0.73x + 0.35$	0.86	0.59	100
Zero slope	Loose	$y = 0.81x + 0.25$	0.89	0.47	67
Zero slope	Strict	$y = 0.80x + 0.27$	0.89	0.48	56
Lookup table	None	$y = 0.86x + 0.40$	0.86	0.61	100
Lookup table	Loose	$y = 0.93x + 0.29$	0.89	0.50	67
Lookup table	Strict	$y = 0.93x + 0.31$	0.91	0.52	56

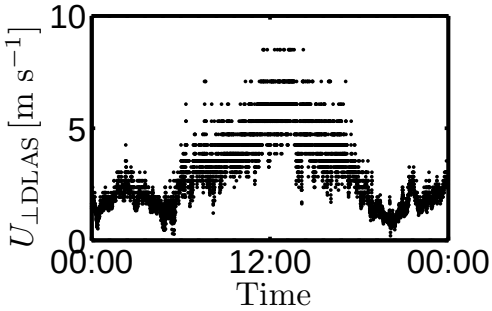

Figure 4.10: Results showing $U_{\perp\mathrm{DLAS}}$ of the peak method for 10 s on DOY 136.

Therefore, the results of the spectral techniques in van Dinther *et al.* (2013) are directly comparable to the results obtained in this study. The results of this study (based on the dual-beam approach; i.e., using $r_{12}(\tau)$) are similar to the results in van Dinther *et al.* (2013) (based on the single-beam approach; i.e., using the scintillation power spectra), with similar scatter (R^2 for both approaches is 0.88 and 0.89) and RMSE (between 0.47 and 0.67 m s^{-1} for the dual-beam approaches and between 0.46 and 0.70 m s^{-1} for the single-beam approaches). An advantage of the dual-beam approaches is that unlike the single-beam approaches, they do not need a filter on the signal intensity, resulting in a data availability of 100% for every dual-beam method except the Briggs method. In summary the dual-beam approaches have the following advantages over the single-beam approaches: $U_\perp$ is determinable over shorter time

intervals ($\sim$ 10 s), the sign of $U_\perp$ is determinable, and the data availability is higher (100% compared to $\leq$ 83%). Therefore, the dual-beam approaches are preferable to the single-beam approaches.

4.5.2 Briggs-quality check

The Briggs method obtains $U_\perp$ from the time lag where $r_{12}(\tau)$,and $r_{11}(\tau)$ intersect (τ_B). The Briggs quality check refers to data where the Briggs method does not find a solution, which occurs if there are no or multiple intersects between $r_{12}(\tau)$ and $r_{11}(\tau)$, indicating that these functions are distorted. We will differentiate between a "loose" and "strict" Briggs-quality check. "Loose" refers to the quality check for data points where there are no intersects between $r_{12}(\tau)$ and $r_{11}(\tau)$ for $0 \leq |\tau_\mathrm{B}| \leq |\tau_\mathrm{P}|$. "Strict" refers to the quality check for data points where there are no or multiple intersects between $r_{12}(\tau)$ and $r_{11}(\tau)$ for $0 \leq |\tau_\mathrm{B}| \leq |\tau_\mathrm{P}|$. With the loose quality check, 67% of the data are left, while with the strict quality check, only 56% of the data are left.

Possible causes for a distorted $r_{12}(\tau)$ and $r_{11}(\tau)$ are variable $U_\perp$ values along the scintillometer path and a strong $U_\parallel$ ($>$ 2.5 m s^{-1}). We cannot investigate the variable $U_\perp$ along the scintillometer path directly, since only one sonic anemometer was measuring the wind field. However, by assuming frozen turbulence, the variability along the scintillometer path is high when the standard deviation over 10 min of $U_{\perp\mathrm{Sonic}}$ ($\mathrm{STD}_{U\perp\mathrm{Sonic}}$) is high. The data filtered out with the strict quality check often coincides with $\mathrm{STD}_{U\perp\mathrm{Sonic}} > 0.5$ m s^{-1} (57% of the filtered data) and $U_\parallel > 2.5$ m s^{-1} (58% of the filtered data). Therefore, we can conclude that a high $\mathrm{STD}_{U\perp}$ and/or high $U_\parallel$ indeed causes a distorted $r_{12}(\tau)$ and $r_{11}(\tau)$.

We tested which intersect (the first or the last) is best to use with the Briggs method in case of multiple intersects between $r_{12}(\tau)$ and $r_{11}(\tau)$ for $0 \leq |\tau_\mathrm{B}| \leq |\tau_\mathrm{P}|$. Using the last intersect as τ_B showed better results than using the first intersect as τ_B: less scatter (R^2 of 0.89 vs 0.59) and a lower RMSE (0.51 m s^{-1} vs 1. m s^{-1}). Therefore, the regression statistics shown in Table 4.1 for the Briggs method with the loose quality check is obtained by using the last intersect (i.e., the intersect closest to τ_P) as τ_B in the case of multiple intersects. Although the results of $U_{\perp\mathrm{DLAS}}$ by using the last intersect are similar to $U_{\perp\mathrm{Sonic}}$, still only 67% of $U_{\perp\mathrm{DLAS}}$ are resolved by the Briggs method.

Results of the four methods filtered with the Briggs quality control are also shown in Table 4.1, and those filtered with the loose quality check are plotted in Fig. 4.11. Comparing the results of the data with and without the Briggs quality check, it is clear that this quality check is valuable. We first compare the results of $U_\perp$ with and without the loose Briggs quality check. For the peak method, the zero-slope method,

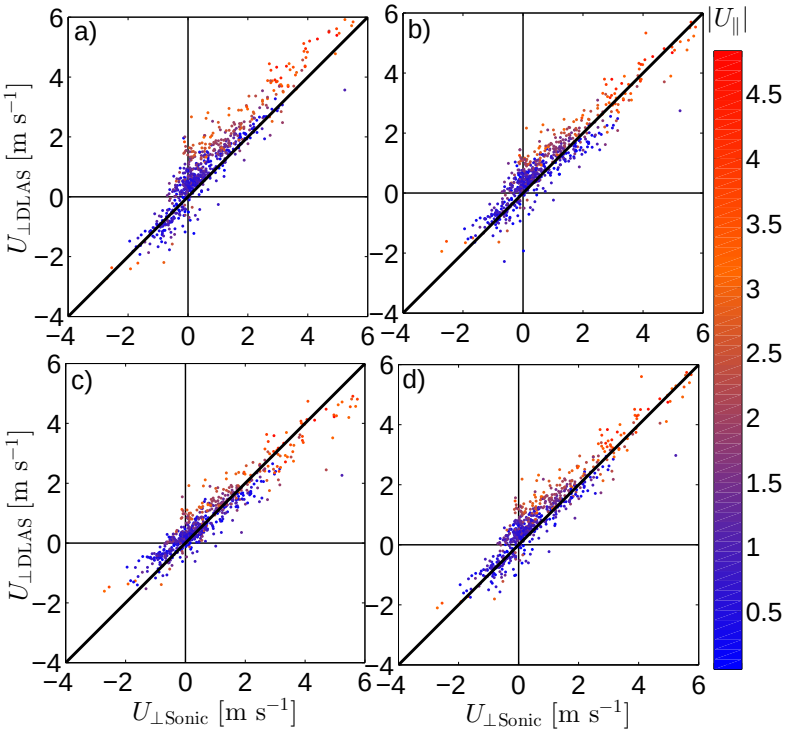

Figure 4.11: Plots of $U_{\perp\mathrm{DLAS}}$ for (a) the peak method, (b) the Briggs method, (c) the zero-slope method, and (d) the lookup table method plotted against $U_{\perp\mathrm{Sonic}}$ over 10 min using the loose quality check, colored with $U_{\parallel}$.

and the lookup table method, all parameters of the linear regression improve when applying the loose Briggs quality check. The RMSE decreases, ranging from 0.59 to 0.82 m s^{-1} without the Briggs quality check to 0.47 to 0.67 m s^{-1} with the loose Briggs quality check. The fit of $U_{\perp\mathrm{DLAS}}$ with $U_{\perp\mathrm{Sonic}}$ improves, with regression slopes closer to one when the loose Briggs quality check is used. Only for the peak method is this not the case, as the regression slope for this method increases from 1.01 to 1.07, but the offset does decrease from 0.48 to 0.34. The R^2 increases by using the loose Briggs quality check: for the peak method it rises from 0.80 to 0.88, and for the zero-slope and lookup table method it rises from 0.86 to 0.89.

Applying the strict Briggs quality check instead of the loose Briggs quality check does not improve the results; the regression statistics stay similar. The RMSE even increases slightly for the four methods (by 0.01 - 0.03 m s^{-1}). However, the strict Briggs quality check does decrease the data availability to 56%.

Table 4.2: Regression equations, R^2, RMSE, and N validating $\mathrm{STD}_{U\perp\mathrm{DLAS}}$ with $\mathrm{STD}_{U\perp\mathrm{Sonic}}$ with or without applying the QC and filtering on $\mathrm{STD}_{U\perp\mathrm{DLAS}} > 2$ m s^{-1}.

Method	QC	Regression equation	R^2	RMSE (m s^{-1})	N (%)
Peak	None	$y = 1.07x + 0.16$	0.38	0.43	84
Peak	Loose	$y = 0.90x + 0.14$	0.32	0.37	62
Peak	Strict	$y = 0.87x + 0.078$	0.46	0.26	54
Briggs	Loose	$y = 0.69x + 0.046$	0.41	0.26	64
Briggs	Strict	$y = 0.70x + 0.030$	0.43	0.25	55
Zero slope	None	$y = 0.76x + 0.097$	0.63	0.19	100
Zero slope	Loose	$y = 0.64x + 0.13$	0.60	0.18	64
Zero slope	Strict	$y = 0.63x + 0.14$	0.59	0.18	55
Lookup table	None	$y = 1.05x + 0.094$	0.44	0.36	97
Lookup table	Loose	$y = 0.81x + 0.072$	0.44	0.26	64
Lookup table	Strict	$y = 0.81x + 0.053$	0.48	0.24	55

Besides the Briggs quality check, two other quality checks were also investigated: the value of the maximum $r_{12}(\tau)$ and the correlation between the measured and modeled $r_{12}(\tau)$. To improve the results of $U_{\perp\mathrm{DLAS}}$, strict thresholds had to be chosen for these quality checks. The maximum in $r_{12}(\tau)$ had to be at least 0.3. The correlation between the measured and modeled $r_{12}(\tau)$ had to be at least 0.9. The results of these quality checks did not improve $U_{\perp\mathrm{DLAS}}$ as much as with the Briggs quality check. Moreover, the data availability after using the maximum $r_{12}(\tau)$ or the correlation between the measured and modeled $r_{12}(\tau)$ as a quality check was lower ($\leq 65\%$), than that after using the loose Briggs quality check. Therefore, we advise to use the loose Briggs quality check.

4.5.3 Standard deviation of the crosswind

The standard deviation of $U_\perp$ ($\mathrm{STD}_{U\perp}$) gives an indication of how well the methods are performing over 10 s. There are some clear outliers in $\mathrm{STD}_{U\perp\mathrm{DLAS}}$ ($\mathrm{STD}_{U\perp\mathrm{DLAS}} > 2$ m s^{-1}) for the peak method (16% of the data up to 7.6 m s^{-1}), the Briggs method (3% of the data up to 7.2 m s^{-1}), and the lookup table method (3% of the data up to 4.5 m s^{-1}) when the Briggs quality check is not used (Fig. 4.12). These outliers mainly occur on 2 days of the experiment (day of the year (DOY) 138 and 139). The cause of these outliers remains unclear. We investigated rain, wind direction, scintillometer signal level, and sign changes in $U_\perp$, but we could not find an explanation for the outliers. The zero-slope method does not have outliers and compares well with $\mathrm{STD}_{U\perp\mathrm{Sonic}}$ for all days of the experiment.

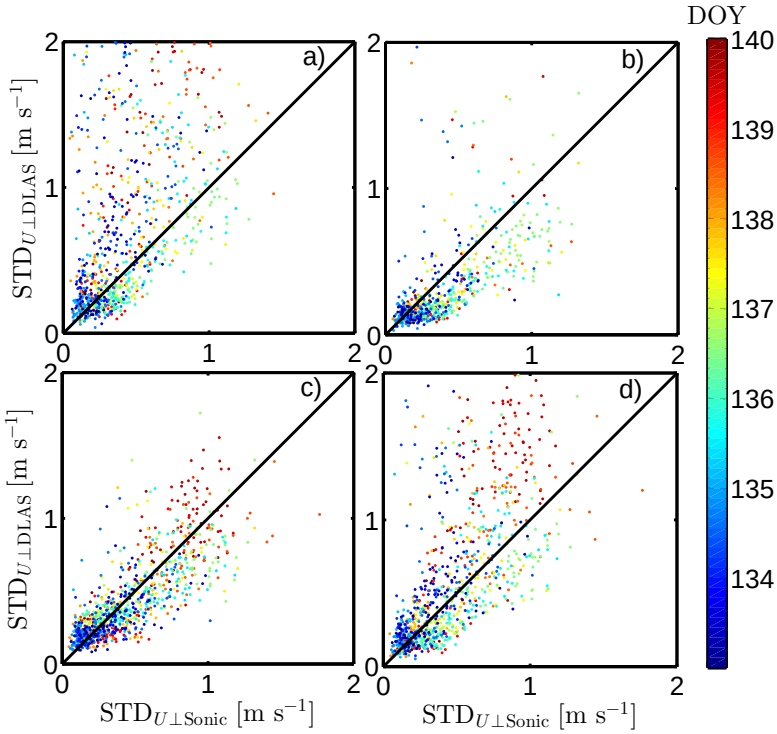

Figure 4.12: Results of $\mathrm{STD_{U\perp DLAS}}$ for (a) the peak method, (b) the Briggs method, (c) the zero-slope method, and (d) the lookup table method against $\mathrm{STD_{U\perp Sonic}}$ over 10 min color coded with DOY (DOY indicated by color scale at right).

The outliers ($\mathrm{STD}_{U\perp\mathrm{DLAS}} > 2$ m s^{-1}) were filtered out to be able to compare $\mathrm{STD}_{U\perp\mathrm{DLAS}}$ with $\mathrm{STD}_{U\perp\mathrm{Sonic}}$; for the results, see Fig. 4.12 and Table 4.2. Another approach to remove outliers is by applying an outlier filter model- for example, the one given by Thompson (1985).

The $\mathrm{STD}_{U\perp\mathrm{DLAS}}$ of the peak method, despite filtering on $\mathrm{STD}_{U\perp\mathrm{DLAS}} > 2$ m s^{-1} and thereby excluding 16% of the data, still showed a poor fit with $\mathrm{STD}_{U\perp\mathrm{Sonic}}$: low R^2 (0.38) and high RMSE (0.43 m s^{-1}). The fit of the Briggs method and the lookup table method with the sonic anemometer measurements was also poor, although better than that of the peak method ($R^2 \leq 0.44$ and RMSE ≥ 0.26 m s^{-1}). The best results for $\mathrm{STD}_{U\perp\mathrm{DLAS}}$ were obtained by the zero-slope method, with the highest R^2 (0.63), lowest RMSE (0.19 m s^{-1}), and highest data availability (100%).

Applying the Briggs quality check improved the results of all the methods (higher R^2 and lower RMSE), except for the zero-slope method. Although applying the

Briggs quality check did result in a lower regression slope for the peak method, the zero-slope method, and the lookup table method. However, for the peak method and lookup table method, this is compensated by the offset of the regression equation, which decreases (from 0.16 to 0.078 m s^{-1} for the peak method and from 0.094 to 0.053 m s^{-1} for the lookup table method). After taking into account the results after applying the Briggs quality check, the best results were still obtained by the zero-slope method without the Briggs quality check. This indicates that the zero-slope method is able to obtain the fluctuations in $U_{\perp\mathrm{DLAS}}$ over 10 min correctly.

4.5.4 SRun version 1.14

The manufacturer of the BLS900 (Scintec) has a software package SRun that uses an algorithm based on $r_{12}(\tau)$ to calculate $U_\perp$. Until now, the algorithm used by SRun was undocumented both in scientific literature and the SRun manual. van Dinther *et al.* (2013) reported that SRun, version 1.07, overestimated $U_\perp$ by almost 20%, resulting in an RMSE of 0.62 m s^{-1}. This prompted Scintec to revise its $U_\perp$ retrieval algorithm in SRun, version 1.14. The results of this new version will be presented here, together with a global outline of the algorithm used by SRun to obtain $U_\perp$ provided by Scintec (A.C. van den Kroonenberg, Scintec AG, 2013, personal communication).

The algorithm is similar to the lookup table method described in Section 4.3.4, where a measured $r_{12}(\tau)$ is compared to the theoretical $r_{12}(\tau)$. The measured $r_{12}(\tau)$ is calculated for -6 s $\leq \tau \leq$ 6 s with 109 steps on a logarithmic scale to decrease computation time. The theoretical $r_{12}(\tau)$ are determined by Gaussian functions ($F(\tau)$) using several combinations of $U_\perp$ (varying between 0.05 and 30 m s^{-1}) and standard deviations of $U_\perp$ (varying between 0.15 and 3.0 m s^{-1}). The measured $r_{12}(\tau)$ is broader than the theoretical $F(\tau)$, due to the spatial expansion of the turbulence elements. Therefore, $F(\tau)$ has to be convolved with a second Gaussian function ($G(\tau)$). This $G(\tau)$ describes the distribution of the eddy sizes and depends on the wavelength that contributes most to the scintillometer signal. The Gaussian fit function is calculated as the discrete convolution of $F(\tau)$ and $G(\tau)$. This fit function is scaled with a factor to obtain the same amplitude as the measured correlation. The fit function that matches the measured $r_{12}(\tau)$ closest (which is determined by a chi-squared test) provides $U_\perp$ and the standard deviation of $U_\perp$. In SRun, version 1.07, the functions describing the turbulence expansion in space (i.e., $G(\tau)$) were too broad, resulting in overestimations of the standard deviation of $U_\perp$ and overestimation of the higher $U_\perp$ values. In SRun, version 1.14, the function $G(\tau)$ was improved (A.C.van den Kroonenberg, Scintec AG, 2013, personal communication).

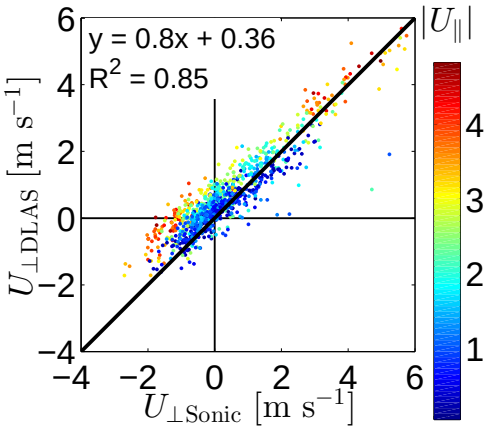

Figure 4.13: Plot of $U_{\perp\mathrm{DLAS}}$ of SRun, version 1.14, against $U_{\perp\mathrm{Sonic}}$ over 10 min, colored with $U_{\parallel}$.

Results of SRun, version 1.14, are shown in Fig. 4.13, including a data filtering used by SRun leading to a data availability of 99%. The same dataset is used in this study as in van Dinther *et al.* (2013); therefore, the results of SRun, version 1.14, are directly comparable to that of SRun, version 1.07 (see Fig. 3.14). The results of $U_{\perp\mathrm{DLAS}}$ improved, especially for the high $U_{\perp}$ values ($>$ 2 m s^{-1}), where the fit of $U_{\perp\mathrm{DLAS}}$ with $U_{\perp\mathrm{Sonic}}$ is better than before. However, there are also some outliers that underestimate $U_{\perp}$, leading to a regression slope of only 0.80. These outliers cause an RMSE of 0.60 m s^{-1}, which is only a bit lower than that of software version 1.07, where it was 0.62 m s^{-1}. Although the error in software version 1.14 seems comparable to software version 1.07, given the better fit for higher $U_{\perp}$ values ($>$ 2 m s^{-1}) we would recommend using version 1.14 over version 1.07 to obtain $U_{\perp}$, especially for the application at airports, where the higher $U_{\perp}$ values are more important.

4.6 Conclusions

In this study the crosswind ($U_{\perp}$) is determined from dual large-aperture scintillometer (DLAS) measurements. The $U_{\perp\mathrm{DLAS}}$ is obtained from the time lagged correlation function ($r_{12}(\tau)$) and the time lagged autocorrelation function ($r_{11}(\tau)$), which are determined over a 10 − s time window. We used four methods to obtain $U_{\perp}$: the peak method, the Briggs method, the zero-slope method, and the lookup table method.

This last method is a new method introduced in this paper. The $U_\perp$ obtained from the DLAS measurements is validated against sonic anemometer measurements. The sonic was not located in the center of the DLAS path. Therefore, for the validation $U_\perp$ is averaged to 10 min.

The 10-min averages of $U_{\perp\mathrm{DLAS}}$ for all the four methods compare reasonably well to $U_{\perp\mathrm{Sonic}}$, with root mean square errors (RMSE) varying from 0.52 to 0.82 m s^{-1}. However, all methods showed an overestimation of $U_{\perp\mathrm{DLAS}}$ when $U_\perp$ is low ($<$ 2 m s^{-1}). Lawrence *et al.* (1972) attributed this overestimation of low $U_\perp$ values to eddy decay, which causes the assumption of frozen turbulence to be violated. Our results, however, show that the overestimation of $U_{\perp\mathrm{DLAS}}$ compared to $U_{\perp\mathrm{Sonic}}$ occurs when the longitudinal wind ($U_\parallel$) is high ($>$ 2.5 m s^{-1}). Potvin *et al.* (2005) showed that $r_{11}(\tau)$ decorrelates faster when $U_\parallel$ is high, which is caused by the fact that $U_\parallel$ also brings in and blows out eddies in the scintillometer path. A faster decorrelation in time of $r_{12}(\tau)$ will be misinterpreted as a higher $U_\perp$ value. Thereby, a high $U_\parallel$ will result in an overestimation of $U_{\perp\mathrm{DLAS}}$. The fact that the overestimation of $U_{\perp\mathrm{DLAS}}$ only occurs for low values of $U_\perp$ ($<$ 2 m s^{-1}) indicates that for higher $U_\perp$ values, the influence of $U_\perp$ is dominant over $U_\parallel$. We expect the influence of $U_\parallel$ to be less for a longer scintillometer path.

The term $U_{\perp\mathrm{DLAS}}$ of the peak method has the worst fit with $U_{\perp\mathrm{Sonic}}$, which is caused by the low resolvable resolution of $U_\perp$ for high values ($>$ 4 m s^{-1}). This low resolution is caused by the fact that the measurement frequency of the DLAS determines the accuracy with which the time lag of the peak in $r_{12}(\tau)$ can be found (e.g., if the measurement frequency is 500 Hz, then accuracy of the peak is determinable to 0.002 s).

The Briggs method seems to obtain the best result for $U_{\perp\mathrm{DLAS}}$. However, this method has an implicit internal filter, which is caused by the fact that the Briggs method does not find a solution when there are no or multiple intersects between $r_{12}(\tau)$ and $r_{11}(\tau)$. We showed that there is a relation between data points when the Briggs method does not find a solution and when $U_\parallel$ is high ($>$ 2.5 m s^{-1}) or $\mathrm{STD}_{U\perp}$ is high ($>$ 0.5 m s^{-1}). The loss of data due to this internal filter can be used as a quality check for the other data. We defined a loose quality check where only the data when there was no intersect between $r_{12}(\tau)$ and $r_{11}(\tau)$ were removed, leading to a data availability of 67%. We defined a strict quality check where data when there was no intersect or multiple intersects between $r_{12}(\tau)$ and $r_{11}(\tau)$ were removed, leading to a data availability of 56%. Besides the loss of data, another problem of the Briggs method is that the constant used by this method (c_B) is, in fact, not constant: c_B decreases with high $U_\perp$ values ($>$ 5 m s^{-1}). The error made by assuming that c_B is constant amounts to -1.3 m s^{-1} for $U_\perp = 10$ m s^{-1}.

The term $U_{\perp\mathrm{DLAS}}$ of both the zero-slope method and the lookup table method compared well to $U_{\perp\mathrm{Sonic}}$, with low RMSE (≤ 0.61 m s^{-1}) and high R^2 values (≥ 0.86). However, for high $U_\perp$ values (> 2 m s^{-1}) the lookup table method gave better results, since the zero-slope method showed a small underestimation of $U_{\perp\mathrm{DLAS}}$ for these values. When applying the loose quality check, the results improved for the zero-slope method and the lookup table method. Therefore, one can choose to optimize the results for data availability (by not applying the Briggs quality check) or to optimize the results for accuracy (by applying the Briggs quality check).

The software (SRun) of the manufacturer of the DLAS used in this study (BLS900, Scintec, Rottenburg, Germany) also obtains $U_\perp$ from $r_{12}(\tau)$. The results of $U_\perp$ of SRun, version 1.14, are better than that of version 1.07 (given by van Dinther *et al.* (2013)), mainly because there is no longer an underestimation of $U_{\perp\mathrm{DLAS}}$ for high values (> 2 m s^{-1}). The results for $U_{\perp\mathrm{DLAS}}$ of SRun, version 1.14, are similar to that of the zero-slope method and the lookup table method in this study.

The 10-min standard deviation (STD) of $U_\perp$ gives an indication of how well the 10-s fluctuations in $U_{\perp\mathrm{DLAS}}$ are resolved. $\mathrm{STD}_{U\perp\mathrm{DLAS}}$ of both the peak method and the Briggs method was not similar to $\mathrm{STD}_{U\perp\mathrm{Sonic}}$, even after filtering on $\mathrm{STD}_{U\perp\mathrm{DLAS}} < 2$ m s^{-1}, mainly due to some outliers. The lookup table method was able to obtain $\mathrm{STD}_{U\perp\mathrm{DLAS}}$; however, the strict Briggs quality check had to be applied. The zero-slope method clearly showed the best results for $\mathrm{STD}_{U\perp\mathrm{DLAS}}$; even without one of the Briggs quality checks, the correspondence with the sonic anemometer was good. The fact that the zero-slope method is also able to obtain the correct $\mathrm{STD}_{U\perp\mathrm{DLAS}}$ enhances our trust in this method.

To conclude, the zero-slope method and the look-up table method showed the best results; $U_{\perp\mathrm{DLAS}}$ and $\mathrm{STD}_{U\perp\mathrm{DLAS}}$ were both similar to that of the sonic anemometer. The zero-slope method obtained better results for low $U_\perp$ values (< 2 m s^{-1}), while the lookup table method obtained better results for high $U_\perp$ values (> 2 m s^{-1}). The peak method and the Briggs method had some issues concerning resolution, data availability, or obtaining the correct $\mathrm{STD}_{U\perp\mathrm{DLAS}}$. The Briggs method did prove to be valuable as a quality check for the other methods.

Acknowledgment

The authors thank Frits Antonysen and Willy Hillen for their assistance with the BLS900 installation. We also thank Aline van den Kroonenberg (Scintec AG, Germany) for giving us more insight into the algorithm used by SRun. This study was funded by the Knowledge for Climate as project “WindVisions” (HSMS01).

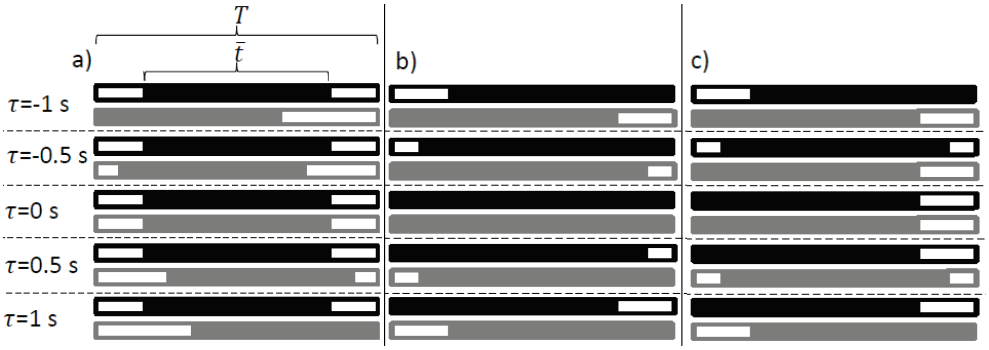

Figure 4A.1: Approaches (a) 1, (b) 2, and (c) 3 of shifting the two signals in time with respect to each other, concerning time period (the total bar, T), time window (the filled bar, $\bar{t}$), and time lag between the two signals (τ). Black blocks represents one signal and gray blocks the other; the time-lagged correlation functions are determined are over the filled color.

4A Appendix: Determination of the Time-Lag Correlation function

When calculating $r_{12}(\tau)$ from DLAS measurements using Equation 4.4, the following time scales are relevant: the time lag (τ), the time period over which r_{12} is determined (T), and the window size ($\bar{t}$). In this appendix we will discuss two issues related to the choice of these time scales and their impact on $r_{12}(\tau)$. First, we will discuss the three approaches by which the two signals (I_1 and I_2) can be shifted with respect to each other. Second, we will discuss which $\bar{t}$ should be chosen to minimize the influence of random errors on $r_{12}(\tau)$.

4A.1 Shifting the two signals with respect to each other to obtain $r_{12}(\tau)$

We investigated three approaches to calculate $r_{12}(\tau)$, which have the following characteristics (see also Fig. 4A.1);

a) $\bar{t}$ is constant, I_1 is fixed while I_2 shifts, and $T = \bar{t} + 2\tau$.

b) $\bar{t}$ is variable, both I_1 and I_2 shift with respect to each other, and $T = \bar{t} + \tau$.

c) $\bar{t}$ is constant, both I_1 and I_2 shift with respect to each other, and $T = \bar{t} + \tau$.

Table 4A.1: Regression equations, R^2, RMSE, and N validating $U_{\perp\text{DLAS}}$ with $U_{\perp\text{Sonic}}$ using approaches 1-3 to shift the signals with respect to each other. Note that N of the Briggs method is not 100% because this method does not yield a solution when there is no intersect between $r_{11}(\tau)$ and $r_{12}(\tau)$

Method	Approach	Regression equation	R^2	RMSE (m s^{-1})	N (%)
Peak	1	$y = 0.95x + 0.44$	0.80	0.75	100
Peak	2	$y = 0.93x + 0.46$	0.80	0.76	100
Peak	3	$y = 1.01x + 0.48$	0.80	0.82	100
Briggs	1	$y = 0.78x + 0.25$	0.86	0.52	67
Briggs	2	$y = 0.77x + 0.26$	0.86	0.53	65
Briggs	3	$y = 0.89x + 0.28$	0.88	0.51	67
Zero slope	2	$y = 0.66x + 0.28$	0.86	0.59	100
Zero slope	2	$y = 0.60x + 0.39$	0.81	0.70	100
Zero slope	3	$y = 0.73x + 0.35$	0.86	0.59	100
Lookup table	1	$y = 0.82x + 0.37$	0.85	0.60	100
Lookup table	2	$y = 0.81x + 0.39$	0.85	0.61	100
Lookup table	3	$y = 0.86x + 0.40$	0.86	0.61	100

These three approaches and the four methods discussed in Section 4.3 were used to obtain the crosswind of the DLAS ($U_{\perp\text{DLAS}}$). $U_{\perp\text{DLAS}}$, which was validated against sonic anemometer measurements ($U_{\perp\text{Sonic}}$).

The results of the three approaches and four methods are shown in Table 4A.1. In general, the results are similar for the three approaches, with comparable regression equations and RMSE. The similarity for the three approaches indicates that the approach by which $r_{12}(\tau)$ is calculated from DLAS measurements does not influence $U_{\perp\text{DLAS}}$ severely. However, there are small differences in $U_{\perp\text{DLAS}}$ for the three approaches: for the Briggs method and the zero-slope method approach 3 gave the best results (lowest RMSE and best fit with $U_{\perp\text{Sonic}}$). Given the fact that approach 3 gave the best results for two of the methods and that this approach has a low T and a constant $\bar{t}$, we decided to use this method to calculate $U_{\perp\text{DLAS}}$.

4A.2 Time window over which $r_{12}(\tau)$ should be determined

The $r_{12}(\tau)$ should be determined over a sufficient T to reduce the influence of random errors and to capture enough statistics to ensure correlation between the two signals. The results of T =3, 10, 30, and 60 s are plotted in Fig 4A.2. The peak associated with $U_\perp$ is located at $\tau = 0.072$ s. However, for $T = 3$ s there are also reasonably high peaks (around 0.3) in $r_{12}(\tau)$ at other τ values that are not associated with $U_\perp$. Fig. 4A.2 indicates that the longer $\bar{t}$, the smaller the peaks not associated with $U_\perp$.

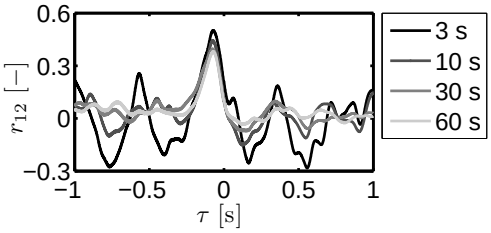

Figure 4A.2: Measured time-lagged correlation function ($r_{12}(\tau)$) for time windows of 3, 10, 30, and 60 s.

In particular, the peaks unassociated with $U_\perp$ decrease when $\bar{t} = 10$ s is used instead of $\bar{t} = 3$ s.

For the application at airports, $U_{\perp\mathrm{DLAS}}$ should be available over the shortest $\bar{t}$ possible. Given Fig. 4A.2, $\bar{t} = 10$ s should be sufficient to obtain reliable $U_{\perp\mathrm{DLAS}}$ values.

5

Observing crosswind over urban terrain using scintillometer and Doppler lidar

In this study, the crosswind (wind component perpendicular to a path, $U_\perp$) has been measured by a scintillometer and Doppler lidar above the urban environment of Helsinki, Finland, for 15 days. The scintillometer allows acquisition of a path-averaged value of $U_\perp$ ($\overline{U_\perp}$), while the Doppler lidar allows acquisition of path-resolved $U_\perp$ ($U_\perp(x)$, where x is the position along the path). The goal of this study is to evaluate the performance of scintillometer $\overline{U_\perp}$-estimates for conditions where $U_\perp(x)$ is variable. Two methods were applied to obtain $\overline{U_\perp}$ from the scintillometer signal; the cumulative spectrum method (relies on scintillation spectra) and the lookup table method (relies on time-lagged correlation functions). The values of $\overline{U_\perp}$ of both methods compared well with the Doppler lidar estimates; with root mean square errors of 0.71 and 0.73 $\mathrm{m\ s^{-1}}$*. This indicates that, given the data treatment applied in this study, both measurement technologies are able to obtain $\overline{U_\perp}$ in the complex urban environment. The detailed investigation of four cases indicate that the cumulative spectrum method is less susceptible to a variable $U_\perp(x)$ than the lookup table method. However, the lookup table method can be adjusted to improve its capabilities to obtain $\overline{U_\perp}$ for conditions where $U_\perp(x)$ is variable.*

This chapter is based on van Dinther *et al.* (2014).

5.1 Introduction

The general application of a scintillometer in micrometeorology is obtaining path-averaged surface fluxes (among others De Bruin *et al.*, 2002; Meijninger *et al.*, 2002a,b). The path can range from a few hundred meters to a few kilometers depending on the type of scintillometer used (De Bruin *et al.*, 2002). In this study the focus is on obtaining the path-averaged crosswind from a scintillometer (among others Briggs *et al.*, 1950; Wang *et al.*, 1981), where the crosswind ($U_\perp$) is defined as the wind-component perpendicular to the scintillometer path. By obtaining a path-averaged value of $U_\perp$ ($\overline{U_\perp}$) instead of a point measurement, a scintillometer is more suitable for validation of winds from model output – given the resolution of numerical weather prediction models (∼10 km) – than point measurements. Furthermore, point measurements can more easily be biased than path-averaged values, especially for urban areas at heights within about 2–3 times the canopy-layer depth (the canopy layer is typically defined as the average building height).

From scintillometer data, one can obtain $\overline{U_\perp}$ from either the scintillation power spectrum ($S_{11}(f)$, where f is the frequency) (van Dinther *et al.*, 2013) or the time-lagged correlation function ($r_{12}(\tau)$, where τ is the time-lag) (among others Briggs *et al.*, 1950; Poggio *et al.*, 2000; van Dinther & Hartogensis, 2014). The validation of $\overline{U_\perp}$ has, so far, mainly taken place on flat grassland sites (Poggio *et al.*, 2000; van Dinther *et al.*, 2013). At such sites $U_\perp$ is assumed to be uniform along the scintillometer path. Despite that, there is also a need for scintillometer $\overline{U_\perp}$ in more complex areas, such as mountain environments (Poggio *et al.*, 2000) and urban environments (above the River Thames in London in Wood *et al.* (2013c)). Ward *et al.* (2011) studied the influence of a variable $U_\perp$-field along the path ($U_\perp(x)$, where x is the location on the scintillometer path) on the scintillometer signal – however, their focus was on scintillation spectra and structure parameter estimates rather than on $\overline{U_\perp}$-estimates. The $U_\perp(x)$-fields used in their study were all synthetic. In the present study, the focus is on the influence of a measured (i.e., non-synthetic) variable $U_\perp(x)$ on the $\overline{U_\perp}$-estimate of a scintillometer.

The measurements investigated in this study are taken in the urban environment. In such an environment the wind speed and direction are spatially variable (Bornstein & Johnson, 1977), making it a suitable environment to study the influence of a variable $U_\perp(x)$ on the scintillometer estimates of $\overline{U_\perp}$. Key to this study are measurements of the variability of $U_\perp(x)$, that are estimated by a scanning Doppler lidar (LIght Detection And Ranging). In this experiment the Doppler lidar was set up in a horizontal scan configuration, in order to estimate the horizontal wind speed and

wind direction along the scintillometer path using a duo-beam method (Wood *et al.*, 2013c).

The measurements were taken in Helsinki, Finland, as part of the Helsinki URban Boundary-Layer Atmosphere Network (Helsinki UrBAN Wood *et al.*, 2013a, http://urban.fmi.fi). The strong spatial and temporal variability of $U_\perp(x)$ induced by buildings poses challenges for both the Doppler lidar and the scintillometer technologies: (i) the Doppler lidar, since one assumes homogeneity of the wind field within each range-gate (sampling bin) for both beams: and (ii) the scintillometer, since both $S_{11}(f)$ and $r_{12}(\tau)$ used in the $\overline{U_\perp}$-retrieval algorithms, are influenced by a variable $U_\perp(x)$ although the algorithms do not take this influence into account (van Dinther *et al.*, 2013; van Dinther & Hartogensis, 2014). We are, therefore, working at the limit of both measurement technologies.

The main goal of this study is to investigate the performance of the scintillometer to measure $\overline{U_\perp}$ in conditions where $U_\perp(x)$ is variable. In order to do so, scintillometer estimates of $\overline{U_\perp}$ are compared to estimates that of the Doppler lidar. However, also for the Doppler lidar the heterogeneous wind conditions are challenging. Therefore, before the scintillometer and Doppler lidar $\overline{U_\perp}$ estimates are compared to each other the applicability of the Doppler lidar to estimate $U_\perp(x)$ is investigated by comparing with sonic anemometer measurements. Lastly, four cases will be selected where $U_\perp(x)$ estimated by the Doppler lidar is used to obtain the theoretical $S_{11}(f)$ and $r_{12}(\tau)$, from the models given by Clifford (1971) and Lawrence *et al.* (1972), respectively. The influence of a variable $U_\perp(x)$ on the theoretical $S_{11}(f)$ and $r_{12}(\tau)$ gives insight into the robustness of the scintillometer methods to obtain $\overline{U_\perp}$.

5.2 Theory and Methods

5.2.1 Scintillometry

A scintillometer consists of a transmitter and a receiver. In this study, a large aperture scintillometer is used of which the transmitter emits near-infrared radiation. This radiation is scattered by eddies in the atmosphere. The atmosphere is turbulent, leading to an eddy field which constantly changes. The intensity measured by the receiver, therefore, fluctuates on short time-scales ($\sim$ 1 s). For these time-scales Taylor's frozen-turbulence assumption is valid, making $U_\perp$ the only driver of changes in the eddy field.

The value of $\overline{U_\perp}$ can be obtained from the intensity fluctuations (also referred to as scintillation signal) by either the scintillation power spectrum or from the time-lagged correlation function. In this study we will use the cumulative spectrum method to

obtain $\overline{U_\perp}$ from $S_{11}(f)$ (van Dinther *et al.*, 2013), and the lookup table method to obtain $\overline{U_\perp}$ from $r_{12}(\tau)$ (van Dinther & Hartogensis, 2014). A detailed description of the methods is given in van Dinther *et al.* (2013) and van Dinther & Hartogensis (2014), a brief outline of the methods are given below.

5.2.1.1 Scintillation spectra

The scintillation spectrum ($S_{11}(f)$) gives insight into which frequencies contribute to the variance of the scintillation signal. Clifford (1971) describes a theoretical model of the scintillation spectrum. Adjusting this model for a large-aperture scintillometer (as used in this study) gives (Nieveen *et al.*, 1998):

$$S_{11}(f) = 16\pi^2 k^2 \int_0^1 \int_{2\pi f/U_\perp(x)}^{\infty} K\phi_n(K) \sin^2\left(\frac{K^2 Lx(1-x)}{2k}\right) \left[(KU_\perp(x))^2 - (2\pi f)^2\right]^{-1/2} \left(\frac{2J_1(0.5KD_\mathrm{R}x)}{0.5KD_\mathrm{R}x}\right)^2 \left(\frac{2J_1(0.5KD_\mathrm{T}(1-x))}{0.5KD_\mathrm{T}(1-x)}\right)^2 dK dx, \quad (5.1)$$

where f is the frequency for which S_{11} is representative, k is the wave number of the emitted radiation, K the turbulent spatial wave number, L is the scintillometer path length, x is the relative location on the path, J_1 is the first-order Bessel function of the first kind, D_R is the aperture diameter of the receiver, D_T is the aperture diameter of the transmitter, and $\phi_n(K)$ is the three-dimensional spectrum of the refractive index in the inertial range given by Kolmogorov (1941). As can be seen in Eq. (5.1), $U_\perp(x)$ influences the scintillation spectrum. In fact, the scintillation spectrum shifts linearly across the frequency axis as a function of $\overline{U_\perp}$. Therefore, by obtaining a characteristic point in the spectrum, $\overline{U_\perp}$ can be obtained, see van Dinther *et al.* (2013).

The cumulative spectrum is obtained by integrating a scintillation spectrum from low to high frequency and normalizing this integration by the variance in the scintillation signal. The cumulative spectrum method takes into account multiple characteristic frequency points (f_CS), which are in this study defined as the frequency points where the cumulative spectrum is 0.5, 0.6, 0.7, 0.8, and 0.9 (as in van Dinther *et al.* (2013)). For each of these five points, a value of $\overline{U_\perp}$ is determined by:

$$\overline{U_\perp} = C_\mathrm{CS} \cdot f_\mathrm{CS}, \quad (5.2)$$

where C_CS is a unique constant, which depends on the experimental setup and scintillometer used, that can be derived from the theoretical $S_{11}(f)$ (Eq. (5.1)), by filling in values of $U_\perp$ and assuming that $U_\perp(x)$ is constant, for the five different frequency points. Subsequently, the five different $\overline{U_\perp}$-values are averaged to obtain one value of $\overline{U_\perp}$ per cumulative spectrum. In this study we will investigate to what extend

the assumption that C_{CS} = constant holds when $U_{\perp}(x)$ varies. This investigation is carried out by means of four cases where the $U_{\perp}(x)$-estimates of the Doppler lidar are used in Eq. (5.1) to obtain the theoretical $S_{11}(f)$. Therefore, Eq. (5.1) is not integrated for x over 0 to 1, but over the 136 range-gates measured by the Doppler lidar (see Section 5.4.3). The cumulative spectra are obtained over 10-min periods in this study.

5.2.1.2 Time-lagged correlation function

The value of $\overline{U_{\perp}}$ can be obtained from a dual-aperture scintillometer (scintillometer with horizontally displaced beams) using $r_{12}(\tau)$. The benefit of the methods relying on $r_{12}(\tau)$ instead of $S_{11}(f)$ is that also the crosswind direction (i.e., the sign of $\overline{U_{\perp}}$) can be obtained from $r_{12}(\tau)$. Another benefit is that $r_{12}(\tau)$ can be determined over a short time-scale ($\sim$ 10 s), while $S_{11}(f)$ needs to be determined over a longer time-scale ($\sim$ 10 min). On the other hand, $r_{12}(\tau)$ needs to be obtained from a dual-aperture scintillometer, while scintillation spectra can in principal be obtained from every type of scintillometer.

The crosswind transports the eddy field through the scintillometer beams. For a dual-aperture scintillometer the two transmitters and receivers are in general setup with only a small separation distance ($\sim$ 10 cm) between the two. Therefore, it takes a short time for the eddy field to travel from the one beam to the other, making that the eddy field barely changes (i.e., frozen turbulence assumption can be assumed). The signals of the two spatially separated scintillometer beams should thus be almost identical except for a time shift. This time shift is related to $\overline{U_{\perp}}$, and can be obtained from $r_{12}(\tau)$. A theoretical model of the time-lagged covariance function ($C_{12}(\tau)$) is given by Lawrence *et al.* (1972), here including the large-aperture averaging terms of Wang *et al.* (1978):

$$C_{12}(\tau) = 16\pi^2 k^2 \int_0^1 \int_0^\infty K\phi_n(K) \sin^2\left[\frac{K^2 Lx(1-x)}{2k}\right] J_0\{K[s(x) - U_{\perp}(x)\tau]\} \left[\frac{2J_1\big(0.5KD_{\mathrm{R}}x\big)}{0.5KD_{\mathrm{R}}x}\right]^2 \left\{\frac{2J_1\big[0.5KD_{\mathrm{T}}(1-x)\big]}{0.5KD_{\mathrm{T}}(1-x)}\right\}^2 dKdx, \quad (5.3)$$

where J_0 is the zero-order Bessel function of the first kind, and $s(x)$ is the separation distance between the two beams at location x. The theoretical $r_{12}(\tau)$ can be obtained by dividing the theoretical $C_{12}(\tau)$ by the theoretical $C_{11}(\tau)$, where $C_{11}(\tau)$ is obtained from Eq. (5.3) by taking $s(x) = 0$ (i.e., variance of the signal).

In this study, we will use the lookup table method to obtain $\overline{U_{\perp}}$ from $r_{12}(\tau)$. A lookup table is created with values of the theoretical $r_{12}(\tau)$ (using Eq. (5.3)) given

a range of $\overline{U_\perp}$ values (resolution of 0.1 m s^{-1}) and time-lag values (resolution of 0.002 s, equal to the measurement frequency of the scintillometer) (van Dinther & Hartogensis, 2014). Note that $U_\perp(x)$ is assumed to be constant when creating the lookup table. The estimate of $\overline{U_\perp}$ is obtained by comparing the measured $r_{12}(\tau)$ values to the theoretical $r_{12}(\tau)$ values of the lookup table. The theoretical $r_{12}(\tau)$ that has the best fit with the measured $r_{12}(\tau)$ thus yields the value of $\overline{U_\perp}$.

The effects of having a variable $U_\perp(x)$ on $r_{12}(\tau)$ and thereby on $\overline{U_\perp}$ will be investigated by means of four cases (see Section 5.4.3). For these four cases Eq. (5.3) is integrated over the 136 range gates given the different values for $U_\perp(x)$ estimated by the Doppler lidar. In this study $r_{12}(\tau)$, and thereby $\overline{U_\perp}$, are determined over 10-s intervals. For the comparison between the scintillometer and Doppler lidar the 10-s $\overline{U_\perp}$-values are arithmetically averaged to 10 min.

5.2.2 Doppler lidar

In this study, a HALO Photonics (Malvern, UK) Streamline scanning Doppler heterodyne lidar is used. Full details of this type of Doppler lidar are described in Hirsikko *et al.* (2014), but briefly summarized here. The Doppler lidar emits pulses of radiation at a wavelength of 1.5 μm; any backscattered radiation from aerosols is used to estimate wind in the atmosphere by assuming that aerosols are perfect tracers of the wind. The pulse repetition rate is 15000 Hz; a 1-s ray is obtained from the accumulation of 15000 pulses. In the returned signal there is a Doppler shift, which enables calculation of the Doppler velocity, i.e., the velocity in the direction in which the Doppler lidar beam is pointing (also referred to as radial or along-beam wind).

In this study, the crosswind component of the wind speed is needed in order to compare with scintillometer estimates. The required wind component can be estimated from the radial Doppler velocities by applying the duo-beam method (Wood *et al.*, 2013c). The method determines the horizontal wind speed and wind direction using trigonometric identities, from which $U_\perp(x)$ can be determined.

The duo-beam method relies, as the name implies, on two sets of measurements from the Doppler lidar: at two different azimuths (i.e., beam-pointing directions in the horizontal plane). A detailed description of this method is given in Wood *et al.* (2013c), a brief outline of the method is given here. The radial velocity (V_b^g) for each range-gate (g), as estimated by the Doppler lidar, and beam number (b) is given by

$$V_b^g = U^g \cos(\phi^g + \pi - \theta_b), \tag{5.4}$$

where U^g is the transect wind speed, ϕ^g is the wind-direction bearing from north, and θ_b is the bearing of the beam angle. When applying Eq. (5.4) for two beams, with

different θ_b, the two unknowns U^g and ϕ^g can be solved, by assuming $V_1^g = V_2^g$. From U^g and ϕ^g, the value of $U_\perp$ can be obtained for each range gate. It is implicit in this method that the wind field is constant between the two lidar beams. Clearly this is not the case in the atmosphere, and one might expect the effects to average out well above buildings (e.g. often assumed so above the roughness sublayer; Roth (2000); Kastner-Klein & Rotach (2004)). But at heights within, say, 2–3 mean building heights, there will inevitably be errors, perhaps including bias, caused by this implicit assumption.

The fixed resolution of the radial wind (of 0.023 m s^{-1}) also limits the duo-beam method; i.e. in general as the beam separation becomes infinitesimally small, so does the need for accuracy to become infinitesimally fine.

5.3 Experimental setup

The measurements in the present study were taken from 1st to 15th of October 2013. The measurement devices used in this study are a scintillometer, a Doppler lidar, and two sonic anemometers. A layout of the measurement devices is given in Fig. 5.1.

The scintillometer used in this study is a BLS900 (Scintec, Rottenburg, Germany) running with SRun software version 1.09. Note that in this study the output of $\overline{U_\perp}$ given in SRun is not used. The BLS900 is a scintillometer with two transmitters and one receiver. Raw signal intensities were measured and stored at a frequency of 500 Hz. The setup of the scintillometer is the same as that of other recent Helsinki scintillometer work (Wood *et al.*, 2013b). The scintillometer measured over a path of 4.2 km. The transmitter unit was placed at a roof section of Hotel Torni a height of 67 m, while the receiver was placed on a roof near the so-called SMEAR-III-Kumpula station at a height of 52.9 m (see Fig. 5.1). The surrounding areas have average building heights of 24 and 20 metres, and zero-plane displacement heights of 15 and 13 metres, at the transmitter and receiver respectively (Nordbo *et al.*, 2013). The orientation of the scintillometer was nearly south-north (17°) – therefore, the wind was nearly-perpendicular to the scintillometer path when it was blowing from the east or west. In this study, $U_\perp$ is defined as positive when the wind is blowing from the west into the path.

The Doppler lidar was placed near the receiver of the scintillometer at a height of 45 m. Each ray lasts for 1 s and is repeated every 4 s. Every 5 min, a set of 10 rays (i.e., taking 40 s) was made comprising different beam angles. From this set, only the 174 and 196°azimuth angles were used in this study, see Fig. 5.1. This pair was wider apart than desired, due to line-of-sight issues. The elevation of the beam was 0.45°. The Doppler lidar data are given in a series of 30-m range-gates centered at distances 105–9585 m from the instrument, but data were only needed until 4155 m

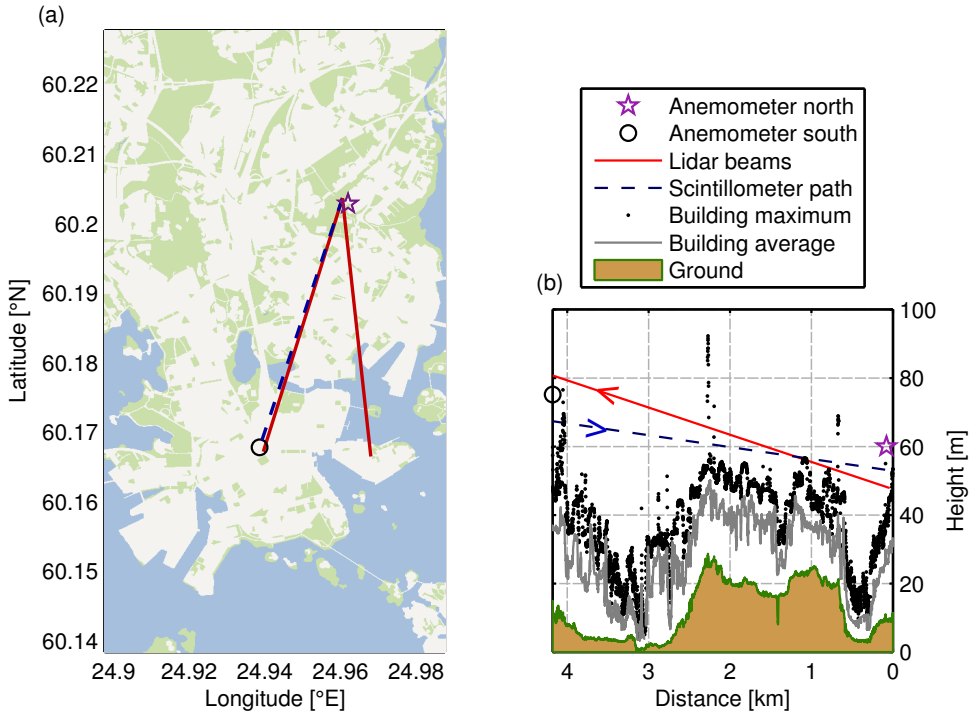

Figure 5.1: (a) Experimental setup with the locations of the instruments in Helsinki indicated, including Doppler lidar-beam azimuths of 174 and 196°; shading is buildings/roads (white), grass/trees (green), and water (blue) (land cover data-source: HSY, 2008); the city-center is roughly the lower half of the map area. (b) A cross-section (height m asl) of the scintillometer beam and Doppler lidar 196°-beam; average building height and maximum building height are with respect to ±250 m laterally of the 196°-beam (building height data source: PaITuli, 2012).

(i.e., 136 range-gates corresponding to the 4.19 km length of the scintillometer path). However – given the atmospheric aerosol loading, sensitivity of the instrument, and integration times – sometimes not enough signal could returned from the farthest gates and therefore results in a limited range of the data. In order to compare the Doppler lidar estimates with $\overline{U_\perp}$ estimates of the scintillometer, two of the Doppler lidar estimates were averaged. Therefore, $\overline{U_\perp}$ estimates of the Doppler lidar were available at 10-minute intervals.

A 3D sonic anemometer was located at 75 m height (near the scintillometer transmitter, denoted here as "Anemometer south") and another at 60 m (near the receiver, denoted here as "Anemometer north"), see Fig. 5.1. Due to the mast mounting,

the wind directions are more uncertain for 0–50°for Anemometer north, and in between 50–185°for Anemometer south. Fortunately, the wind directions during the study were mainly 210–350°. For more details of the anemometer setup see Järvi *et al.* (2009) and Nordbo *et al.* (2013). The value of $U_\perp$ measured by each of the anemometers was added to the beginning and the end of the Doppler lidar-path estimates, giving a fuller path of $U_\perp(x)$. The estimates of $U_\perp(x)$ were path-averaged according to the scintillometer path-weighting function given by Wang *et al.* (1978) for comparison with $\overline{U_\perp}$ estimated by the scintillometer. In case of missing $U_\perp(x)$ data the path-weighting factors were scaled to a total of 100 % in order to calculate the estimate of $\overline{U_\perp}$ of the Doppler lidar. Note that because of the bell-shaped path-weighting function, the anemometer measurements are barely (only for 2.5 %) included in the path-weight averaged $U_\perp$ estimates over the path. For the comparison between Doppler lidar and scintillometer, an arbitrary requirement was that at least 50 % of $U_\perp(x)$ of the Doppler lidar data were available along the scintillometer path.

5.4 Results and discussion

5.4.1 Doppler lidar path-resolved crosswinds

For the Doppler lidar, the urban environment is challenging, since the duo-beam method assumes a homogeneous wind field at each range-gate distance. This assumption will be violated to an unknown degree as the pair of beams diverges. Therefore– before comparing the scintillometer with the Doppler lidar– measurements periods and conditions are identified where the Doppler lidar differs from south anemometer measurements. We evaluate the difference between $U_\perp(x)$ estimated by the Doppler lidar and $U_\perp$ measured by the south anemometer, to see the impact of the wind direction and building height (see Fig. 5.2). Note that a perfect agreement between the Doppler lidar and anemometer estimates is not expected, since the measurement locations are different. The first ten range-gates of $U_\perp$ of the Doppler lidar compared well with that measured by anemometer north for the time-period studied, with root-mean-square deviation (RMSD) values of 0.57 m s^{-1}. Hirsikko *et al.* (2014) showed for the same experimental setup, but a different time-period, a RMSD of 0.53–0.67 m s^{-1} for the Doppler velocity between Doppler lidar and sonic anemometer.

It should be noted that the sign of $U_\perp(x)$ is determined by the wind direction estimated by the Doppler lidar. When the wind is near parallel to the path, a small error in the estimated wind direction can result in an error of the sign of $U_\perp(x)$. The wind directions where the wind is near-parallel to the path (167–227°and 347–47°) are denoted in light-red shading in the lower figure-panel. It can clearly be seen that

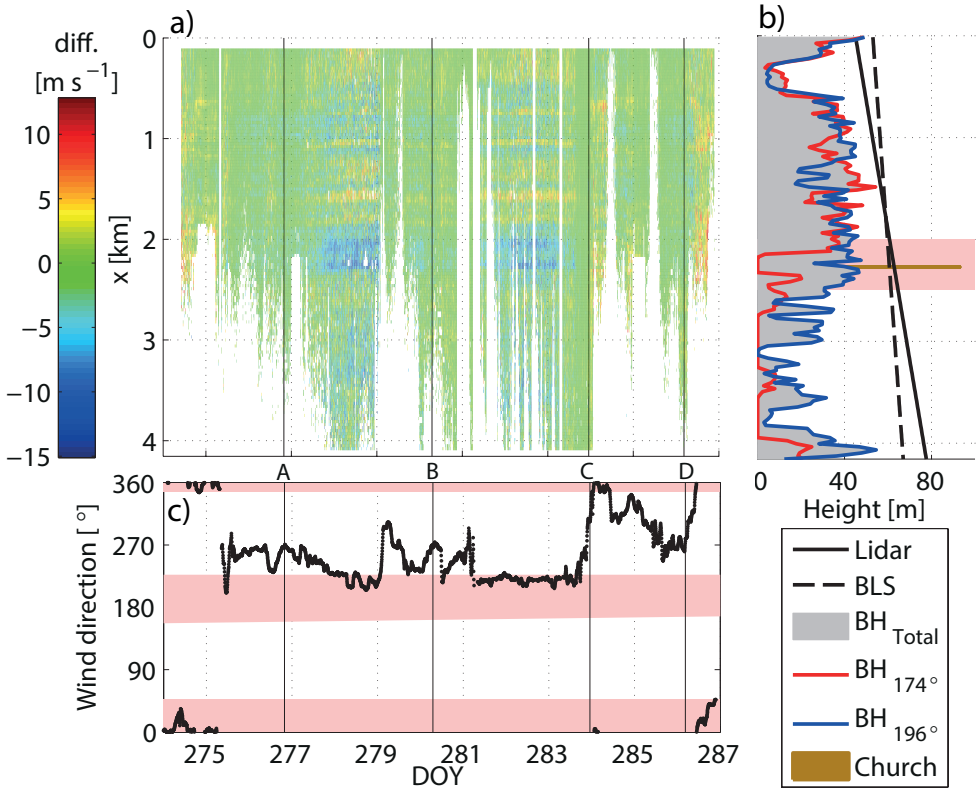

Figure 5.2: (a) The difference in $U_\perp$ estimated by the Doppler lidar duo-beam method compared with the south anemometer (colorbar) as a function of Doppler lidar beam distance (resolution of 30 m) and time (resolution of 10-min, DOY = day of year). (b) The height (asl) of the Doppler lidar beam and building height (BH) ± 25 m laterally underneath the paths (total, and under beam with azimuth 174 and 196°). When there are no buildings below the path, BH indicates the height of highest ground point or zero when it is over sea. (c) The wind direction against DOY from the south anemometer.

there is a substantial difference between Doppler lidar and anemometer for these wind directions, especially when the wind is blowing from 200–227°. Even sign changes of the difference are observed. The winds from the 200–227°directions are also strong (> 5 m s^{-1}). Therefore, the corresponding $U_\perp(x)$-values are still moderate (absolute up to 3 m s^{-1}) for these wind directions. A small error in the wind direction can therefore result in a sign change of a moderate $U_\perp(x)$, which is indeed what we see in Fig. 5.2. Also for the wind direction 347–46°there is a clear difference between $U_\perp(x)$ of the Doppler lidar and $U_\perp$ of the anemometer, with differences up to 10 m s^{-1}. Whilst we might expect differences above the urban canopy layer, to have such large

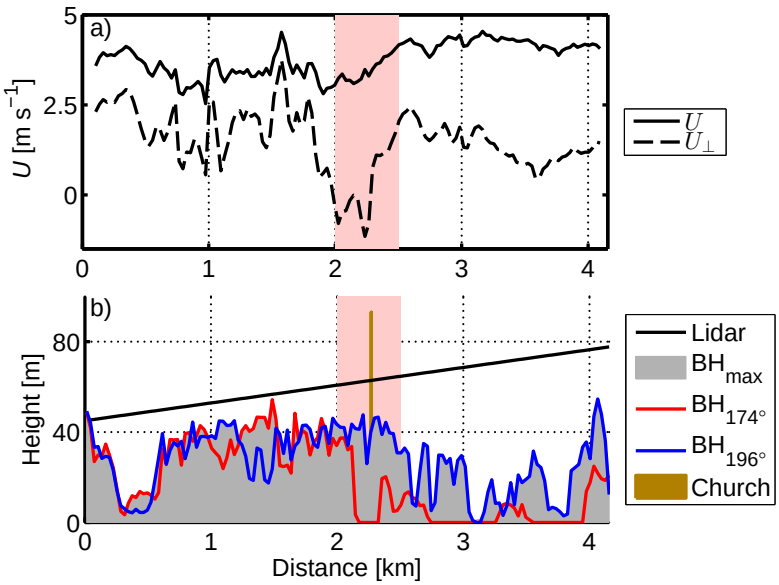

Figure 5.3: (a) Average horizontal wind speed and crosswind speed estimated by the Doppler lidar. (b) The height (asl) of the Doppler lidar beam and building height (BH) ± 25 m laterally underneath the paths (total, and under beam with azimuth 174 and 196°). When there are no buildings below the path, BH indicates the height of highest ground point or zero when it is over sea.

differences for hundreds of meters seems unrealistic. Perhaps this is a breakdown of the homogeneity assumption required for the duo-beam method. Whatever the cause, it is deemed that Doppler lidar values where the wind direction is 167–227°and 347–46°are excluded for the rest of the study (also when selecting the four cases). The difference between Doppler lidar and anemometer $U_\perp$ is also large from 2000–2500 m along the Doppler lidar path (indicated in light red in Fig. 5.2b). That the Doppler lidar estimates of $U_\perp(x)$ are unreliable for this part of the path is more clearly visible in Fig. 5.3, where the average horizontal wind speed (U) and the crosswind speed along the path as estimated by the Doppler lidar are shown. Note in order to make this figure the near-parallel wind direction are excluded as data where the Doppler lidar reached less than 70 % of the total path. The value of $U_\perp(x)$ even changes sign at the 2000–2500 m section along the Doppler lidar path. The error in $U_\perp(x)$ for this section of the path is probably caused by differences in the wind fields measured by the two beams, since the 196°-beam passes near to a high church tower (Kallio, about 93 m asl) which is located 35 m from the 196°-beam and at 2300 m distance

from the Doppler lidar (see Fig. 5.1b). Although the church tower is somewhat to the east of the Doppler lidar path it apparently has a significant influence on the wind-field estimated by the Doppler lidar. The church alters the wind field of one of the Doppler lidar path (196°), while the other beam (174°) does not encounter this alteration. Thus, the wind field sampled by the two Doppler lidar beams are not homogeneous, which causes problems for the duo-beam method. Therefore, we also excluded $U_\perp(x)$-values estimated by the Doppler lidar from 2000–2500 m for the evaluation of scintillometer estimates with Doppler lidar estimates. However, in order to evaluate the response of a variable $U_\perp(x)$ on $S_{11}(f)$ and $r_{12}(\tau)$, and thereby on $\overline{U_\perp}$ estimated by the scintillometer, the four selected cases need the complete $U_\perp(x)$ of the scintillometer path. Therefore, when selecting the four cases the value of $U_\perp(x)$ had to be below $1.5 \cdot \overline{U_\perp}$ (of the Doppler lidar estimates) for 2000 m $\leq x \leq$ 2500 m.

Although, the data where the wind direction was 167–227°or 347–46°are excluded, as are the data 2000–2500 m along the Doppler lidar path, there are still enough data-points left for the comparison between Doppler lidar and scintillometer. The exclusion resulted in 1288 10-min data-points (60 % of the data) for the comparison between Doppler lidar and scintillometer. For the four cases, the complete scintillometer path had to be covered by the Doppler lidar. The four cases selected are indicated in Fig. 5.2. These cases are spread over the measurement period, and have different $\overline{U_\perp}$ values. The results of the four cases are presented in Section 5.4.3.

5.4.2 Path-averaged crosswinds

In this section, $\overline{U_\perp}$ obtained by the scintillometer is compared to that of the Doppler lidar. Note that the scintillometer path and the Doppler lidar duo-beam setup are not sampling the same part of the atmosphere exactly (see Fig. 5.1). Therefore, a perfect one-to-one correlation cannot be expected. However, the height difference between the scintillometer and the Doppler lidar beam causes a negligible difference in the $\overline{U_\perp}$ estimates. Assuming a neutral wind profile the difference in $\overline{U_\perp}$ is merely 1.1 % (with a higher $\overline{U_\perp}$ estimate of the scintillometer), which assures that the height difference between the two measurement devices should not influence the comparison. Note that this 1.1 % is only an approximation, in reality the comparison is more complicated since part of the measurements are done just above the urban canopy layer where logarithmic wind profiles are not applicable.

Before looking into detail in the comparison between the Doppler lidar and scintillometer estimates of $\overline{U_\perp}$, we first show a time series of $U_\perp$ as estimated by scintillometer, Doppler lidar, and sonic anemometer (Fig. 5.4). For the scintillometer estimates it is clear that the cumulative spectrum method and lookup table method give very

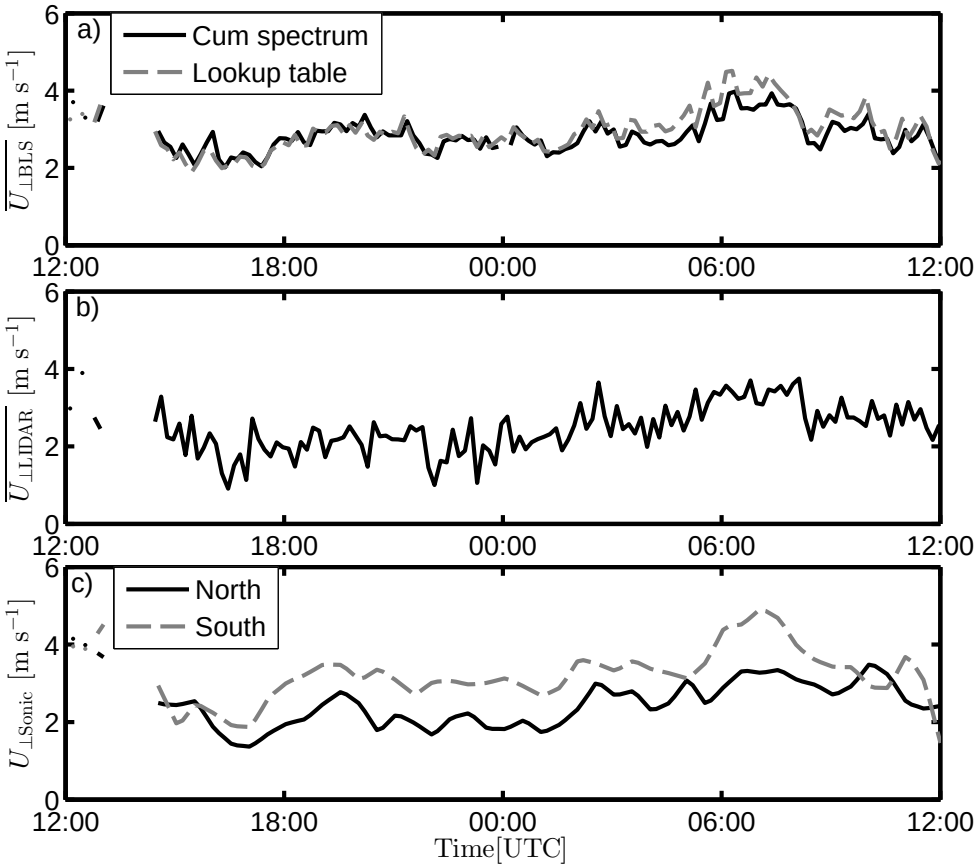

Figure 5.4: Time series of $U_\perp$ as estimated by (a) the scintillometer, (b) the Doppler lidar, and (c) the sonic anemometer for DOY 279 and 280.

similar results. The Doppler lidar estimates of $\overline{U_\perp}$ fluctuates more strongly than both the scintillometer and sonic anemometers. However, the Doppler lidar does capture the same pattern in $\overline{U_\perp}$ as the scintillometer (especially on DOY 180 from 6:00 UTC onwards). For the sonic anemometers it is apparent that they do measure a different value of $U_\perp$, which indicates that there is indeed spatial variability of $U_\perp$ for this instance.

For the comparison of the Doppler lidar and scintillometer we first focus on the result of the cumulative spectrum method (Fig. 5.5a). Note that the plots in Fig. 5.5 are colored with the standard deviation path-averaged by the scintillometer path-weighting function ($\overline{\mathrm{STD}_{\mathrm{U}\perp}}$, i.e., fluctuations of $U_\perp(x)$ in the middle of the path

contribute more to $\overline{\mathrm{STD}_{\mathrm{U}\perp}}$ than those at the ends of the path). Recall that the sign of $\overline{U_\perp}$ is unknown with the cumulative spectrum method, and thus the absolute values of $\overline{U_\perp}$ are compared to each other. There is an encouraging correlation between $\overline{U_\perp}$ of the scintillometer and Doppler lidar, with an RMSD of 0.73 m s^{-1}. However, for higher path-weighted standard deviation along the scintillometer path ($\overline{\mathrm{STD}_{\mathrm{U}\perp}}$), more scatter occurs between the scintillometer and Doppler lidar estimates. Only taking into account the data points where $\overline{\mathrm{STD}_{\mathrm{U}\perp}} > 2$ m s^{-1} leads to an R^2 value of 0.32 and an RMSD of 0.86 m s^{-1}. This higher scatter indicates the difficulty of obtaining $\overline{U_\perp}$ when the wind field is more variable along the path. An RMSD of 0.73 m s^{-1} is relatively low compared to other studies. For measurements in London (Wood *et al.*, 2013c) for comparable wind conditions, horizontal wind speed RMSDs were found of 0.35 m s^{-1} between two sonic anemometers on the same mast, 0.71–0.73 m s^{-1} between two sonic anemometers on different masts, 0.65–0.68 m s^{-1} between Doppler lidar and sonic anemometers. And for $\overline{U_\perp}$, Wood *et al.* (2013c) found an RMSD of 1.12–2.13 m s^{-1} between scintillometer and Doppler lidar. For a flat grassland site, where $U_\perp(x)$ can be assumed to be rather homogenous, van Dinther *et al.* (2013) and van Dinther & Hartogensis (2014) showed RMSD values of quality-checked data of 0.41–0.67 m s^{-1} between a scintillometer and sonic anemometer for similar $\overline{U_\perp}$-conditions (in absolute values is between 0 and 6 m s^{-1}. Therefore, we can conclude, that despite the higher scatter for variable $U_\perp(x)$-conditions, both measurement techniques seem able to obtain $\overline{U_\perp}$ in this challenging environment. In Fig. 5.5b, $\overline{U_\perp}$ obtained by the lookup table method is compared to the Doppler lidar estimates. Note that the following regression statistics are obtained when absolute $\overline{U_\perp}$-values are considered for the lookup table method: RMSD of 0.73 m s^{-1}, $y = 0.76x + 0.83$, and $R^2 = 0.53$ Just like the cumulative spectrum method, there is a clear correlation between $\overline{U_\perp}$ estimated by the scintillometer and that estimated by the Doppler lidar. Considering the regression statistics of the absolute $\overline{U_\perp}$ are very similar with the same RMSD and similar regression equation (slightly better fit for the lookup table method). The scatter of $\overline{U_\perp}$ of the lookup table method with the Doppler lidar estimates is somewhat lower than that of the cumulative spectrum method with an R^2-value of 0.53 compared to 0.47. For the lookup table, the scatter is also higher (R^2 of 0.37 and RMSD of 0.88 m s^{-1}) when $U_\perp(x)$ is very variable ($\overline{\mathrm{STD}_{\mathrm{U}\perp}} > 2$ m s^{-1}).

Overall, both scintillometer methods are able to obtain a similar $\overline{U_\perp}$ as the Doppler lidar. This indicates that both the Doppler lidar and scintillometer are able to obtain $\overline{U_\perp}$ over the complex urban environment. However, bear in mind that in order to achieve these results certain wind directions and a certain section of the path were not take into account (see Section 5.4.1). The lookup table method showed the best results, with the lowest RMSD and scatter.

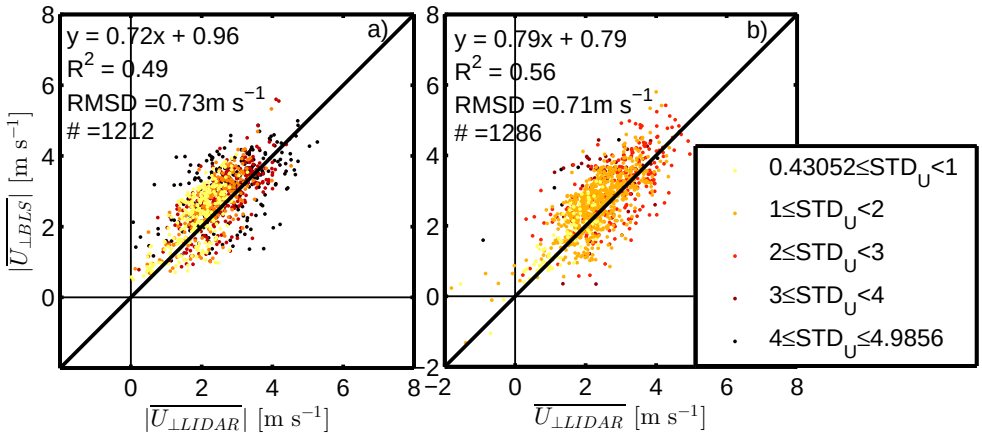

Figure 5.5: (a) Crosswind 10-min averages estimated by the scintillometer ($\overline{U_{\perp\mathrm{Scint}}}$) using the cumulative spectrum method against Doppler lidar crosswind ($\overline{U_{\perp\mathrm{Lidar}}}$). (b) Crosswind estimated by the scintillometer using the lookup table method against Doppler lidar data. Both plots are color coded with the Doppler lidar-derived path weighted standard deviation of the crosswind along the 4.2 km path (see legend). The one-to-one lines are shown in thick black.

5.4.3 Variable crosswinds along the path

Four cases were selected to investigate the influence of a variable $U_\perp(x)$ on $S_{11}(f)$ and $r_{12}(\tau)$; A, B, C, and D (see top panels Fig. 5.6 and Table 5.1). As a measure of the variability of $U_\perp(x)$, the weight-averaged standard deviation of $U_\perp(x)$ is normalized by $\overline{U_\perp}$ ($\overline{\mathrm{STD}_{\mathrm{U}\perp *}}$). For the four cases, the theoretical $S_{11}(f)$ and $r_{12}(\tau)$ are calculated using Eq. (5.1) and Eq. (5.3), respectively.

We first focus on the cumulative scintillation spectra (CS, given in the middle panels of Fig. 5.6). Remember that the cumulative spectrum method determines $\overline{U_\perp}$ from the frequencies where the CS is 0.5, 0.6, 0.7, 0.8, and 0.9. Therefore, in Fig. 5.6 the cumulative spectra are zoomed into these points. For simplicity we abbreviate the cumulative spectrum obtained from the scintillometer as $\mathrm{CS}_{\mathrm{scint}}$, the cumulative spectrum obtained from Eq. (5.1) using $U_\perp(x)$ of the Doppler lidar as $\mathrm{CS}_{\mathrm{varU}\perp}$, and the cumulative spectrum obtained from Eq. (5.1) using $\overline{U_\perp}$ of the Doppler lidar as $\mathrm{CS}_{\mathrm{constU}\perp}$.

There is a difference between $\mathrm{CS}_{\mathrm{varU}\perp}$ and $\mathrm{CS}_{\mathrm{constU}\perp}$ for all four cases. Therefore, the CS is indeed influenced by a variable $U_\perp(x)$ as was suggested by van Dinther *et al.* (2013). Recall that when a CS-point shifts to a higher frequency, the retrieved value of $\overline{U_\perp}$ will be higher; and the other way around (see Eq. (5.2)). The CS-points

Table 5.1: Crosswind for the four cases estimated by the Doppler lidar, and scintillometer (using either cumulative spectra, CS, or time-lagged correlation function, $r_{12}(\tau)$). $\overline{U_{\perp \mathrm{varU}\perp}}$ is given by the theoretical CS and $r_{12}(\tau)$ using the variable $U_\perp(x)$ estimated by the Doppler lidar.

Case	DOY	HH:MM (UTC)	Doppler lidar		CS		$r_{12}(\tau)$	
			$\overline{U_\perp}$ m s^{-1}	$\overline{\mathrm{STD}_{\mathrm{U}\perp *}}$ m s^{-1}	$\overline{U_{\mathrm{scint}}}$ m s^{-1}	$\overline{U_{\mathrm{varU}\perp}}$ m s^{-1}	$\overline{U_{\mathrm{scint}}}$ m s^{-1}	$\overline{U_{\mathrm{varU}\perp}}$ m s^{-1}
A	276	19:47	2.8	0.36	3.5	2.6	3.2	2.5
B	280	06:57	3.3	0.39	3.4	3.1	4.1	3.0
C	283	22:57	1.6	0.63	1.6	1.4	0.8	0.8
D	286	04:27	3.9	0.41	3.5	3.9	3.1	3.1

of 0.5, 0.6, and 0.7 lie at lower frequencies for $\mathrm{CS}_{\mathrm{varU}\perp}$ than for $\mathrm{CS}_{\mathrm{constU}\perp}$, while the 0.9 CS-point lies at higher frequencies. $\mathrm{CS}_{\mathrm{scint}}$ is more similar to $\mathrm{CS}_{\mathrm{varU}\perp}$ than to $\mathrm{CS}_{\mathrm{constU}\perp}$, which indicates that Eq. (5.1) is also applicable when $U_\perp(x)$ is variable.

The results of applying the cumulative spectrum method to $\mathrm{CS}_{\mathrm{scint}}$ and $\mathrm{CS}_{\mathrm{varU}\perp}$ are given in Table 5.1. If the assumption of the cumulative spectrum methods, that C_{CS} of Eq. (5.2) is constant, also holds for variable $U_\perp(x)$, then the value of $\overline{U_\perp}$ of the Doppler lidar should be identical to that of $\overline{U_{\mathrm{CSvarU}\perp}}$. For case D this is indeed true.

However, for cases A, B, and C $\overline{U_{\mathrm{CSvarU}\perp}}$ is 0.2 m s^{-1} lower than $\overline{U_{\mathrm{Lidar}}}$. Therefore, the assumption that C_{CS} is constant does not hold. However, the error that is made in $\overline{U_\perp}$ is small (0.2 m s^{-1}), and is due to the cumulative spectrum method calculating $\overline{U_\perp}$ for five frequency points and then averaging these to obtain one value for $\overline{U_\perp}$ (see Section 5.2.1.1). For the 0.5, 0.6, and 0.7 CS-points, $\overline{U_{\mathrm{CSvarU}\perp}}$ is underestimated; while for the 0.9 CS-point, $\overline{U_{\mathrm{CSvarU}\perp}}$ is overestimated. Therefore, applying a method with only one frequency point to obtain $\overline{U_\perp}$ is more likely to have a higher error. This makes the cumulative spectrum method the most suitable method to obtain $\overline{U_\perp}$ from $S_{11}(f)$ when $U_\perp(x)$ is variable, compared to other methods suggested by van Dinther *et al.* (2013). Alternatively, to obtain $\overline{U_\perp}$ even more reliably from $S_{11}(f)$ in variable $U_\perp(x)$ conditions, an approach similar to the lookup table method can be applied. A lookup table can be created of the theoretical CS for different $\overline{U_\perp}$-values and also different variabilities of $U_\perp(x)$.

Next we focus on the results of the lookup table method, which relies on $r_{12}(\tau)$ to obtain $\overline{U_\perp}$ (given in the bottom panels of Fig. 5.6). For all cases, except case B, there is a substantial difference in magnitude between $r_{12\ \mathrm{varU}\perp}(\tau)$ (grey solid lines) and $r_{12\ \mathrm{constU}\perp}(\tau)$ (grey dashed lines). However, the magnitude of $r_{12}(\tau)$ does not influence $\overline{U_\perp}$ obtained by the lookup table method, but the shape of $r_{12}(\tau)$ does. The

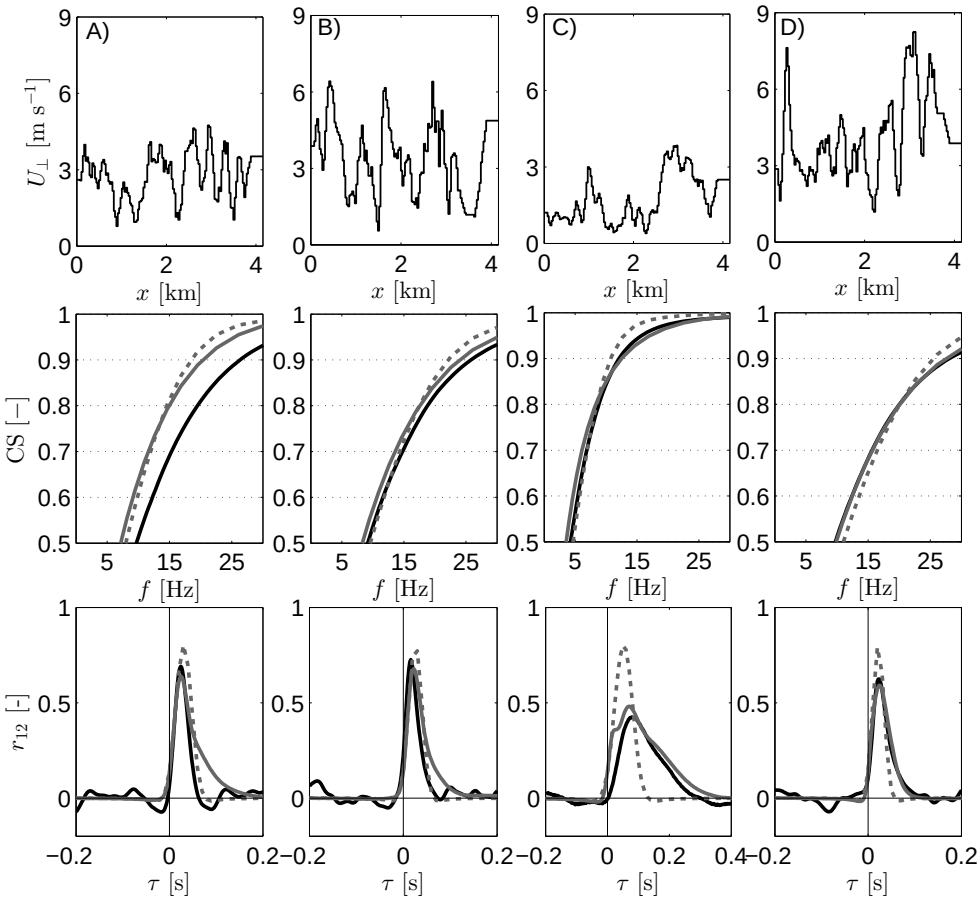

Figure 5.6: Four cases (A, B, C, and D) with in the top panels the transect of $U_\perp(x)$, in the middle panels the corresponding CS, and in the lower panels the corresponding $r_{12}(\tau)$. The estimated CS and $r_{12}(\tau)$ of the scintillometer are given in black solid lines, the theoretical CS and $r_{12}(\tau)$ given $U_\perp(x)$ of the Doppler lidar are given in solid grey lines, and the theoretical CS and $r_{12}(\tau)$ given $U_\perp(x) = \overline{U_\perp}$ are given in dashed grey lines.

shape of $r_{12}(\tau)$ also changes when $U_\perp(x)$ is variable: it becomes wider. For cases C and D $r_{12\ \mathrm{varU}\perp}(\tau)$ resembles $r_{12\ \mathrm{scint}}(\tau)$ clearly better than $r_{12\ \mathrm{constU}\perp}(\tau)$. This resemblance indicates that the theoretical model of Lawrence *et al.* (1972) (Eq. (5.3)) can be used to obtain $r_{12}(\tau)$ also given a variable $U_\perp(x)$. The fact that variable $U_\perp(x)$ causes a wider $r_{12}(\tau)$ can cause an underestimation of $\overline{U_\perp}$ obtained by the scintillometer, since a wider $r_{12}(\tau)$ is normally associated with lower $\overline{U_\perp}$-values. For

the four cases selected in this study $\overline{U_\perp}$ calculated from $r_{12\ \mathrm{varU}\perp}$ is indeed lower than $\overline{U_\perp}$ estimated by the Doppler lidar (see Table 5.1). The error is in this study defined as the difference between $\overline{U_\perp}$ estimated by the Doppler lidar and $\overline{U_\perp}$ obtained from $r_{12}(\tau)$. For cases C and D the error is higher with a value of 0.8 m s^{-1}. This high error is caused by the fact that for these two cases $r_{12}(\tau)$ is not only lowered by the variable $U_\perp(x)$, but the peak in $r_{12}(\tau)$ also changes location and $r_{12}(\tau)$ becomes much wider due to the variable $U_\perp(x)$. For these cases $\overline{\mathrm{STD}_{\mathrm{U}\perp *}}$ is also high with values of 0.63 and 0.41, respectively. Although the error with the Doppler lidar estimates is high for case C and D, the estimated $\overline{U_{\perp\mathrm{scint}}}$ of the lookup table method are for these cases exactly identical to that of $r_{12\mathrm{varU}\perp}(\tau)$. Therefore, if the lookup table was expanded to also including variable $U_\perp(x)$ field the results of the lookup table method in a more challenging environment could be improved. The underestimation of $\overline{U_\perp}$ given in the cases is however not clearly visible in the comparison between Doppler lidar and scintillometer (see Section 5.4.2 Fig. 5.5). Although, we do see that a higher $\overline{\mathrm{STD}_{\mathrm{U}\perp}}$ causes more scatter between $\overline{U_\perp}$ of the scintillometer and Doppler lidar.

From the analysis of these four cases, it follows that the present cumulative spectrum method is better equipped to obtain $\overline{U_\perp}$ than the lookup table method. However, as mentioned before the lookup table method can be adjusted to take into account the variability of $U_\perp(x)$. The underestimation of $\overline{U_\perp}$ found for the four cases for both methods was not clearly distinguishable in Section 5.4.2. Though more scatter occurred between $\overline{U_\perp}$ estimated by scintillometer and Doppler lidar when $\overline{\mathrm{STD}_{\mathrm{U}\perp}}$ was high (> 2 m s^{-1}).

5.5 Conclusions and outlook

In this study, estimates of $U_\perp$ above the urban environment of Helsinki from sonic anemometers and Doppler lidar data were compared with scintillometer data. The anemometers measured at either ends of the scintillometer path, and the Doppler lidar was measuring alongside the scintillometer path. For the Doppler lidar duo-beam method, sign problems of $U_\perp$ naturally occurred when the wind direction was parallel to the scintillometer path (167–227°and 347–47°). In the middle of the path (2000–2500 m) a church tower near one of the Doppler lidar beams resulted in problems, presumably because of the heterogeneity it introduced in the wind field. Therefore, for the comparison with the scintillometer these points were excluded.

For the scintillometer, two different methods were tested: the cumulative spectrum method (van Dinther *et al.*, 2013), based on $S_{11}(f)$, and the lookup table method (van Dinther & Hartogensis, 2014), based on $r_{12}(\tau)$). Both methods gave similar results as the Doppler lidar estimates, although with scatter between the Doppler lidar and the

scintillometer (especially for conditions where $\overline{\mathrm{STD}_{\mathrm{U}\perp}} > 2$ m s^{-1}). Still, given that the Doppler lidar and scintillometer did not sample over exactly the same area in this urban environment, the good fit and low RMSD ($\leq$ 0.73 m s^{-1}) indicate that both measurement devices are able to obtain $\overline{U_\perp}$, given the data treatment applied in this study,. For the scintillometer the method relying on $r_{12}(\tau)$ (lookup table method) is preferable, since $r_{12}(\tau)$ is determinable over short time scale ($\sim$ 10 s) compared to scintillation spectra ($\sim$ 10 min) and it also includes information about the sign of $\overline{U_\perp}$.

Four cases were selected to investigate the influence of a variable $U_\perp(x)$ on $\overline{U_\perp}$ estimated by the scintillometer. Variability of $U_\perp(x)$ causes only a slight difference between $\overline{U_\perp}$ obtained by the cumulative spectrum method and Doppler lidar (error $\leq$ 0.2 m s^{-1}). $r_{12}(\tau)$ was more affected by a variable $U_\perp(x)$-field than $S_{11}(f)$ leading to higher errors in $\overline{U_\perp}$ obtained by the lookup table method (error $\leq$ 0.8 m s^{-1}). The lookup table method can however, be adjusted to include heterogeneous wind fields; thereby, probably making the scintillometer more suitable to obtain $\overline{U_\perp}$ in a more challenging environment.

In this study the focus was on the influence of spatial variability of $U_\perp(x)$ on scintillometer $\overline{U_\perp}$ estimates. However, temporal variability of $U_\perp(x)$ will also influence the estimates of $\overline{U_\perp}$. We expect that this temporal variability has the same influence as the spatial variability; a smoothing of $S_{11}(f)$ and a widening of $r_{12}(\tau)$. However, methods that rely on $r_{12}(\tau)$ are likely not affected by temporal variability of $U_\perp(x)$, since $r_{12}(\tau)$ is determined over a reasonable short time interval ($\sim$ 10 s). Methods that rely on $S_{11}(f)$ are more likely to be affected by a temporal variability of $U_\perp(x)$, since $S_{11}(f)$ is determined over a relatively long time interval ($\sim$ 10 min).

In the future, by applying two scintillometers with paths perpendicular to each other, not only $\overline{U_\perp}$ could be obtained, but also the wind direction and horizontal wind speed (Andreas, 2000). Thereby, obtaining an area-averaged value of the horizontal wind speed and wind direction above an urban environment. Compared to a Doppler lidar the scintillometer is less expensive and easier to use. An path-averaged value of wind direction and horizontal wind speed would be directly useful for nowcasting for meteorology and for atmospheric composition (AC); and also in the development of models of AC and numerical weather prediction.

Acknowledgements

The authors would like to thank Leena Järvi, Rostislav Kouznetsov, Anne Hirsikko, and Ville Vakari for their help with instrumental setup and preliminary data analysis; and Kari Riikonen, Erkki Siivola, Petri Keronen, and Sami Haapanala for their technical support. Daniëlle van Dinther and Oscar Hartogensis were supported by the

Knowledge for Climate project Theme 6 entitled "High Quality Climate Projections" (KVK-HS2). Curtis Wood was supported by the EC FP7 ERC Grant 227915 "Atmospheric planetary boundary layers: Physics, modelling and role in Earth system". We would also like to thank the anonymous reviewers for their valuable comments, which helped to improve the quality of the manuscript.

6

Runway wake vortex, crosswind, and visibility detection with a scintillometer at Schiphol airport

This study investigates the capability and performance of a scintillometer to detect wake vortices, crosswind, and visibility near an airport runway. An experiment was carried out at Schiphol airport (Amsterdam, the Netherlands), where an optical scintillometer was setup alongside a runway. An algorithm was developed to detect wake vortices, and also the strength of the wake vortex, from the variance in the scintillation signal. The algorithm showed promising results in detecting wake vortices and their strengths during the night. During the day, the scintillometer signal is dominated by environmental turbulence and the wake vortices are no longer detectable. The crosswind measured by the scintillometer is compared to wind anemometer and wind vane data at the airport. Our results show that, after applying an outlier filter, the scintillometer is able to measure the crosswind over a short time period of 3 s. The outlier filter did not comprise the capability of the scintillometer to obtain the maximum crosswind over the last 10 min correctly. Finally, a transmission method is used to obtain the visibility from the scintillometer signal. The visibility measured by the scintillometer are compared to that obtained from a visibility sensor. The scintillometer was able to quantify the visibility correctly, albeit with a high amount of scatter, for practically relevant cases in which the visibility dropped below 10 km.

This chapter is under review at the Boundary-Layer Meteorology journal.

6.1 Introduction

The safety of airplanes landing and taking off is dependent on critical weather and environmental conditions. Examples are strong crosswinds, strong tailwinds, heavy fog, rain events, and wake vortices created by other airplanes. In order to minimize the risk of accidents airplane operations are limited to certain weather conditions. Most weather conditions are monitored by point measurements, which can be affected by local conditions or ground clutter close by. Therefore, the measurements may not be representative for the weather conditions on the runway. In this study, we present a line-averaged measurement technique with an optical scintillometer to detect wake vortices, crosswind, and visibility near an airport runway.

A scintillometer consists of a transmitter and receiver, typically spaced a few hundred meters to a few kilometers apart. The transmitter emits light with a certain wavelength, which is refracted by the turbulent eddy field in the atmosphere resulting in light intensity fluctuations at the receiver side. The more turbulent the atmosphere, the more vigorous the intensity fluctuations in the scintillometer signal. These intensity fluctuations can be linked to surface fluxes, since exchange of heat causes more turbulence in the atmosphere. Obtaining path-averaged surface fluxes has been the main application of scintillometers so far (among others Green *et al.*, 2001; Meijninger & de Bruin, 2000).

In this study we will investigate the applicability of a scintillometer to detect wake vortices. The lift of the wings of airplanes creates wake vortices, which can create safety issues for a following airplane landing or taking off. Therefore, there are rules concerning the separation in between two airplanes landing or taking off (Gerz *et al.*, 2002). However, these rules limit airport capacity. A monitoring system for wake vortices can help to ensure airport safety and increase airport capacity. Various studies (among others Harris *et al.*, 2002; Gerz *et al.*, 2005; Holzäpfel & Steen, 2007) focus on Doppler lidar measurements to detect wake vortices. However, Doppler lidars have problems with retrieving values of the wind near the ground surface, since the return signal of the ground also influences the signal (Godwin *et al.*, 2012). Wake vortices can also be obtained from an array of sonic anemometers (Hallock & Osgood, 2003). However, in order to do so a large array of sonic anemometer are necessary (in the study of Hallock & Osgood (2003) a sonic every 50 m). A scintillometer with one transmitter and one receiver should suffice to detect wake vortices along the touch down or take off zone.

Regarding the crosswind, different studies already showed that a scintillometer is very useful in obtaining it (among others Lawrence *et al.*, 1972; Wang *et al.*, 1981; Poggio *et al.*, 2000). The crosswind ($U_{\perp}$) is the wind component perpendicular to

a path. Most of the validation studies for a scintillometer measuring $U_\perp$ took place over flat grass land fields (among others Poggio *et al.*, 2000; van Dinther *et al.*, 2013; van Dinther & Hartogensis, 2014), over which $U_\perp$ can be assumed constant along the scintillometer path. Around airport runways the scintillometer signal will be affected by the turbulence induced by airplanes. In this study, we will therefore investigate if the algorithms to obtain $U_\perp$ from scintillometer measurements are still applicable near airport runways. In aviation, $U_\perp$ is required at a time-scale of 3 s, while previous studies that obtained $U_\perp$ from scintillometers used timescale in the order of 10 s (van Dinther & Hartogensis, 2014). In this study, we will test if $U_\perp$ can be obtained from a scintillometer over 3 s time-scales.

Fog at airports can cause delays and thereby limit airports capacity (among others Robinson, 1989; van der Velde *et al.*, 2010). Nowadays, fog is at airports in general measured by point measurements (e.g., transmissometer). We will investigate the possibility of a scintillometer to obtain a path-averaged value for the visibility. Fog results in a lowering of the scintillation signal, since the water particles in the air of fog scatter the light, so that the light transmitted by the transmitter is not captured by the receiver (Earnshaw *et al.*, 1978). Potentially, the drop in the scintillometer signal can be linked to the visibility.

Thus the goal of this study is to investigate the feasibility and performance of a scintillometer to detect wake vortices, crosswind, and visibility. The investigation is carried out on scintillometer data collected in the summer of 2013 near a busy runway at Schiphol airport in Amsterdam, the Netherlands.

6.2 Theory

A scintillometer consists of a transmitter and a receiver. The receiver measures light intensity fluctuations that are caused by the turbulent atmosphere the light travels through. The turbulent eddy field in between the transmitter and receiver is constantly changing, due to eddy decay and transport by the wind. A scintillometer measures over very small time-scales (measurement frequency of 500 Hz), which makes Taylor's frozen turbulence hypothesis applicable (i.e., the eddy-field does not change while it is being transported through the scintillometer path). The only driver of changes in eddy field is therefore the wind. Given the path-length of scintillometers (a few hundred meters to a few kilometers) the sole driver is actually the crosswind ($U_\perp$). The background theory of the three subjects investigated (wake vortices, crosswind, and visibility) is briefly described in the sections below.

6.2.1 Wake vortices

The lift force exerted on the wing of an airplane creates wake vortices, which develop the following way. First a strong downward motion develops behind the trailing edge of the wing, while a weaker upward motion develops behind the wing tips (Gerz *et al.*, 2002). Therefore, small spiraling motions develop at the wing tips and landing flap. These small motions through a phenomenon known as roll-up develop into the wake vortex with single- and double-branched spirals (Krasny, 1987). The strength of the circulation of a wake vortex is proportional to the weight of the airplane and the order of wing span (Gerz *et al.*, 2002).

Wake vortices deform and weaken, and thereby decay under the influence of secondary vorticity structures (Holzäpfel *et al.*, 2003). There are multiple quantities that influence the lifetime and trajectory path of wake vortices, such as ambient wind, turbulence, wind shear and turbulence stratification (Gerz *et al.*, 2005). Besides these quantities, near the ground wake vortices can separate and rebound leading to decay of the wake vortex (Robins & Delisit, 1993). Robins & Delisit (1993) found that in stable conditions wake vortices are able to survive up to 3.5 min and travel perpendicular under the influence of the crosswind. Unfortunately, they did not state information about the lifetime of wake vortices near the ground for unstable conditions. The long lifetime in stable conditions makes it possible for wake vortices to be transported from one runway to a neighboring runway, thus making a wake vortex detection system crucial for airports safety.

6.2.2 Crosswind

Different methods exist to obtain scintillometer based $U_\perp$ which rely either on scintillation spectra or the time-lagged correlation function ($r_{12}(\tau)$). Scintillation spectra can be obtained from a single-aperture scintillometer, while $r_{12}(\tau)$ needs to be obtained from a dual-aperture scintillometer (i.e., two spatially separated scintillometers). The benefit of $r_{12}(\tau)$ is that it can be obtained over shorter time scales than scintillation spectra ($\sim$ 10 s compared to $\sim$ 10 min) (van Dinther & Hartogensis, 2014). Furthermore, from $r_{12}(\tau)$ also the sign of $U_\perp$ (i.e., the side from which the wind blows into the scintillometer path) can be obtained. For the application at airports $U_\perp$ needs to be obtained over a short time scale (3 s), which is necessary to determine the wind gust and wind lull. Therefore, in this study a method relying on $r_{12}(\tau)$ will be used.

The values of $r_{12}(\tau)$ are obtained from a dual-aperture scintillometer by shifting one of the two signals in time and calculating the correlation between the two signals. In theory the two signals should be identical at a certain time-lag, since the eddy field

does not change while it is being transported from the one scintillometer to the other. The higher $U_\perp$ the smaller the time-lag in between the two signals.

Lawrence *et al.* (1972) developed a theoretical model for the time-lagged covariance function ($C_{12}(\tau)$), based on earlier work of Tatarskii (1961). Including the aperture averaging terms of a large aperture scintillometer (Wang *et al.*, 1981) the theoretical model of Lawrence *et al.* (1972) reads:

$$C_{12}(\tau) = 16\pi^2 k^2 \int_0^1 \int_0^\infty K\phi_n(K) \sin^2\left[\frac{K^2 Lx(1-x)}{2k}\right] J_0\{K[s(x) - U_\perp(x)\tau]\} \left[\frac{2J_1\big(0.5KD_\mathrm{R}x\big)}{0.5KD_\mathrm{R}x}\right]^2 \left\{\frac{2J_1\big[0.5KD_\mathrm{T}(1-x)\big]}{0.5KD_\mathrm{T}(1-x)}\right\}^2 dKdx, \quad (6.1)$$

where k is the wave number of the emitted radiation, K the turbulent spatial wave number, $\phi_n(K)$ is the three-dimensional spectrum of the refractive index in the inertial range given by Kolmogorov (1941), L is the scintillometer path length, x is the relative location on the path, J_0 is the zero-order Bessel function, $s(x)$ is the separation distance between the two beams at location x along the path, τ is the time-lag, J_1 is the first-order Bessel function, D_R is the aperture diameter of the receiver, and D_T is the aperture diameter of the transmitter. From Eq. 6.1 the theoretical variance (C_{11}) can also be calculated by taking $s(x) = 0$ m and $\tau = 0$ s. The theoretical $r_{12}(\tau)$ can be obtained by dividing the theoretical $C_{12}(\tau)$ by the theoretical C_{11}. Hereby, it is assumed that $C_{11} = C_{22}$, which is the case when D_R and D_T are the same for the two scintillometers.

6.2.3 Visibility

Different types of visibility sensors exist, which rely on different methods to obtain the visibility. The most classical is the transmission method where a transmitter and receiver are aligned over a certain path. The receiver measures the amount of light left after the transmitted light traveled over a path. Other methods rely on forward and backscattering to measure the visibility. A scintillometer uses the transmission method, since the transmitter and receiver are directly aligned.

Visibility measurement devices in general use the Lambert-Beer law, which describes the extinction of light by refraction and absorption in a medium. This law written for a scintillometer reads:

$$I_\mathrm{R} = I_\mathrm{T} e^{-aL}, \quad (6.2)$$

where I_R is the light intensity measured by the receiver of the scintillometer, I_T is the light intensity emitted by the transmitter, and a is the attenuation coefficient.

The coefficient a is a measure of the amount of attenuation due to absorption and the scattering of the light in the atmosphere (Vogt, 1968). This absorption or scattering can be caused by different quantities e.g., dust, water droplets, and aerosols.

In order to ensure a detectable signal over a range of scintillometer measurement paths (for a large aperture scintillometer typically 500–5000 m) either I_R or I_T of a scintillometer can be adjusted. In case of the scintillometer used in this study (BLS900, Scintec, Rottenburg, Germany), I_R is adjusted through discrete attenuation settings in order to ensure a suitable level of I_R for scintillometer measurements.

Koschmieder (1924) was the first to link visibility (V) to a, by stating that during day-light conditions 2 % of the light had to be detected by a receiver in order for a human eye to detect an object. Thereby, making the so-called transmission factor (T, which is given by $\frac{I_\mathrm{R}}{I_\mathrm{T}}$) 0.02. Applying the concept of $L = V$ for $T = 0.02$ to Eq. 6.2 gives

$$V = \frac{-\ln 0.02}{a}. \tag{6.3}$$

A quantity often used in aviation to describe the visibility is the Meteorological Optical Range (MOR). MOR is defined as the limit were at least 5 % of the light is received, leading to (Werner *et al.*, 2005)

$$\mathrm{MOR} = \frac{-\ln 0.05}{a} \approx \frac{3}{a}. \tag{6.4}$$

Equation 6.4 gives the relation between MOR and a. Substituting this a in Eq. 6.2 we end of with the following expression for MOR

$$\mathrm{MOR} = \frac{L \cdot \ln 0.05}{\ln\left(\frac{I_\mathrm{R}}{I_\mathrm{T}}\right)}. \tag{6.5}$$

In Eq. 6.5, MOR is expressed in terms of the scintillometer controlled and measured quantity: I_T and I_R.

6.3 Methods

6.3.1 Wake-vortex detection

Wake vortices create extra turbulence around the airport's runway, and thus leave a trace in the scintillation signal, making it potentially possible to determine them with a scintillometer. The variance of the log of the light intensity measured by the receiver ($\sigma^2_{\ln I}$) is a measure for the amount of turbulence in between the scintillometer's transmitter and receiver. Hence, $\sigma^2_{\ln I}$ should increase when a wake vortex is located in the scintillometer path. In order to determine if a wake vortex is present the value of $\sigma^2_{\ln I}$

is compared to the running median $\sigma^2_{\ln I}$ of the previous 5 min ($\overrightarrow{\sigma^2_{\ln I}}$). Thereby, it is assumed that the value of $\overrightarrow{\sigma^2_{\ln I}}$ is an approximate value of the amount of turbulence in the atmosphere without being influenced by the wake vortices. We developed an algorithm to detect a wake vortex. The algorithm consisted of the following criteria which needed to be met over a time window to be labeled as a wake vortex:

- $\sigma^2_{\ln I} > 1.8 \cdot \overrightarrow{\sigma^2_{\ln I}}$
- $\overrightarrow{\sigma^2_{\ln I}} < 2 \cdot 10^{-4}$
- $I_{\mathrm{R}} > \frac{2}{3}$ of the maximum I_{R} ($I_{\mathrm{R,max}}$)
- At least 10 consecutive points had to meet the criteria above

The criteria stated above are all in principle applicable for different scintillometer setup, except the second criteria ($\overrightarrow{\sigma^2_{\ln I}} < 2 \cdot 10^{-4}$). This criteria had to be applied, since the scintillometer is unable to detect wake vortices in an unstable atmosphere (as will be shown in Section 6.5.1). The value of $\overrightarrow{\sigma^2_{\ln I}}$ of $2 \cdot 10^{-4}$ corresponds to a value of the structure parameter of the refractive index (C_{n^2}) of $9 \cdot 10^{-15}$ m$^{-2/3}$. The value of C_{n^2} is in principal applicable for any scintillometer setup.

For the detection of the wake vortices the criteria given above worked well (as will be shown in Section 6.5.1). However, to determine the length of a wake vortex the criteria of $\sigma^2_{\ln I} > 1.8 \cdot \overrightarrow{\sigma^2_{\ln I}}$ appeared to be too strict. Therefore, for determining the duration of the wake vortex a less strict filter of $\sigma^2_{\ln I} > 1.2 \cdot \overrightarrow{\sigma^2_{\ln I}}$ is applied, which should be applicable for any scintillometer setup.

Besides detecting if a wake vortex was present we also developed an algorithm to determine the strength of a wake vortex ($\mathrm{WV_{Intensity}}$). The strength is determined from the magnitude of $\sigma^2_{\ln I}$; the stronger the wake vortex, the more turbulence the wake vortex generates and the higher $\sigma^2_{\ln I}$. The value of $\mathrm{WV_{Intensity}}$ is therefore determined by the 95 % percentile of $\sigma^2_{\ln I}$ during the wake vortex divided by the $\overrightarrow{\sigma^2_{\ln I}}$ just before the wake vortex, resulting in a $\mathrm{WV_{Intensity}}$ of arbitrary units.

No other measurement devices were recording wake vortices at the moment of the experiment, thus it is not possible to directly validate the wake vortices detected by the scintillometer with independent measurements. However, the Air Traffic Control the Netherlands (LVNL) keeps track of when and on which runway an airplane is landing or taking off. All airplanes have a wake turbulence category given by the International Civil Aviation Organization, which is either “Light”, “Medium”, “Heavy”, or “Super”, based on the weight and other specifications of the airplane. These wake turbulence category specifications together with the airport’s operations (landing or take off)

were available from day of the year (DOY) 184 until 221 in 2013. Note that during this time period only airplanes with a wake turbulence category of medium and heavy landed or took off from the runway the scintillometer was measuring at. The timing of airplanes landing and taking off together with the wake turbulence category can be used to validate the wake vortex strength and timing retrieved from the scintillation signal. In order for a detected wake vortex to be attributed to an airplane the time between the airplane landing or taking off and the detected wake vortex had to be less than 3.5 min. This is the time reported by Robins & Delisit (1993) up to which a wake vortex can survive.

From the known airplane operations we can also calculate how many wake vortices of airplanes can be detected by the scintillometer. This was achieved by using similar criteria as mentioned above to detect wake vortices, but for one minute averages from before the airplane landed or took off; the average $\sigma^2_{\ln I}$ had to be below $2 \cdot 10^{-4}$, while the average I_{R} had to be above $\frac{2}{3} \cdot I_{\mathrm{R,max}}$. The results of the wake vortex detection by the scintillometer are given in Section 6.5.1.

6.3.2 Crosswind

The crosswind is calculated from the scintillometer by using the lookup table method described in van Dinther & Hartogensis (2014). This method compares the time-lagged correlation function ($r_{12}(\tau)$) measured by a dual-aperture scintillometer to that of a lookup table with the theoretical model of Lawrence *et al.* (1972) of $r_{12}(\tau)$. The $U_\perp$-value of the theoretical $r_{12}(\tau)$ with the best fit with the measured $r_{12}(\tau)$ is the $U_\perp$-value representative for the time period. More details on the lookup table method are given in van Dinther & Hartogensis (2014).

The time window over which $r_{12}(\tau)$ is determined should according to van Dinther & Hartogensis (2014) be ∼10 s. However, as mentioned before for aviation a time-window of 3 s is necessary. In this study, $U_\perp$ was thus determined over a 3 s time window, but an outlier detection filter was applied in order to minimize the effect of not determining $r_{12}(\tau)$ over a sufficient time window. Note that in practice only a filter can be used that takes the data taken before the sample. From the $U_\perp$-measurements a running median was calculate over a period of 5 min. If the value of $U_\perp$ was 2.5 m s^{-1} more than the running median $U_\perp$ was classified as an outlier and not taken into account for further analysis.

6.3.3 Visibility

In order to measure visibility defined as the Meteorological Optical Range (MOR) with a scintillometer the Lambert-Beer law is used as stated in Eq. 6.5, which is

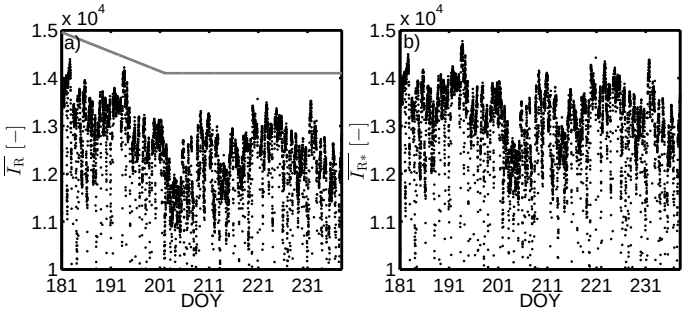

Figure 6.1: (a) Average scintillometer signal over 10 min ($\overline{I_{\mathrm{R}}}$) from day of the year (DOY) 181 till 241 in black dots zoomed into the higher values ($\overline{I_{\mathrm{R}}} \geq 1.0 \cdot 10^4$), in grey solid line the line with which $\overline{I_{\mathrm{R}}}$ was adjusted. (b) Normalized 10-min averaged scintillometer signal ($\overline{I_{\mathrm{R}*}}$) after adjusting for alignment issues from DOY 181 till 241 zoomed into the higher values ($\overline{I_{\mathrm{R}*}} \geq 1.0 \cdot 10^4$).

valid during day-light conditions. In order to determine MOR, I_{R} and I_{T} must be determined. The value of I_{R} is variable and measured by the scintillometer. The value of I_{T} is constant and needs to be determined. We calibrate I_{T} using MOR measurements of a Vaisala FD12P sensor. This calibration is valid for this type of scintillometer given the attenuation setting used in this study (see Section 6.4.1). Note that only the day-light hours are considered during this study, thus excluding the measurements in between 20:00 and 5:00 UTC for the visibility analysis.

In order to measure MOR with a scintillometer it is assumed that I_{R} is only influenced by the visibility and not by other issues (e.g., misalignment, dirty lenses). However, in Fig. **??**a it can be seen that at the beginning of the experiment the 10-min averaged I_{R} ($\overline{I_{\mathrm{R}}}$) decreases. This decrease appears in no way to be related to the visibility (not shown here), and therefore it must be caused by alignment issues. Therefore, the signal was adjusted by eye according to the grey solid line of Fig. **??**a, resulting in a adjusted 10-min averaged scintillometer signal ($\overline{I_{\mathrm{R}*}}$) given in Fig. **??**b.

6.4 Experimental set-up and data treatment

Section 6.4.1 specifies the experimental setup used in this study. In order to be able to compare the crosswind measured by the scintillometer and those collected by the Royal Netherlands Meteorological Institute (KNMI) additional data treatment had to be applied. Details on the data treatment are specified in Section 6.4.2.

6.4.1 Setup

The data were collected at Schiphol airport in the Netherlands on the so-called polderbaan runway from 26th of July till 29th of August of 2013. The runway has approximately a north-south orientation (see Fig. **??**). In this study the crosswind is defined as positive, when looking from the transmitters to the receiver, the wind is blowing from the left into the scintillometer path. For this north-south set-up the crosswind is, therefore, positive when the wind is blowing from the east.

The transmitters and receiver of a BLS900 scintillometer (Scintec AG, Rottenburg, Germany) measured over a 1060 m path at a height of 3.2 m with a geographical orientation of 177°(see Fig. **??**). Given this path length the attenuation setting of the scintillometer was set to values appropriate for a path ranging from 750 to 1500 m. The transmitters of the BLS900 emit near infrared light with a wavelength of 880 nm. The scintillometer was installed approximately 150 m from the actual runway. The measurement frequency of the BLS900 was 500 Hz, from which the raw data signal was saved.

The data of the scintillometer are compared to data collected by KNMI. They collect among other variables wind and visibility data at Schiphol. The wind data are collected by a cup anemometer and wind vane at a height of 10 m (see Fig. **??**), and contain the horizontal wind speed (U) and the wind direction (WD).

The anemometer has a measurement frequency of 4 Hz, from which the 3 s running mean data sample (U_{Sample}) is saved every 12 s, as well as maximum 3 s sample over the last 12 s, average over the last 1 min, average over the last 10 min ($\overline{U}$), maximum over the last 10 min (Max_U), minimum over the last 10 min, and standard deviation of the 3 s U values over the last 10 min (STD_U).

The wind vane measures the wind direction with a frequency of 4 Hz. The maximum change in wind direction between two samples is allowed to be 8.44°, higher difference than that threshold are probably caused by an error in the measurements. Just like U, the values of WD are saved every 12 s, which are the following quantities; average WD over the last 12 s, vectorial mean over the last 1 min, vectorial mean over the last 10 min ($\overline{\mathrm{WD}}$), maximum veering wind over the last 10 min, minimum backing wind over the last 10 min, and standard deviation of the 12 s WD over the last 10 min ($\mathrm{STD}_{\mathrm{WD}}$)

The meteorological optical range (MOR) is measured by KNMI with a Vaisala FD12P sensor at a height of about 2.5 m for every minute. This sensor uses the forward scattering method, and measures under an angle of 33°. The transmitter emits infrared light with a wavelength of 875 nm. The following quantities are saved; average over the last 1 min, average over the last 10 min ($\overline{\mathrm{MOR}}$), maximum over

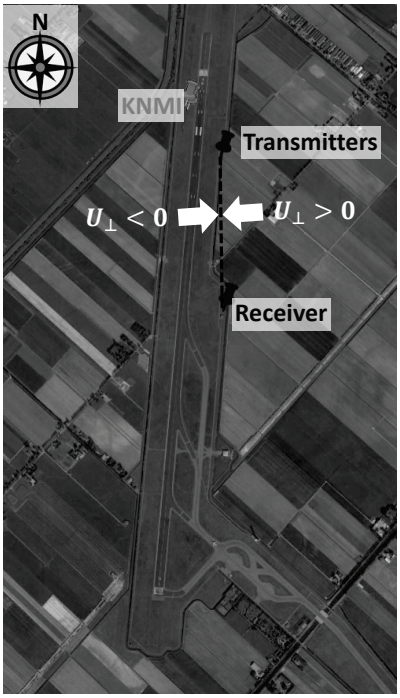

Figure 6.2: Experimental setup at Schiphol airport with the transmitters and receiver of the scintillometer indicated in black, the wind and visibility measurements of KNMI are given in grey.

the last 10 min, minimum over the last 10 min, and standard deviation of the 12 s MOR-values over the last 10 min.

6.4.2 Data treatment

The horizontal wind speed data of KNMI are corrected when the wind speed is greater then a certain threshold ($U_{\text{Threshold}}$). It is assumed that wind speeds above $U_{\text{Threshold}}$ is caused by wake vortices of airplanes. $U_{\text{Threshold}}$ is given by (Meulen, 1998):

$$U_{\text{Threshold}} = \overline{U} + C_1 \text{STD}_\text{U} + 0.5, \tag{6.6}$$

where C_1 is a constant given by 4. When $U_{\text{Sample}} > U_{\text{Threshold}}$ the horizontal wind speed can be corrected (U_{Cor}) using (Meulen, 1998):

$$U_{\text{Cor}} = \overline{U} + C_2 \text{STD}_U + 0.5, \tag{6.7}$$

where C_2 is a constant given by 2. However, Eq. 6.7 can only be applied if the following criteria are met:

- $\mathrm{STD}_U > 0.5$ m s^{-1}
- $\overline{U} > 0.5$ m s^{-1}
- $U_{\mathrm{Sample}} < 15$ m s^{-1}
- Minimum 90 % of the data are available

If the criteria above are not met U_{Sample} is not saved. Note that, unfortunately, only the corrected horizontal wind speed is saved, making it is impossible to verify the detected wake vortices of the scintillometer with the anemometer measurements.

The scintillometer measured at a height of 3.2 m, while the wind data collected by KNMI are measured at a height of 10 m. Therefore, a logarithmic wind profile was used to transpose $U_\perp$ measured by the scintillometer at a height of 3.2 m to 10 m. For simplicity we used a neutral wind profile, thereby ignoring the effect of stability. Applying the neutral wind profile gives:

$$U(10) = \frac{U(3.2)}{\ln\left(\frac{3.2}{z_0}\right)} \ln\left(\frac{10}{z_0}\right), \tag{6.8}$$

where $U(10)$ and $U(3.2)$ are the wind speed at height a height of 10 and 3.2 m respectively, and z_0 is the roughness length (z_0). In this study z_0 was assumed to be 3 cm on the flat grassland side. By applying Eq. 6.8 for $U_\perp$ we assume that the wind direction does not change in height. Note that the outlier filter specified in Section 6.3.2 is already applied before transposing $U_\perp$ measured by the scintillometer to a height of 10 m.

An important parameter for aviation is the 10-min maximum in $U_\perp$ ($\mathrm{Max}_{U\perp}$). However, $\mathrm{Max}_{U\perp}$ is not saved by KNMI, but only the maximum 10-min horizontal wind speed. In this study the value of $\mathrm{Max}_{U\perp}$ is thus calculated from Max_U and $\overline{\mathrm{WD}}$. However, given a variable wind direction during the 10-min time interval the value of $\mathrm{Max}_{U\perp}$ can be unrepresentative. Therefore, $\mathrm{Max}_{U\perp}$ was excluded from the data analysis when $\mathrm{STD}_{\mathrm{WD}} > 20°$.

6.5 Results and discussion

6.5.1 Wake-vortex detection

In this section, the results of the wake vortex detection algorithm specified in Section 6.3.1 are discussed. First, two examples of the performance of the algorithm in stable

and unstable conditions are given. Second, the wind fields are shown under which airplanes were landing and taking off for the study period. Third, the amount of detected wake vortices and amount of landings and take offs are discussed. Last, we look at the wake vortex strength, wake vortex size, and separation time between an airplane movement and the detected wake vortex.

Figure **??**a shows the wake vortices detected by the scintillometer on DOY 186 in between 3:30 and 3:50 UTC. For this time period there is a clear increase in $\sigma^2_{\ln I}$ after an airplane has landed. The wind direction and crosswind speed over this time period given the experimental setup of this study (see Section 6.4.1) transport the wake vortices to the scintillometer path. Thus, we can assume that the increase in $\sigma^2_{\ln I}$ is caused by wake vortices. However, a wake vortex is not detected for all the airplanes that land. For example, the airplane with a wake turbulence category of heavy landing on 3:34:37 UTC no wake vortex is detected. The increase of $\sigma^2_{\ln I}$ after the airplane landed is only small (with a maximum of $1.4 \cdot 10^{-4}$ compared to a $\overrightarrow{\sigma^2_{\ln I}}$ of $6.4 \cdot 10^{-5}$), and only a few points show an elevated $\sigma^2_{\ln I}$ (6, but not consecutive). Thereby, the detection criteria stated in Section 6.3.1 are not met. It is possible that the wake vortex had already decayed before reaching the scintillometer path, or that it was transported away from the scintillometer path (with a wind direction of 223°at the time). Figure **??** is a typical example of the detectability of wake vortices during the night. In the end, we can conclude that for these night time conditions the scintillometer is clearly able to indicate when a wake vortex is present.

Figure **??** shows $\sigma^2_{\ln I}$ for similar wind conditions as Fig **??** (not shown here, but $220° \leq \mathrm{WD} \leq 250°$ and $-5\ \mathrm{m\ s^{-1}} \leq \mathrm{U}_\perp \leq -2.5\ \mathrm{m\ s^{-1}}$), but during day-time conditions. For these conditions, the influence of the wake vortices on the scintillation signal is not visible. Apparently, during the day the scintillometer signal is dominated by the background atmospheric turbulence, making it impossible to detect wake vortices from $\sigma^2_{\ln I}$. To make sure that there are no false detections of wake vortices due to the background atmospheric turbulence the criterion of $\overline{\sigma^2_{\ln I}} < 2 \cdot 10^{-4}$ is included in the detection algorithm (see Section 6.3.1). Implicitly this criterion is a filter on stability; the lower $\overline{\sigma^2_{\ln I}}$ the more stable the atmosphere.

Before looking into the amount of wake vortices detected by the scintillometer, we first investigate the wind direction and speed under which landings and take offs occurred (Fig. **??**a and b). Note that in this figure only the airplanes for which the wake vortices can potentially be detected (using the criteria stated in Section 6.3.1) are taken into account. There is a clear difference in wind directions under which landings and take offs occur, since the airplanes need to keep their nose into the wind. Landings mainly occur during wind directions of 180–270°, while take offs

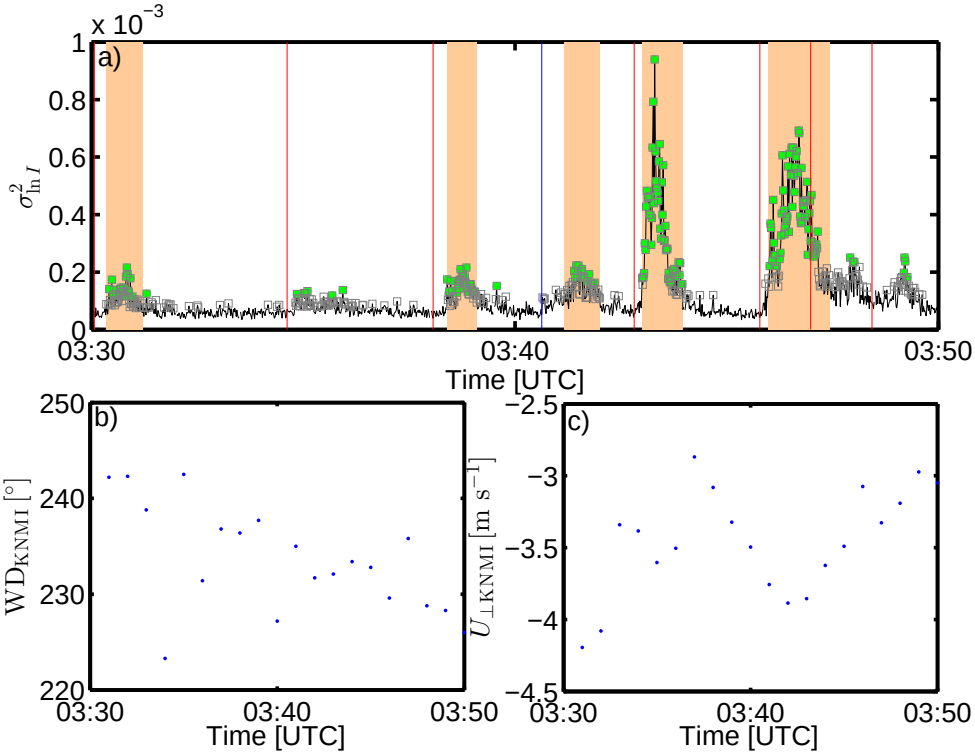

Figure 6.3: (a) Time series of $\sigma^2_{\ln I}$ measured by the scintillometer on DOY 186 in between 3:30 and 3:50 UTC, the solid lines indicate when an airplane was landing (blue for an airplane with wake turbulence category medium, and red for an airplane with wake turbulence category heavy). The green dots indicate when $\sigma^2_{\ln I}$ is high to indicate a wake-vortex, the grey squares indicate till when a wake vortex is to be taken into account. The orange shaded areas indicate the time period over which the algorithm specified in Section 6.3.1 finds a wake vortex. (b) Wind direction and (c) crosswind measured by KNMI over the same time period (1 min average).

occur during wind directions of 350–60°. The wind speed is in general greater for airplanes landing (typically 6-7 m s^{-1}) than taking off (typically 4-5 m s^{-1}). Given the setup in this experiment (see Section 6.4.1), the landings should be more easily detectable, since the wake vortices are blown towards the scintillometer path.

Figures **??**c and d show the wind roses of the wake votices that are detected by the scintillometer. The wake vortices caused by landing airplanes are detected for wind directions of 220–230°, while the wake vortices created by airplanes under wind directions of 180–220° are not detected. This implies that the wake vortices

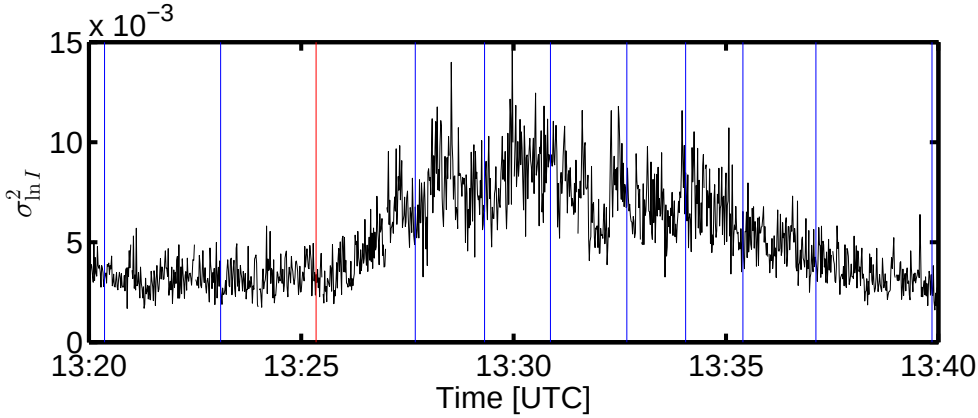

Figure 6.4: Time series of $\sigma^2_{\ln I}$ measured by the scintillometer on DOY 184 in between 13:20 and 13:40 UTC, the solid lines indicate when an airplane was landing (blue for an airplane with wake turbulence category medium, and red for an airplane with wake turbulence category heavy).

are indeed transported by the wind. For airplanes taking off the wake vortices are mainly detected when the wind speed is relatively weak ($\leq$ 4 m s^{-1}). The wake vortices created by airplanes taking off under the influence of strong wind speed would be transported from the scintillometer path. There are also some (in total 39) wake vortices detected when there was no airplane landing or taking off the previous 3.5 min, which we refer to as false detections. The wind rose of these false detections is plotted in Fig. **??**e. The false detections seem to occur for random wind directions and wind speeds.

Table 6.1 lists the amount of wake vortices detected by the scintillometer, as well as the amount of airplanes that produce wake vortices that are potentially detectable using the criteria stated in Section 6.3.1. Note that we do not expect that the wake vortices of all airplanes are detected, since some wake vortices can decay before reaching the scintillometer path or due to transport by wind do not reach the scintillometer path at all. From the in total 386 wake vortices that were potentially detectable 139 wake vortices were detected. There were also 39 false detections, which probably occur due to the influence of background atmospheric turbulence on the scintillometer signal, also insects or dust can influence the scintillometer signal and be misinterpreted as wake vortices. As expected, the scintillometer more easily detects wake vortices for airplanes landing than taking off (63% compared to 15%), which is likely caused by the wind directions under which planes land and take off (Fig. **??**). The influence of

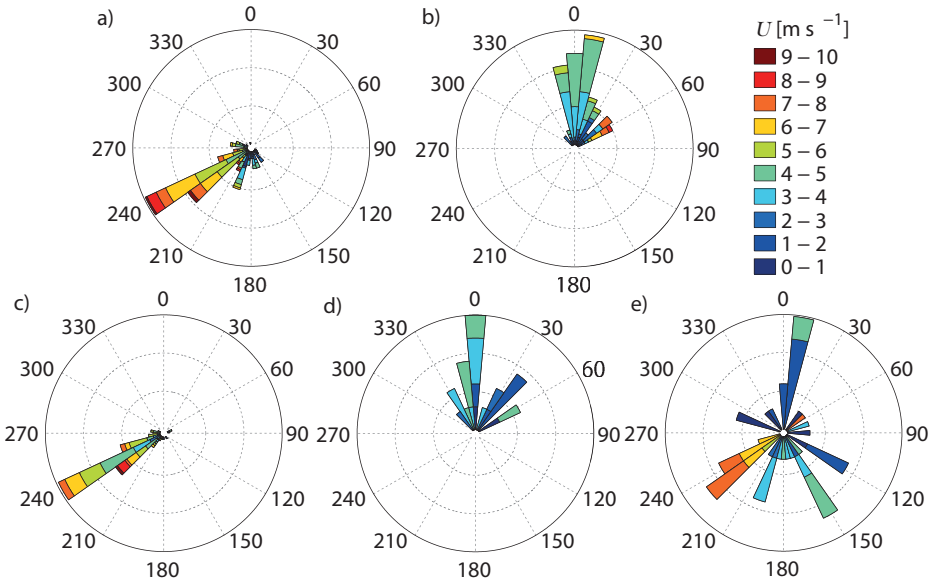

Figure 6.5: Wind roses of airplanes (a) landing and (b) taking off in conditions where the wake vortices are detectable by the scintillometer, colored with the horizontal wind speed. Wind roses of the detected wake vortices for airplanes (c) landing, (d) taking off, and (e) false detections, colored with the horizontal wind speed.

the transport by the wind of wake vortices is also apparent from the higher amount of wake vortices that are detected when $\overline{U_\perp} < 0$ m s^{-1} than when $\overline{U_\perp} > 0$ m s^{-1} (as percentage of the total detectable 50% compared to 12%). Therefore, in order to increase the amount of wake vortices that are detected for $\overline{U_\perp} > 0$ m s^{-1} and for airplanes taking off a scintillometer also would have to be placed at other side of the runway (in this case west).

In Table 6.1 a difference is visible between the percentage of wake vortices detected for airplanes with a medium and heavy wake turbulence category. Both for airplanes landing and taking off there is a clearly higher detectability of the wake vorticies created by an airplane with wake turbulence category of heavy (76% and 27%) than for a wake turbulence category of medium (38% and 14%). This seems to imply that wake vortices created by an airplane with a wake turbulence category of medium decay faster than those created by an airplane with a wake turbulence category of heavy.

In order to investigate the capability of the scintillometer to give a measure of the strength of the wake vortices, Fig. **??** shows the occurrence of different $\mathrm{WV}_{\mathrm{Intensity}}$

Table 6.1: Amount of airplanes of which potentially the wake vortices could be detected by the scintillometer, together with the amount of wake vortices (landing, take off, and false) detected by the scintillometer giving the corresponding wake turbulence category of the airplane.

		Landing			Take off			False
	$U_\perp$	Medium	Heavy	**Total**	Medium	Heavy	**Total**	
Airplanes	> 0	35	6	**41**	92	12	**104**	
Airplanes	< 0	161	52	**213**	25	3	**28**	
Detected	> 0	4	0	**4**	9	4	**13**	20
Detected	< 0	71	44	**115**	7	0	**7**	19

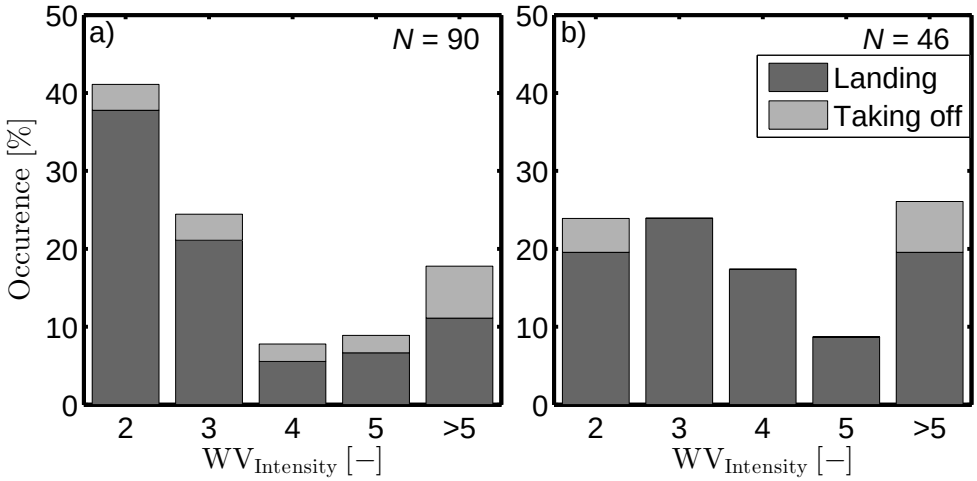

Figure 6.6: Histogram of the occurrence (in %) of wake-vortex intensities for airplanes with a wake turbulence category of (a) medium, and (b) heavy, where 2 on the x-axis stands for a $\mathrm{WV_{Intensity}}$ in between 1 and 2, 3 for a $\mathrm{WV_{Intensity}}$ in between 2 and 3, and so on.

values for airplanes with wake-vortex class medium (Fig. **??**a), and heavy (Fig. **??**b). For airplanes with a wake turbulence category of medium $\mathrm{WV_{Intensity}}$ in between 1 and 2 occurs most often (41 %), while for a wake turbulence category of heavy a $\mathrm{WV_{Intensity}}$ greater than 5 occurs most often (26 %). The strength of the wake vortices were not influenced by the value of $U_\perp$ (not shown here), nor by whether an airplane was landing or taking off. From Fig. **??** we can conclude that the scintillometer indeed measures stronger wake vortices when the wake vortex is created by an airplane with a wake turbulence category of heavy.

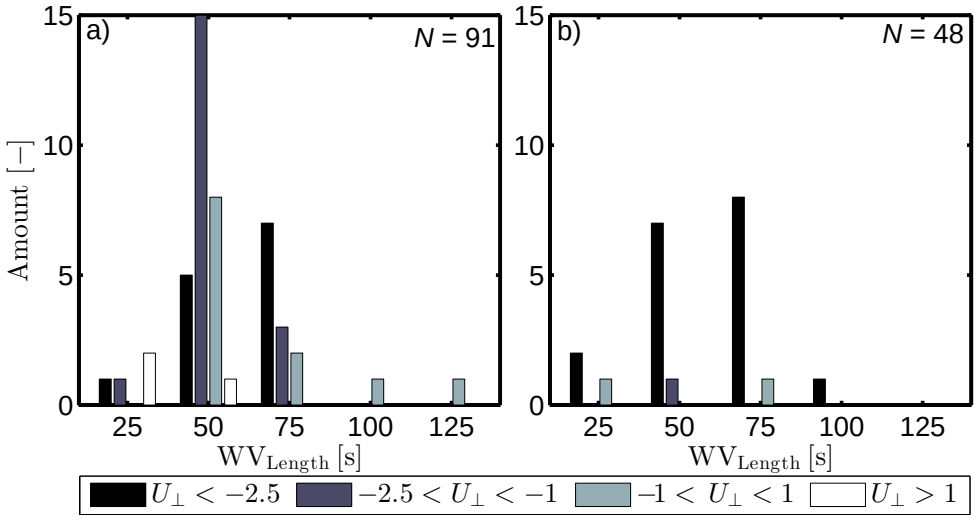

Figure 6.7: Histograms of the amount of wake-vortex length for airplanes with wake turbulence category (a) medium, and (b) heavy, where 25 on the x-axis stands for a $\mathrm{WV_{Length}}$ in between 0 and 25 s, 50 for a $\mathrm{WV_{Length}}$ in between 25 and 50 s, and so on. The histograms are color coded with $U_\perp$.

Besides the strength of a wake vortex the scintillometer can also give a measure of the size of a wake vortex, which is expressed as the time the wake vortex is present in the scintillometer signal (see Fig. **??**). There is no clear difference visible for wake vortices created by airplanes with a wake turbulence category of medium and heavy. For both categories the wake vortices are mostly present in the scintillometer signals in between 25 and 75 s. However, some wake vortices are present for up to 125 s in the scintillometer signal. Figure **??**a indicates that the wake vortices are longer present in the scintillometer signal when $|U_\perp|$ is weak (< 1 m s^{-1}).

Figure **??** depicts the separation time between an airplane landing or taking off and the scintillometer detecting the corresponding wake vortex for different $U_\perp$-values. This figure confirms that wake vortices leave the runway with different time scales. Most wake vortices are detected in between 0 to 80 s after the airplane landed or took off. The figure again indicates that the wake vortices are transported by the wind, the more negative $U_\perp$ (darker colors in Fig. **??**), the earlier the wake vortices are detected. The airplanes with a wake turbulence category of heavy are in general very fast detected with often (25 %) only 0 to 40 s in between the airplane landing or taking off and the detection. For airplanes with a wake turbulence category of medium times between 40 and 80 s occur most often (25 %). From Figs. **??** and **??**

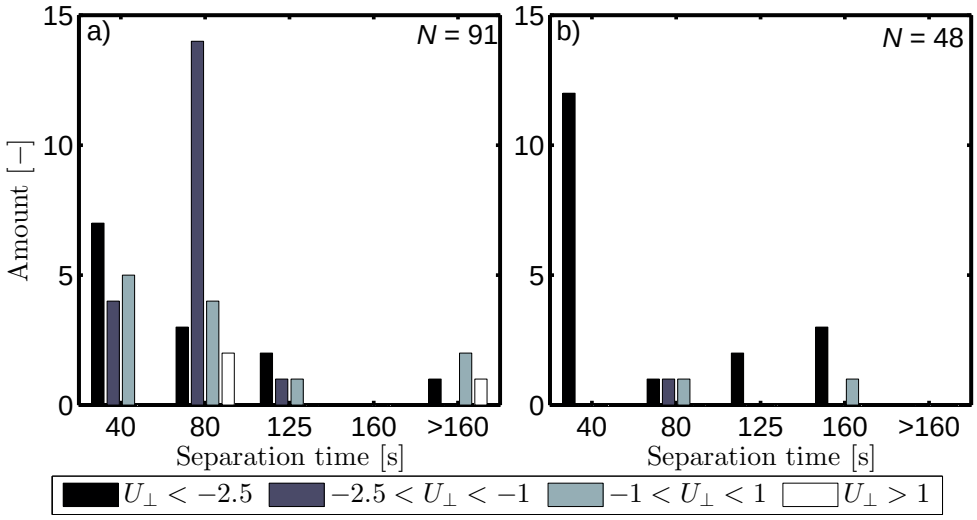

Figure 6.8: Histograms of the time between an airplane landing or taking off and the scintillometer picking up the wake vortex of the airplane with a wake turbulence category of (a) medium and (b) heavy, where 40 on the x-axis stands for a separation time in between 0 and 40 s, 80 for a separation time in between 40 and 80 s, and so on. The histograms are color coded with $U_\perp$.

we can conclude that taking a fixed separation distance between airplanes landing and taking off is in reality not necessary and unnecessarily limits the airport capacity. Thus, a scintillometer can detect when a wake vortex has left the runway, which can increase the airports capacity.

6.5.2 Crosswind

The crosswind was measured by the scintillometer over 3-s time windows, while KNMI data were saved over every 12 s (see Section 6.4.1). Note that the clock of the scintillometer and KNMI measurements were not synchronized. Furthermore, the measurement location and height of the scintillometer and KNMI wind data are not the same (see Section 6.4.1). Therefore, the comparison between $U_\perp$ measured by the scintillometer (transposed to a measurement height of 10 m, see Section 6.4.2) and KNMI is done over 1 min averages. This comparison is plotted in Fig. **??**a. The agreement between the two measurement devices is very satisfactory with a linear regression slope of 0.89 and a low amount of scatter ($R^2 = 0.90$), leading to an RMSE of 0.89 m s^{-1}. Concluding, the scintillometer is capable of obtaining $U_\perp$ correctly

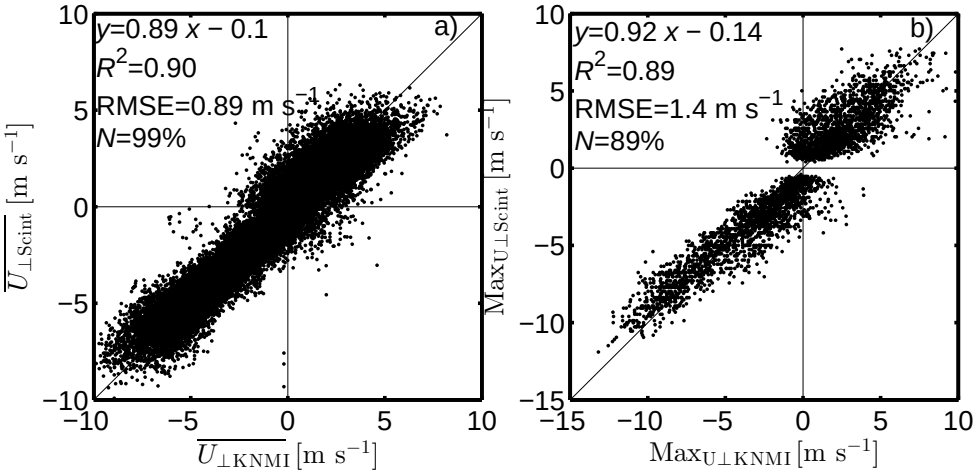

Figure 6.9: (a) Scatterplot of the 10-min average of $U_\perp$ measured by the scintillometer ($\overline{U_{\perp\mathrm{Scint}}}$) and KNMI ($\overline{U_{\perp\mathrm{KNMI}}}$). (b) Scatterplot of the maximum $U_\perp$ measured by the scintillometer ($\overline{\mathrm{Max}_{U\perp\mathrm{Scint}}}$) and KNMI ($\overline{\mathrm{Max}_{U\perp\mathrm{KNMI}}}$). For both plots the corresponding regression statistics are plotted on the left-hand side and the black line indicates the one-to-one line.

near an airport runway over a 3-s time window.

For aviation an important parameter for the wind is the maximum $U_\perp$ value over the last 10 min ($\mathrm{Max}_{U\perp}$). The results of $\mathrm{Max}_{U\perp}$ are plotted in Fig. **??**b. There is again a good correlation between the scintillometer $U_\perp$-measurements and KNMI $U_\perp$-measurements, albeit with more scatter between the two ($R^2 = 0.89$). However, this higher scatter is to be expected since the maximum corresponds to a 3 s $U_\perp$-value, which given the different measurements location and height can differ.

6.5.3 Visibility

Before going into detail about the calibration of I_T, we first have a look at Fig. **??**a, which shows the normalized scintillation signal against MOR measured by the visibility sensor. From this figure it is apparent that there is a sharp drop in $\overline{I_{\mathrm{R}*}}$ when MOR is below 10 km. However, for the early morning hours (in between 5:00 and 7:00 UTC), there are some cases where the visibility is above 10 km and $\overline{I_{\mathrm{R}*}}$ is below $\frac{2}{3}$ of $I_{\mathrm{R,max}}$ (10 000). These cases are probably caused by water droplets on the apertures of the scintillometer due to dew. Therefore, cases in between 5:00 and 7:00 UTC where $\overline{I_{\mathrm{R}*}} < \frac{2}{3} I_{\mathrm{R,max}}$ and MOR> 10 km were excluded for the rest of the

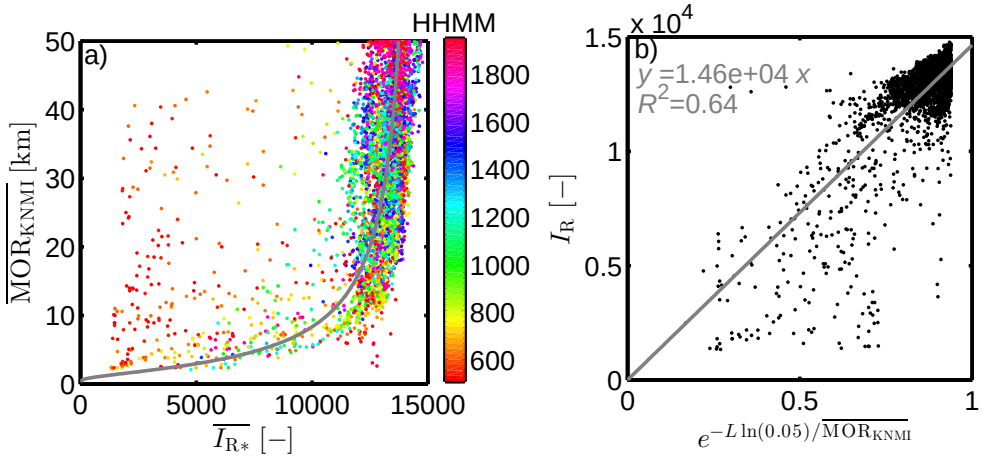

Figure 6.10: (a) Plot of MOR measured by the visibility sensor ($\mathrm{MOR_{KNMI}}$) against $\overline{I_{\mathrm{R}*}}$ color coded with HHMM. The grey line indicates the values of MOR obtained from $\overline{I_{\mathrm{R}*}}$ when using Eq. 6.5 and I_{T} from the right figure. (b) Plot of $\overline{I_{\mathrm{R}}}$ against $e^{-L\ln(0.05)/\mathrm{MOR}}$, with the regression equation and R^2 with a fit through the origin given in grey.

visibility analysis.

The calibration of I_{T} is done by means of Fig. **??**b, where $\overline{I_{\mathrm{R}*}}$ is plotted against $e^{-L\ln(0.05)/\mathrm{MOR}}$. According to Eqs. 6.2 and 6.4, these two quantities should have a linear relation with one another, where the regression slope between these two gives I_{T}. There is indeed a linear relationship through the origin visible in Fig. **??**b. However, the scatter is reasonably large with an R^2-value of 0.64. This scatter can be caused by the different measurement locations of the scintillometer and the visibility sensor (see Fig. **??**). The regression slope of $1.46 \cdot 10^4$ given in Fig. **??**b is in fact the value of I_{T}. In Fig. **??**a the grey line indicates MOR given the value of $\overline{I_{\mathrm{R}*}}$ using this value of I_{T} after applying Eq. 6.5 ($\overline{\mathrm{MOR_{Scint}}}$). Given the measurements of $\overline{\mathrm{MOR_{KNMI}}}$ there is indeed a good correspondence with $\overline{\mathrm{MOR_{Scint}}}$ for the different values of $\overline{I_{\mathrm{R}*}}$.

Figure **??** shows MOR measured by the visibility sensor (KNMI) and scintillometer (Scint) over the measurement period. Form Fig. **??**a it is apparent that there is a lot of scatter between $\overline{\mathrm{MOR_{Scint}}}$ and $\overline{\mathrm{MOR_{KNMI}}}$ for values of $\overline{\mathrm{MOR_{Scint}}}$ above 15 km. Therefore, Fig. **??**b shows values of $\overline{\mathrm{MOR_{Scint}}}$ in between 0 and 15 km. Also for these lower values of MOR there is scatter between that measured by KNMI and scintillometer ($R^2 = 0.39$). Besides the scatter also the fit of $\overline{\mathrm{MOR_{Scint}}}$ with $\overline{\mathrm{MOR_{KNMI}}}$ is

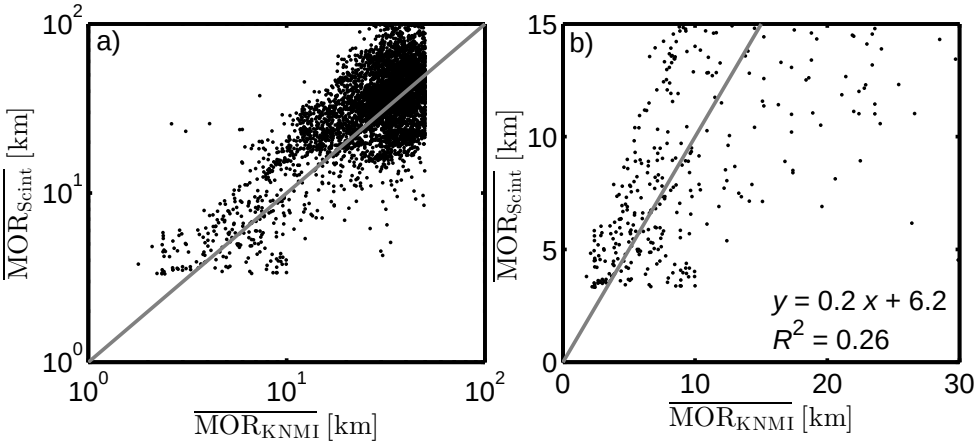

Figure 6.11: MOR measured by the visibility sensor ($\overline{\mathrm{MOR}_{\mathrm{KNMI}}}$) and the scintillometer ($\overline{\mathrm{MOR}_{\mathrm{Scint}}}$) for (a) all values on logarithmic axes, and (b) zoomed into a $\overline{\mathrm{MOR}_{\mathrm{Scint}}}$ of 0 to 15 km on normal scale including the regression statistics. The grey lines indicate the one-to-one line.

poor with a regression slope of 0.25. Some of the scatter can – as already discussed earlier – be caused by the different measurement location of the two devices. However, it seems that the scintillometer has problems to quantify MOR correctly.

6.6 Conclusions

In this study we investigated the use of a scintillometer installed alongside a runway at Schiphol airport to detect wake vortices, crosswind, and visibility. We conclude that during the night, when the amount of turbulence in the atmosphere is low, a scintillometer is able to detect the presence of a wake vortex in its path, by an increase in $\sigma^2_{\ln I}$. However, during the day the scintillation signal, and thereby $\sigma^2_{\ln I}$, is dominated by the background atmospheric turbulence making it impossible to detect wake vortices from the scintillation signal. Besides detecting when a wake vortex is present, we also developed an algorithm to determine the strength of a wake vortex. The algorithm worked satisfactory, since airplanes with a heavy wake turbulence category more often produced high values of $\mathrm{WV}_{\mathrm{Intensity}}$ (> 5). For the scintillometer setup used in this study the wake vortices created by landings are more often detected than those created by take offs, probably due to the different wind regime during landing and take off. In order to increase the detectability of wake vortices created

by take offs another scintillometer needs to be setup at the other side of the runway (in this case at the west side). Further, the detectability can also be increased by placing the scintillometer as close by the runway as possible. There were 39 cases where the algorithm detected a wake vortex though no airplane landed or took off in the previous 3.5 min, which are probably caused by an increase of $\sigma^2_{\ln I}$ related to the background atmospheric turbulence.

A scintillometer is able to obtain correct values of the crosswind also near an airport runway over a 3-s time-window. However, in order to achieve correct crosswind estimations a filter on outliers had to be applied. Although this filter was applied it is still possible to obtain the maximum crosswind over the last 10 min, which is an important quantity for aviation.

It is difficult to obtain the exact value of the visibility from the signal intensity of the scintillometer. However, albeit with some scatter, the scintillometer is able to obtain the visibility when it is below 10 km. Different issues had to be corrected in order to achieve these results. First, alignment issues can result in a decrease in the scintillometer signal, which can be misinterpreted as low visibility conditions. Therefore, in this study the signal was adjusted for alignment issues. Second, dew on the apertures of the scintillometer can result in a lowering of the scintillometer signal. Thus in order to measure visibility it is recommendable to use scintillometers that heat the aperture, to minimize the influence of dew on the scintillometer signal.

Acknowledgments

The authors would like to thank Kees van den Dries and Jan-Willem Schoonderwoerd for their help in the field, Ben Wichers Schreur for supplying KNMI data, and Evert Westerveld for supplying the wake turbulence category data. Further the authors also thank Marco Ponsen, Jan-Otto Haanstra, Peter van den Brink, Martin Dikker, Jan Sondij, Henk Klein Baltink, Paul van Es, Jan Meijer, Frits van Peppel, Rob Poelsma, and Jan Elbers for making it possible to measure at Schiphol airport. Daniëlle van Dinther and Oscar Hartogensis were supported by the Knowledge for Climate project Theme 6 entitled “High Quality Climate Projections” (KVK-HS2).

6. RUNWAY WAKE VORTEX, CROSSWIND, AND VISIBILITY DETECTION WITH A SCINTILLOMETER AT SCHIPHOL AIRPORT

7

Summary

This chapter gives an overview of the main findings of this thesis. The findings are discussed on the basis of the research questions stated in Section 1.3.

This thesis outlines how a scintillometer can measure the so-called crosswind ($U_\perp$), where $U_\perp$ is defined as the wind component perpendicular to a path. Crosswind measurements are among other applications necessary at airports, since strong $U_\perp$ on runways introduces a safety risk for airplanes landing and taking off. A scintillometer consists of a transmitter and a receiver typically spaced a few hundred meters to a few kilometres apart. The transmitter emits light, which is refracted by the turbulent eddy field in the atmosphere. The receiver measures intensity fluctuations, which can be related to a path-averaged value of $U_\perp$ ($\overline{U_\perp}$).

The first research question of this thesis was:

Question 1: Are the theoretical models by Lawrence *et al.* (1972) and Clifford (1971) suitable to calibrate the crosswind measurements of a scintillometer, instead of experimental calibration?

In Chapter 3 of this thesis we tested if the theoretical model for the scintillation power spectrum ($S_{11}(f)$) of Clifford (1971) was able to calibrate the constants describing the relation between $\overline{U_\perp}$ and the corner frequency and maximum frequency. The spectrally derived $\overline{U_\perp}$ values compared well with sonic anemometer estimates, indicating that the model of Clifford (1971) can be used to obtain $\overline{U_\perp}$ from $S_{11}(f)$, making an expensive experimental calibration redundant.

In Chapter 4 of this thesis we tested if the theoretical model for the time-lagged correlation function of a dual-aperture scintillometer ($r_{12}(\tau)$) of Lawrence *et al.*

(1972) was able to calibrate the constants describing the relation between $\overline{U_\perp}$ and the peak in $r_{12}(\tau)$ (peak method), the intersection between $r_{12}(\tau)$ and the time-lagged variance function (Briggs method), and the slope of $r_{12}(\tau)$ at zero time-lag (zero-slope method). The two benefits of using $r_{12}(\tau)$ instead of $S_{11}(f)$ to derive $\overline{U_\perp}$ are that from $r_{12}(\tau)$ also the sign can be obtained and $\overline{U_\perp}$ can be obtained over a relatively short time span ($\sim$ 10 s). The $\overline{U_\perp}$-values obtained from the scintillometer were again compared to sonic anemometer measurements. Results showed that the model of Lawrence *et al.* (1972) was able to calibrate the constant for the three methods. However, for the Briggs methods the "constant" (C_B) turned out not to be constant, but to increase with higher $\overline{U_\perp}$-values ($>$ 5 m s^{-1}). We conclude that assuming a constant C_B would result in errors for these high values of $\overline{U_\perp}$.

The second research question answered in this thesis was:

Question 2: Can the shape of the theoretical models by Lawrence *et al.* (1972) and Clifford (1971) be used to obtain the crosswind?

Two new methods were introduced in this thesis to explore this issue; the cumulative spectrum method (in Chapter 3) and the lookup table method (in Chapter 4). The cumulative spectrum uses five points in the cumulative spectrum to obtain $\overline{U_\perp}$. From the methods relying on scintillation spectra to derive $\overline{U_\perp}$ this method obtained the best results.

The lookup table method obtains $\overline{U_\perp}$ by comparing $r_{12}(\tau)$ of measurements to the theoretical model of $r_{12}(\tau)$. This method obtained the best result of $\overline{U_\perp}$ from $r_{12}(\tau)$ for $\overline{U_\perp} > 2$ m s^{-1}.

The third research question answered in this thesis was:

Question 3: How are the crosswind measurements of a scintillometer influenced by variable crosswind values along the scintillometer path?

In appendix 3A the hypothetical influence of a slant path on the scintillometer $\overline{U_\perp}$-values calculated from $S_{11}(f)$ were investigated. On a slant path $U_\perp$ will change along the scintillometer path due to different measurement heights according to the wind profile. Even for an extreme slant path (from 2 to 100 m) the maximum error in $\overline{U_\perp}$ was 8 %.

In Chapter 4 we investigated how $r_{12}(\tau)$ changed as a result of a hypothetical $U_\perp$-field where $U_\perp$ was different for two halves of the path. The resulting $r_{12}(\tau)$ was a combination of $r_{12}(\tau)$ of the two different crosswinds. Therefore, the measured value of $\overline{U_\perp}$ is probably affected by a variable $U_\perp$-field.

In Chapter 5 we investigated to what extend the $\overline{U_\perp}$-measurements were affected by a variable $U_\perp$-field along the scintillometer path. In this chapter scintillometer measurements where carried out above the urban environment of Helsinki, Finland. In this environment $U_\perp$ is expected to vary over the scintillometer path. The scintillometer measurements are compared to Doppler lidar measurements, which allows acquisition of a path-resolved $U_\perp$ ($U_\perp(x)$, where x is the position along the path). Two methods were applied to obtain $\overline{U_\perp}$ from the scintillometer signal: the cumulative spectrum method, and the lookup table method. Both methods compared reasonably well with the Doppler lidar measurements, especially considering the challenging urban environment in which the measurements were taken. This good comparison indicates that both measurement technologies are able to obtain $\overline{U_\perp}$ over a complex urban environment. The in detail investigation of four cases indicated that the cumulative spectrum method is less susceptible to a variable $U_\perp(x)$ than the lookup table method. However, the lookup table method can be adjusted to improve its capabilities to obtain $\overline{U_\perp}$ for conditions where $U_\perp(x)$ is variable.

The last research question answered in this thesis was:

Question 4: To what extent can a scintillometer detect wake vortices, crosswind, and visibility near an airport runway?

This question was answered in Chapter 6 of this thesis using data collected near a runway at Schiphol airport (Amsterdam, the Netherlands). The scintillometer measurements were compared to wind measurements and visibility measurements made at the airport. The results showed that, after applying an outlier filter, a scintillometer was also able to obtain $\overline{U_\perp}$ using the lookup table method near airport runways also over the short averaging time needed in aviation (3 s). Although an outlier filter was applied, the scintillometer was still able to correctly obtain the maximum $\overline{U_\perp}$ over 10 min.

The scintillometer signal drops off very sharply as a result of a decrease in visibility, making it hard to quantify the visibility with the scintillometer. We conclude that a scintillometer is able to identify time periods where the visibility is below 10 km, albeit with a high amount of scatter.

Results showed that during the night a scintillometer is able to detect wake vortices, because of the extra fluctuations in the scintillation signal that the vortices introduce. The amount of variance in the scintillometer signal even states information about the strength of the wake vortex. Finally, during the day the scintillometer signal is dominated by the background atmospheric turbulence, making it very difficult to detect wake vortices with a scintillometer under these conditions.

8

General discussion & Outlook

This chapter discusses the main findings of this thesis on the basis of the research questions stated in Section 1.3 and put them in a broader perspective. Further, an outlook on scintillometer crosswind measurements and its applicability at airports is given.

8.1 General discussion

Question 1: Are the theoretical models by Lawrence *et al.* (1972) and Clifford (1971) suitable to calibrate the crosswind measurements of a scintillometer, instead of experimental calibration?

Chapters 3 and 4 showed that the model of Lawrence *et al.* (1972) and Clifford (1971) can be used to calibrate $\overline{U_\perp}$ measurements of the scintillometer. However, for the Briggs method the "constant" is in fact not constant, but changes for higher crosswind ($U_\perp$) values.

In Chapters 3 and 4 the path-averaged crosswind ($\overline{U_\perp}$) obtained by the scintillometer was compared to point measurements obtained by a sonic anemometer. However, the anemometer was not located in the center of the scintillometer path, but around 300 m away. In order to validate the $U_\perp$-measurements of the scintillometer with the sonic anemometer the values were averaged to 10 min. Ideally, a path-averaged value of $U_\perp$ should be measured using an array of sonic anemometers along the scintillometer path (or cup anemometers and wind vanes, as done by Poggio *et al.* (2000)). This would allow a validation of $\overline{U_\perp}$ over a shorter time window. Because of the limitations in the experimental setup described in Chapters 3 and 4 only the 10 min average and 10 min standard deviation of $U_\perp$ could be validated. An array of sonic

anemometers would enable us to identify better how well the scintillometer is able to obtain $\overline{U_\perp}$ over short time windows. As such, it is recommended to use an array of sonic anemometers to validate the $\overline{U_\perp}$ values in future studies.

Question 2: Can the shape of the theoretical models by Lawrence *et al.* (1972) and Clifford (1971) be used to obtain the crosswind?

The cumulative spectrum method (using the scintillation spectral model of Clifford (1971)) and the look-up table method (using the time-lagged correlation fuction model of Lawrence *et al.* (1972)) were developed in Chapters 3 and 4 of this thesis. Both methods performed adequately, and compared well with $U_\perp$-measurements obtained from the sonic anemometer. However, for the cumulative spectrum method a filter was necessary on data where the spectral maximum was lower than 0.1 Hz or higher than 90 Hz, resulting in a data-availability of 75 %. The look-up table method proved to be the best method to obtain $\overline{U_\perp}$ from the time-lagged correlation function in conditions were $U_\perp$ is strong ($U_\perp \geq 2$ ms^{-1}). For the application at airports these strong $U_\perp$-conditions are the practically relevant cases.

Question 3: How are the crosswind measurements of a scintillometer influenced by variable crosswind values along the scintillometer path?

We answered this question first by using the theoretical models by Lawrence *et al.* (1972) and Clifford (1971). Appendix 3A showed a low error (maximum error of an extreme case of 8%) for $\overline{U_\perp}$ obtained from the scintillation spectra ($S_{11}(f)$) when a slant scintillometer path was used, where $U_\perp$ changes due to the increase of wind speed with height. Chapter 4 showed that the shape of the time-lagged correlation function ($r_{12}(\tau)$) is influenced by a variable $U_\perp$ along the path for an extreme case (different $U_\perp$ on two halves of the scintillometer path). However, it is questionable how well the theoretical models represent $S_{11}(f)$ and $r_{12}(\tau)$ under variable $U_\perp$ conditions.

In Chapter 5, the Doppler lidar was measuring path-resolved $U_\perp$-values, which were used to calculate the theoretical cumulative spectrum ($\mathrm{S_{cum}}$) and $r_{12}(\tau)$ given variable $U_\perp$-conditions along the path for four selected case studies. The values and shape of $\mathrm{S_{cum}}$ and $r_{12}(\tau)$ compared well to the ones measured by the scintillometer. Also a good comparison was found between $\overline{U_\perp}$ measured with the scintillometer and the Doppler lidar, also under variable wind conditions. However, in order to achieve these results we applied a strict filter on wind direction, due to the fact that two beams of the Doppler lidar were far apart (22°). In order to test the performance of

the scintillometer and Doppler lidar for all wind conditions above an urban environment, the two Doppler lidar beams have to be closer together (for example 10°).

Question 4: To what extent can a scintillometer detect wake vortices, crosswind, and visibility near an airport runway?

In Chapter 6 wake vortices were determined from the variance in the scintillometer signal during the night. However, no other measurement devices were measuring wake vortices alongside the scintillometer. Therefore, the detectability of the wake vortices was determined by the known wake vortex classes of the airplanes landing and taking off. In multiple studies (among other Harris *et al.*, 2002; Gerz *et al.*, 2005; Holzäpfel & Steen, 2007) Doppler lidars have been proven capable of measuring wake vortices along the gliding path of airplanes. Using a Doppler lidar alongside the scintillometer would allow for a better comparison of the wake vortex intensity measured by the scintillometer. Godwin *et al.* (2012) noted that a Doppler lidar has problems to retrieve the wind field correctly close to the ground. Alternatively, close to the ground, an array of sonic anemometers could measure the wake vortices (Hallock & Osgood, 2003) and thereby validate the scintillometer measurements of the wake vortices.

The results in Chapter 6 indicate that in order to detect when wake vortices leave the runway two scintillometer should be placed on both sides of the runway. Further, the scintillometers should be setup as close to the runway as possible, since wake vortices can decay while being transported away from the runway.

Besides measuring wake vortices, there are also promising studies trying to model the decay and transport of wake vortices. Shen *et al.* (1999) concluded from their model results that ambient turbulence significantly influences the vortex decay. Scintillometers measure turbulence, and therefore the link between wake vortex decay and turbulence can be investigated using scintillometer data.

The crosswind measurements of the scintillometer and that of wind vane and cup anemometer showed a good comparison for 1-min averages. In order to compare the 3 s data directly, an array of wind vanes and cup anemometer (or alternatively sonic anemometers) need to be setup along the scintillometer path. Further, the scintillometer and wind vane and cup anemometers need to have the same measurement heights.

The scintillometer was able to obtain a value of the visibility below 10 km, which are the practically relevant cases at airports. However, the scintillometer did show a high amount of scatter when compared to the visibility sensor. This scatter could be caused by the different measurements locations of the scintillometer and the visibility

sensor. In order to compare the two devices more thoroughly a visibility sensor would need to be placed in the middle of the scintillometer path. Further, to exclude the influence of dew on the scintillometer signal it is advisable to use a scintillometer with heated aperture windows.

8.2 Outlook

In general scintillometers are used to measure a path-averaged value of the surface fluxes. These surface fluxes are calculated from the structure parameter of the refractive index (C_{n^2}), which are obtained from the variance of the log intensity fluctuations of the scintillometer. However, Van Kesteren *et al.* (2014) showed that for weak $|U_\perp|$-values (≤ 1 m s^{-1}) there is a difference between C_{n^2} of two large aperture scintillometer manufacturers (Wageningen LAS and Scintec BLS) measuring simultaneously alongside each other. They attributed this to a different high-pass frequency filter applied by the scintillometers (0.1 Hz for the Wageningen LAS and 0.03 Hz for the Scintec BLS). A high-pass filter is applied to remove fluctuations in the scintillometer signal due to absorption. Nieveen *et al.* (1998) showed that the absorption fluctuations occur at lower frequencies than those associated with refraction. However, for low $|U_\perp|$-values the refractive index fluctuations still contribute to the scintillation signal for low frequencies. Removing these fluctuations with a high-pass filter, thereby artificially reduces C_{n^2} (Solignac *et al.*, 2012). Crosswind measurements by a scintillometer can help to identify time periods where C_{n^2} of the scintillometer is underestimated due to the high-pass filter applied. Note that in order to do so only $\overline{U_\perp}$ estimates from $r_{12}(\tau)$ should be used, since a high-pass frequency filter was also applied in order to obtain $\overline{U_\perp}$ from $S_{11}(f)$. Besides identifying time periods where C_{n^2} is underestimated, $U_\perp$ scintillometer measurement can prevent an underestimation of C_{n^2} by using a dynamical high-pass frequency filter according to the value of $|U_\perp|$. In doing so, for weak values of $|U_\perp|$ (≤ 1 m s^{-1}), absorption fluctuations can also cause fluctuations in the scintillometer signal and be wrongly attributed to refractive index fluctuations.

Apart from determining $\overline{U_\perp}$ from either $S_{11}(f)$ or $r_{12}(\tau)$ as done in Chapters 3 and 4, $\overline{U_\perp}$ can in theory also be obtained from the co-spectra of the two signals of a dual-aperture scintillometer ($S_{12}(f)$). The reasoning is the same as that of obtaining $\overline{U_\perp}$ from $S_{11}(f)$; the larger $\overline{U_\perp}$ the more the higher frequencies contribute to $S_{12}(f)$. In that way, $\overline{U_\perp}$ can be obtained from a characteristic point in $S_{12}(f)$ and its location along the frequency axis (see Fig. 8.1). There are different points that could be used to obtain $\overline{U_\perp}$ (e.g., peaks, valleys, and zero crossing). Although this is a new approach to obtain $\overline{U_\perp}$ in practice it is similar to obtaining $\overline{U_\perp}$ from $S_{11}(f)$. Therefore, obtaining

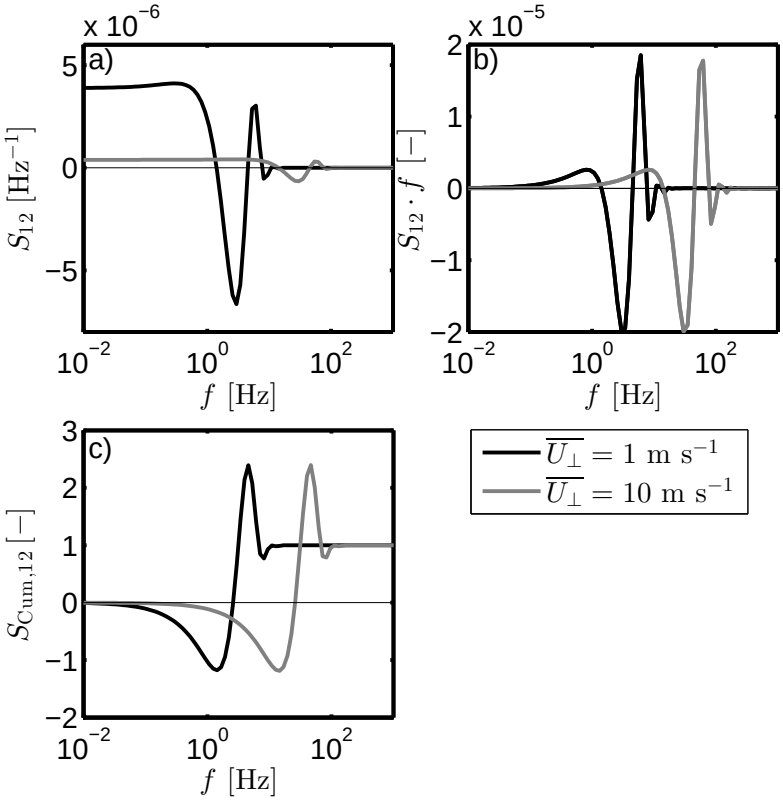

Figure 8.1: Theoretical power co-spectra of a dual aperture scintillometer signal for two different crosswind speeds visualized as (a) semi-log representation, (b) semi-log respresentation using $S_{12} \cdot f$, and (c) semi-log using the cumulative co-spectrum ($S_{\mathrm{Cum},12}$)

$\overline{U_\perp}$ from $S_{12}(f)$ has the same disadvantages as obtaining $\overline{U_\perp}$ from $S_{11}(f)$: the sign of $\overline{U_\perp}$ remains unknown and if $S_{12}(f)$ is determined with a fast Fourier transformation it needs to be obtained over a relatively long time window ($\sim$ 10 min). An advantage of determining $\overline{U_\perp}$ from $S_{12}(f)$ is that in theory $S_{12}(f)$ should not be affected by an eddy field blown into the scintillometer path by the longitudinal wind components, since the eddy field will not be correlated for the two scintillometer signals. In order to measure $S_{12}(f)$ a dual-aperture scintillometer is necessary, given the disadvantages given above methods relying on $r_{12}(\tau)$ to measure $\overline{U_\perp}$ are more preferable than relying on $S_{12}(f)$.

Rain causes extinction of the scintillometer signal (among others Wang & Clifford, 1975; Wang *et al.*, 1979, 1982; Nedvidek *et al.*, 1983; Uijlenhoet *et al.*, 2011), leading

to extra variance in the scintillometer signal which is not related to $\overline{U_\perp}$. According to Wang *et al.* (1982) rain induced scintillations occur at frequencies above 1 kHz. The scintillometer used in this study had a measurement frequency of 500 Hz, making it possible to determine $S_{11}(f)$ up to 250 Hz. In that way, the methods relying on $S_{11}(f)$ to obtain $\overline{U_\perp}$ should not be influenced by rain induced scintillations. However, in order to obtain $\overline{U_\perp}$ from $S_{11}(f)$ the scintillometer signal had to be at least above a threshold value. During rain events the scintillation signal can fall under the threshold, which would imply that $\overline{U_\perp}$ cannot be determined from $S_{11}(f)$ anymore. In order to obtain $\overline{U_\perp}$ from $r_{12}(\tau)$ no threshold of the scintillation signal is applied. The performance of the methods relying on $r_{12}(\tau)$ therefore depends on the correlation the rain induces in the two scintillation signals. If the two signals are uncorrelated affected by rainfall $r_{12}(\tau)$ will be lowered, but the shape will not change. If the two signals are correlated at the same time this will lead to a peak in $r_{12}(\tau)$ at zero time-lag resulting in a very strong estimate of $\overline{U_\perp}$. Applying an outlier filter on $\overline{U_\perp}$ as was discussed in Chapter 6 can make sure these large values of $\overline{U_\perp}$ are not taken into account.

For the application of scintillometer $\overline{U_\perp}$-measurements at airports the methods relying on $r_{12}(\tau)$ are more suitable than those relying on $S_{11}(f)$ to obtain $\overline{U_\perp}$. First, because of the fact that these methods are also able to determine the sign of $\overline{U_\perp}$. Second, because $\overline{U_\perp}$ can be obtained instantaneously from $r_{12}(\tau)$ over a short time window (3 s when an outlier filter is applied). Using wavelets $\overline{U_\perp}$ can also be obtained from $S_{11}(f)$ over a short time-window (1 s). However, a wavelet transformation can only be done afterwards, since it only yields values of $S_{11}(f)$ for low frequencies (< 0.1 Hz) for half the time over which the wavelet transformation is determined (see Fig. 2.6). Therefore, when determining $S_{11}(f)$ over a 5 min time window, the corresponding $S_{11}(f)$ which includes the low frequencies is representable for 2.5 min earlier. Note that at airports $\overline{U_\perp}$-measurements are necessary instantaneously. Third, methods relying on $r_{12}(\tau)$ are better capable in obtaining $\overline{U_\perp}$ in conditions where the scintillometer signal drops (e.g., due to rain or fog) than methods relying on $S_{11}(f)$. In this thesis the focus was not on the performance of the scintillometer during rain events, thus more research is necessary to evaluate the performance of the scintillometer in obtaining $\overline{U_\perp}$ in rain events.

When using the scintillometer operationally at airports to measure $\overline{U_\perp}$ alignment issues can occur. Over time the alignment of the scintillometer can change, which can cause the receiver to no longer receive the emitted light of the transmitter. Therefore, if a scintillometer will be used operationally the alignment of the scintillometer would need to be checked and if necessary be adjusted on a regular basis.

References

Andreas, E.L. (1989). Two-wavelength method of measuring path-averaged turbulent surface heat fluxes. *Journal of Atmospheric and Oceanic Technology*, **6**, 280–292. 61

Andreas, E.L. (2000). Obtaining Surface Momentum and Sensible Heat Fluxes from Crosswind Scintillometers. *Journal of Atmospheric and Oceanic Technology*, **17**, 3–16. 113

Baker, C.J., Jones, J., Lopez-Calleja, F. & Munday, J. (2004). Measurements of the cross wind forces on trains. *Journal of Wind Engineering and Industrial Aerodynamics*, **92**, 547–563. 32, 66

Beyrich, F., De Bruin, H.A.R., Meijninger, W.M.L., Schipper, J.W. & Lohse, H. (2002). Results from one-year continuous operation of a large aperture scintillometer over a heterogeneous land surface. *Boundary-Layer Meteorology*, **105**, 85–97. 14, 32, 47

Bornstein, R.D. & Johnson, D.S. (1977). Urban–rural wind velocity differences. *Atmospheric Environment*, **11**, 597–604. 96

Briggs, B.H., Phillips, G.J. & Shinn, D.H. (1950). The Analysis of Observations on Spaced Receivers of the Fading of Radio Signals. *Proceedings of the Physical Society. Section B*, **63**, 106–121. 12, 66, 67, 73, 74, 96

Businger, J.A. (1988). A note on the Businger-Dyer profiles. *Boundary-Layer Meteorology*, **42**, 145–151. 60

Businger, J.A., Wyngaard, J.C., Izumi, Y. & Bradley, E.F. (1971). Flux-profile relationships in the atmospheric surface layer. *Journal of Atmospheric Sciences*, **28**, 181–189. 59

Chen, S.R. & Cai, C.S. (2004). Accident assessment of vehicles on long-span bridges in windy environments. *Journal of Wind Engineering and Industrial Aerodynamics*, **92**, 991–1024. 32, 66

Churnside, J.H., Lataitis, R.J. & Lawrence, R.S. (1988). Localized measurements of refractive turbulence using spatial filtering of scintillations. *Applied Optics*, **27**, 2199–2213. 34

Clifford, S.F. (1971). Temporal-frequency spectra for a spherical wave propagating through atmospheric turbulence. *Journal of the Optical Society of America*, **61**, 1285–1292. 13, 14, 15, 16, 27, 33, 34, 35, 39, 42, 67, 97, 98, 139, 140, 143, 144, 155, 156

Clifford, S.F. & Churnside, J.H. (1987). Refractive turbulence profiling using synthetic aperture spatial filtering of scintillation. *Applied Optics*, **26**, 1295–1303. 34

De Bruin, H.A.R., Meijninger, W.M.L., Smedman, A.S. & Magnusson, M. (2002). Displaced-beam small aperture scintillometer test. Part I: the WINTEX data-set. *Boundary-Layer Meteorology*, **105**, 129–148. 47, 96

Dyer, A.J. (1974). A review of flux-profile relationships. *Boundary-Layer Meteorology*, **7**, 363–372. 60, 61

Earnshaw, K.B., Wang, T.I., Lawrence, R.S. & Greunke, R.G. (1978). A feasibility study of identifying weather by laser forward scattering. *Journal of Applied Meteorology*, **17**, 1476–1481. 47, 117

Farge, M. (1992). Wavelet Transforms and their Applications to Turbulence. *Annual Review of Fluid Mechanics*, **24**, 395–458. 21

Foken, T. (2008). *Micrometeorology*. Springer, Berlin Heidelberg. 18

Furger, M., Drobinski, P., Prévôt, A.S.H., Weber, R.O., Graber, W.K. & Neininger, B. (2001). Comparison of Horizontal and Vertical Scintillometer Crosswinds during Strong Foehn with Lidar and Aircraft Measurements. *Journal of Atmospheric and Oceanic Technology*, **18**, 1975. 32, 66

Garratt, J.R. (1992). *The atmospheric boundary layer*. Cambridge University Press, U.K. 17

Gerz, T., Holzäpfel, F. & Darracq, D. (2002). Commercial aircraft wake vortices. *Progress in Aerospace Sciences*, **38**, 181–208. 116, 118

Gerz, T., Holzäpfel, F., Bryant, W., Köpp, F., Frech, M., Tafferner, A. & Winckelmans, G. (2005). Research towards a wake-vortex advisory system for optimal aircraft spacing. *Comptes Rendus Physique*, **6**, 501–523. 116, 118, 145

Godwin, K.S., De Wekker, S.F.J. & Emmitt, G.D. (2012). Retrieving Winds in the Surface Layer over Land Using an Airborne Doppler Lidar. *Journal of Atmospheric and Oceanic Technology*, **29**, 487–499. 116, 145

Green, A.E., Astill, M.S., McAneney, K.J. & Nieveen, J.P. (2001). Path-averaged surface fluxes determined from infrared and microwave scintillometers. *Agricultural and Forest Meteorology*, **109**, 233–247. 28, 32, 116

Hallock, J.N. & Osgood, S.P. (2003). Wake vortex effects on parallel runway operations. *AIAA*, **379**, 1–11. 116, 145

Harris, M., Young, R.I., Köpp, F., Dolfi, A. & Cariou, J.P. (2002). Wake vortex detection and monitoring. *Aerospace Science and Technology*, **6**, 325–331. 116, 145

Hartogensis, O.K. (2006). *Exploring Scintillometry in the Stable Atmospheric Surface Layer*. Ph.D. thesis, Wageningen University. 20, 38, 43

Hartogensis, O.K., Watts, C.J., Rodriguez, J.C. & De Bruin, H.A.R. (2003). Derivation of an Effective Height for Scintillometers: La Poza Experiment in Northwest Mexico. *Journal of Hydrometeorology*, **4**, 915–928. 47, 59

Heneghan, J.M. & Ishimaru, A. (1974). Remote determination of the profiles of the atmospheric structure constant and wind velocity along a line-of-sight path by a statistical inversion procedure. *IEEE Transactions on Antennas and Propagation*, **22**, 457–464. 32

Hirsikko, A., O'Connor, E.J., Komppula, M., Korhonen, K., Pfüller, A., Giannakaki, E., Wood, C.R., Bauer-Pfundstein, M., Poikonen, A., Karppinen, T., Lonka, H., Kurri, M., Heinonen, J., Moisseev, D., Asmi, E., Aaltonen, V., Nordbo, A., Rodriguez, E., Lihavainen, H., Laaksonen, A., Lehtinen, K.E.J., Laurila, T., Petäjä, T., Kulmala, M. & Viisanen, Y. (2014). Observing wind, aerosol particles, cloud and precipitation: Finland's new ground-based remote-sensing network. *Atmospheric Measurement Techniques*, **7**, 1351–1375. 100, 103

Holzäpfel, F. & Steen, M. (2007). Aircraft Wake-Vortex Evolution in Ground Proximity: Analysis and Parameterization. *American Institute of Aeronautics and Astronautics Journal*, **45**, 218–227. 116, 145

Holzäpfel, F., Hofbauer, T., Darracq, D., Moet, H., Garnier, F. & Cago, C. (2003). Analysis of wake vortex decay mechanisms in the atmosphere. *Aerospace Science and Technology*, **7**, 263–275. 118

HSY (2008). SeutuCD (CD-rom). 102

Järvi, L., Hannuniemi, H., Hussein, T., Junninen, H., Aalto, P., Hillamo, R., Mkel, T., Keronen, P., Siivola, E., Vesala, T. & Kulmala, M. (2009). The urban measurement station SMEAR III: Continuous monitoring of air pollution and surface–atmosphere interactions in Helsinki, Finland. *Boreal Environmental Research*, **14**, 86–109. 103

Kastner-Klein, P. & Rotach, M.W. (2004). Mean flow and turbulence characteristics in an urban roughenss sublayer. *Boundary-Layer Meteorology*, **111**, 58–84. 101

Kleissl, J., Hong, S.H. & Hendrickx, J.M.H. (2009). New Mexico Scintillometer Network: Supporting Remote Sensing and Hydrologic and Meteorological Models. *Bulletin of the American Meteorological Society*, **90**, 207–218. 11

Kolmogorov, A.N. (1941). The local structure of turbulence in an incompressible viscous fluid for very large Reynolds numbers. *Dokl. Akad. Nauk.*, **30**, 299–303. 17, 18, 25, 36, 68, 98, 119

Koschmieder, H. (1924). Theorie der horizontalen Sichtweite. *Beitr. Phys. freie Atmos.*, **12**, 171–181. 120

Krasny, R. (1987). Computation of vortex sheet roll-up in the Trefftz plane. *Journal of Fluid Mechanics*, **184**, 123–155. 118

Lau, K.M. & Weng, H. (1995). Climate signal detection using wavelet transform: How to make a time series sing. *Bulletin of the American Meteorological Society*, **76**, 2391–2402. 21

Lawrence, R.S., Ochs, G.R. & Clifford, S.F. (1972). Use of scintillations to measure average wind across a light beam. *Applied Optics*, **11**, 239–43. 9, 12, 13, 14, 15, 16, 24, 32, 33, 66, 67, 68, 73, 75, 89, 97, 99, 111, 116, 119, 122, 139, 140, 143, 144, 155, 156

Medeiros Filho, F.C., Jayasuriya, D.A.R., Cole, R.S. & Helmis, C.G. (1983). Spectral density of millimeter wave amplitude scintillations in an absorption region. *IEEE Transactions on Antennas and Propagation*, **31**, 672–676. 40

Meijninger, W.M.L. & de Bruin, H.A.R. (2000). The sensible heat fluxes over irrigated areas in western Turkey determined with a large aperture scintillometer. *Journal of Hydrology*, **229**, 42–49. 116

Meijninger, W.M.L., Green, A.E., Hartogensis, O.K., Kohsiek, W., Hoedjes, J.C.B., Zuurbier, R.M. & De Bruin, H.A.R. (2002a). Determination of area-averaged water vapour fluxes with Large Aperture and Radio Wave Scintillometers over a heterogeneous surface - Flevoland Field Experiment. *Boundary-Layer Meteorology*, **105**, 63–83. 28, 32, 96

Meijninger, W.M.L., Hartogensis, O.K., Kohsiek, W., Hoedjes, J.C.B., Zuurbier, R.M. & De Bruin, H.A.R. (2002b). Determination of area-averaged sensible heat fluxes with a large aperture scintillometer over a heterogeneous surface - Flevoland field experiment. *Boundary-Layer Meteorology*, **105**, 37–62. 32, 96

Meulen, J.P., van der (1998). Wake Vortex Induced Wind measurements at Airfields: A simple Algorithm to Reduce the Vortex Impact. *Instruments and Observing Methods Reports*, **WMO/TD No.** 125

Monin, A. & Yaglom, A. (1975). *Statistical Fluid mechanics of Turbulence Vol. 2*. MIT Press, Cambridge, United Kingdom. 18

REFERENCES

Monin, A.S. & Yaglom, A.M. (1971). *Statistical Fluid mechanics of Turbulence Vol. 1*. MIT Press, Cambridge, United Kingdom. 18

Nedvidek, F.J., Kucerovsky, Z. & Brannen, E. (1983). An instrument for the measurement of precipitation rate by near-infrared extinction. *Journal of climate and applied meteorology*, **22**, 1581–1586. 147

Nieveen, J.P., Green, A.E. & Kohsiek, W. (1998). Using a large-aperture scintillometer to measure absorption and refractive index fluctuations. *Boundary-Layer Meteorology*, **87**, 101–116. 33, 36, 39, 40, 41, 45, 98, 146

Nordbo, A., Järvi, L., Haapanala, S., Moilanen, J. & Vesala, T. (2013). Intra-City Variation in Urban Morphology and Turbulence Structure in Helsinki, Finland. *Boundary-Layer Meteorology*, **146**, 469–496. 101, 103

Obukhov, A.M. (1949). Structure of the temperature field in turbulent flow. *Izv. Akad. Nauk.*, **13**, 58–69. 18

Oncley, S.P., Friehe, C.A., Larue, J.C., Businger, J.A., Itsweire, E.C. & Chang, S.S. (1996). Surface-layer fluxes, profiles, and turbulence measurements over uniform terrain under near-neutral conditions. *Journal of the Atmospheric Sciences*, **53**, 1029–1044. 34, 41

PaiTuli (2012). Topographic Dataset of National Land Survey of Finland. 102

Paulson, C.A. (1970). The mathematical representation of wind speed and temperature profiles in the unstable atmospheric surface layer. *Journal of Applied Meteorology*, **9**, 857–861. 60, 61

Poggio, L.P., Furger, M., Prévôt, A.H., Graber, W.K. & Andreas, E.L. (2000). Scintillometer Wind Measurements over Complex Terrain. *Journal of Atmospheric and Oceanic Technology*, **17**, 17–26. 32, 33, 34, 53, 66, 67, 73, 74, 96, 116, 117, 143

Potvin, G., Dion, D. & Forand, J.L. (2005). Wind effects on scintillation decorrelation times. *Optical Engineering*, **44**, 016001. 55, 56, 58, 80, 89

Robins, R.E. & Delisit, D.P. (1993). Potential Hazard of Aircraft Wake Vortices in Ground Effect with Crosswind. *Journal of Aircraft*, **30**, 201–206. 118, 122

Robinson, P.J. (1989). The influence of weather on flight operations at the Atlanta Hartsfield International Airport. *Weather and Forecasting*, **4**, 461–468. 117

Roth, M. (2000). Review of atmospheric turbulence over cities. *Quarterly Journal of the Royal Meterological Society*, **126**, 941–990. 101

Shen, S., Ding, F., Han, J., Yuh-Lang, L., Arya, S.P. & Proctor, F.H. (1999). Numerical modeling studies of wake vortices: real case simulations. *Proceedings of the 37th AIAA Aerospace Sciences Meeting*. 145

Solignac, P.A., Brut, A., Selves, J.L., Béteille, J.P. & Gastellu-Etchegorry, J.P. (2012). Attenuating the Absorption Contribution on ${C_{n^{2}}}$ Estimates with a Large-Aperture Scintillometer. *Boundary-Layer Meteorology*, **143**, 261–283. 146

Tatarskii, V.I. (1961). *Wave propagation in a turbulent medium*. McGraw-Hill, New York. 26, 35, 119

Thompson, R. (1985). A note on restricted maximum likelihood estimation with an alternative outlier model. *Journal of the Royal Statistical Society. Series B*, **47**, 53–55. 86

Torrence, C. & Compo, G.P. (1998). A Practical Guide to Wavelet Analysis. *Bulletin of the American Meteorological Society*, **79**, 61–78. 21, 22, 23, 38

Uijlenhoet, R., Cohard, J.M. & Gosset, M. (2011). Path-average rainfall estimation from optical extinction measurements using a large-aperture scintillometer. *Journal of Hydrometeorology*, **12**, 955–972. 147

van der Velde, I.R., Steeneveld, G.J., Wichers Schreur, B.G.J. & Holtslag, a.a.M. (2010). Modeling and Forecasting the Onset and Duration of Severe Radiation Fog under Frost Conditions. *Monthly Weather Review*, **138**, 4237–4253. 117

van Dinther, D. & Hartogensis, O.K. (2014). Using the Time-Lag-Correlation function of Dual-Aperture-Scintillometer measurements to obtain the Crosswind. *Journal of Atmospheric and Oceanic Technology*, **31**, 62–78. 65, 96, 97, 98, 100, 108, 112, 117, 118, 122

van Dinther, D., Hartogensis, O.K. & Moene, A.F. (2013). Crosswinds from a Single-Aperture Scintillometer Using Spectral Techniques. *Journal of Atmospheric and Oceanic Technology*, **30**, 3–21. 31, 67, 77, 78, 79, 81, 82, 87, 88, 90, 96, 97, 98, 108, 109, 110, 112, 117

van Dinther, D., Wood, C.R., Hartogensis, O.K., Nordbo, A. & O'Connor, E.J. (2014). Observing crosswind over urban terrain using scintillometer and Doppler lidar. *Atmospheric Measurement Techniques Discussions*, **7**, 6431–6456. 95

Van Kesteren, B., Hartogensis, O.K., van Dinther, D., Moene, A.F. & De Bruin, H.A.R. (2013). Measuring H2O and CO2 fluxes at field scales with scintillometry: Part I Introduction and validation of four methods. *Agricultural and Forest Meteorology*, **178-179**, 75–87. 11

Van Kesteren, B., Beyrich, F., Hartogensis, O.K. & Braam, M. (2014). Long-term evaluation of the Scintec boundary-layer scintillometer and the Wageningen large-aperture scintillometer: Implications for scintillometer users. *Boundary-Layer Meteorology*, **Under review**. 146

Vogt, H. (1968). Visibility measurement using backscattered light. *Journal of the Atmospheric Sciences*, **25**, 912–918. 120

Wang, T.I. & Clifford, S.F. (1975). Use of rainfall-induced optical scintillations to measure path-averaged rain parameters. *Journal of the Optical Society of America*, **65**, 927. 147

Wang, T.I., Ochs, G.R. & Clifford, S.F. (1978). A saturation-resistant optical scintillometer to measure C_{n^2}. *Journal of the Optical Society of America*, **68**, 334. 28, 29, 30, 34, 35, 42, 99, 103

Wang, T.I., Earnshaw, K.B. & Lawrence, R.S. (1979). Path-averaged measurements of rain rate and raindrop size distribution using a fast-response optical sensor. *Journal of Applied Meteorology*, **18**, 654–660. 147

Wang, T.I., Ochs, G.R. & Lawrence, R.S. (1981). Wind measurements by the temporal cross-correlation of the optical scintillations. *Applied Optics*, **20**, 4073–81. 9, 12, 24, 32, 33, 34, 66, 67, 68, 78, 96, 116, 119

Wang, T.I., Lataitis, R., Lawrence, R.S. & Ochs, G.R. (1982). Laser Weather Identifier: Present and Future. *Journal of Applied Meteorology*, **21**, 1747–1753. 147, 148

Ward, H.C., Evans, J.G. & Grimmond, C.S.B. (2011). Effects of Non-Uniform Crosswind Fields on Scintillometry Measurements. *Boundary-Layer Meteorology*, **141**, 143–163. 13, 33, 40, 41, 48, 96

Werner, C., Streicher, J., Leike, I. & Münkel, C. (2005). Visibility and Cloud Lidar. In C. Weitkamp, ed., *Lidar Range-Resolved Optical Remote Sensing of the Atmosphere*, chap. 6, 164–186, Springer. 120

Wilczak, J.M., Oncley, S.P. & Stage, S.A. (2001). Sonic anemometer tilt correction algorithms. *Boundary-Layer Meteorology*, **99**, 127–150. 49

REFERENCES

Wong, D.K.Y., Pitfield, D.E., Caves, R.E. & Appleyard, A.J. (2006). Quantifying and characterising aviation accident risk factors. *Journal of Air Transport Management*, **12**, 352–357. 9

Wood, C.R., Järvi, L., Kouznetsov, R.D., Nordbo, A., Joffre, S., Drebs, A., Vihma, T., Hirsikko, A., Suomi, I., Fortelius, C., O'Connor, E., Moiseev, D., Haapanala, S., Moilanen, J., Kangas, M., Karppinen, A., Vesala, T. & Kukkonen, J. (2013a). An Overview of the Urban Boundary Layer Atmosphere Network in Helsinki. *Bulletin of the American Meteorological Society*, **94**, 1675–1690. 97

Wood, C.R., Kouznetsov, R.D., Gierens, R., Nordbo, A., Järvi, L., Kallistratova, M.A. & Kukkonen, J. (2013b). On the Temperature Structure Parameter and Sensible Heat Flux over Helsinki from Sonic Anemometry and Scintillometry. *Journal of Atmospheric and Oceanic Technology*, **14**, 1604–1615. 101

Wood, C.R., Pauscher, L., Ward, H.C., Kotthaus, S., Barlow, J.F., Gouvea, M., Lane, S.E. & Grimmond, C.S.B. (2013c). Wind observations above an urban river using a new lidar technique, scintillometry and anemometry. *The Science of the total environment*, **442**, 527–33. 15, 66, 96, 97, 100, 108

Samenvatting

Dit hoofdstuk geeft een overzicht van de belangrijkste bevindingen van dit proefschrift. Het overzicht wordt gegeven aan de hand van vier onderzoeksvragen.

In dit proefschrift wordt beschreven hoe een scintillometer de dwarswind op een pad kan meten ($U_\perp$), waar $U_\perp$ gedefinieerd is als de windcomponent loodrecht op een pad (in dit geval het scintillometer pad). Padgemiddelde dwarswindmetingen ($\overline{U_\perp}$) zijn onder andere belangrijk op vliegvelden, waar een sterke dwarswind een veiligheidsrisico vormt voor vliegtuigen die landen en opstijgen. Een scintillometer bestaat uit een zender en ontvanger, die typisch enkele honderden meters tot enkele kilometers uit elkaar staan. De zender zendt licht uit, welke gebroken wordt door het turbulente wervelveld in de atmosfeer. Hierdoor meet de ontvanger intensiteit schommelingen. Deze schommelingen kunnen gerelateerd worden aan de dwarswind.

De eerste onderzoeksvraag van dit proefschrift was:

Vraag 1: Kunnen de theoretische modellen van Lawrence *et al.* (1972) en Clifford (1971) gebruikt worden om de dwarswind metingen van een scintillometer te kalibreren, in plaats van experimentele kalibratie?

In hoofdstuk 3 is getest of het theoretisch model van een scintillatie spectrum ($S_{11}(f)$) van Clifford (1971) de kalibratieconstanten die de relatie tussen $\overline{U_\perp}$ en de hoekfrequentie en $\overline{U_\perp}$ en de maximumfrequentie kan vinden. De resultaten van $\overline{U_\perp}$ verkregen uit de spectra waren vergelijkbaar met $U_\perp$-metingen verkregen uit een sonische anemometer. Hierdoor kunnen we concluderen dat het model van Clifford (1971) inderdaad gebruikt kan worden om $\overline{U_\perp}$-metingen uit $S_{11}(f)$ mogelijk te maken, dit maakt dure experimentele kalibratie overbodig.

In hoofdstuk 4 is getest of het theoretisch model van de tijdsverschoven correlatie functie van een dubbele scintillometer ($r_{12}(\tau)$) van Lawrence *et al.* (1972) gebruikt

kan worden om de kalibratieconstanten te vinden. De constanten geven de relatie aan tussen $\overline{U_\perp}$ en de tijdsverschuiving waar het maximum in $r_{12}(\tau)$ zich bevindt, tussen $\overline{U_\perp}$ en de tijdsverschuiving waar $r_{12}(\tau)$ en de tijdsverschoven variantie functie elkaar snijden en tussen $\overline{U_\perp}$ en de hellingshoek van $r_{12}(\tau)$ voor nul tijdsverschuiving. Het voordeel van $\overline{U_\perp}$ verkrijgen uit $r_{12}(\tau)$ in plaats van $S_{11}(f)$ is dat uit $r_{12}(\tau)$ ook de kant bepaald kan worden van waaruit de wind het pad inwaait (in andere woorden het teken van $\overline{U_\perp}$). Een ander voordeel is dat $r_{12}(\tau)$ en daardoor $\overline{U_\perp}$ verkregen kan worden over een relatief kort tijdsbestek ($\sim$ 10 s). De resultaten van $\overline{U_\perp}$ verkregen met de scintillometer zijn opnieuw vergeleken met die verkregen uit een sonische anemometer. Uit de resultaten kan geconcludeerd worden dat het model van Lawrence *et al.* (1972) inderdaad gebruikt kan worden om de kalibratieconstanten van de drie methodes te vinden. Voor de Briggs methode bleek de "constante" (C_B) anders dan verwacht niet constant te zijn, maar toe te nemen voor hoge $\overline{U_\perp}$-waardes (> 5 m s^{-1}). Daarom concluderen we dat het aannemen dat C_B constant is resulteert in fouten voor de hoge waardes van $\overline{U_\perp}$.

De tweede onderzoeksvraag van dit proefschrift was:

Vraag 2: Kan de vorm van de theoretische modellen van Lawrence *et al.* (1972) en Clifford (1971) gebruikt worden om de dwarswind te bepalen?

In dit proefschrift zijn twee nieuwe methodes geïntroduceerd om antwoord te krijgen op deze vraag: de cumulatief spectrum methode (geïntroduceerd in hoofdstuk 3) en de opzoektabel methode (geïntroduceerd in hoofdstuk 4). De cumulatief spectrum methode gebruikt vijf punten uit het cumulatief spectrum om $\overline{U_\perp}$ te bepalen. Van alle drie de methodes die $\overline{U_\perp}$ bepaald uit $S_{11}(f)$ gaf deze methode het beste resultaat.

De opzoektabel methode bepaald $\overline{U_\perp}$ door een gemeten $r_{12}(\tau)$ te vergelijken met $r_{12}(\tau)$ uit het theoretisch model (welke opgeslagen zijn in een tabel). Deze methode toonde de beste resultaten van alle methodes die $\overline{U_\perp}$ verkreeg uit $r_{12}(\tau)$ voor waardes van $\overline{U_\perp}$ boven de 2 m s^{-1}.

De derde onderzoeksvraag gesteld in dit proefschrift was:

Vraag 3: Hoe worden de dwarswindmetingen van een scintillometer beïnvloed door een variabele dwarswind over het scintillometer pad?

Appendix 3A onderzoekt de theoretische invloed van een schuin scintillometer pad op de $\overline{U_\perp}$-waardes uitgerekend uit $S_{11}(f)$. Het verschil in meethoogte langs het schuine pad zorgt ervoor dat $U_\perp$ veranderd over het pad als functie van het windprofiel. Zelfs

voor extreem schuin pad (van 2 naar 100 m) bedroeg de maximale fout in $\overline{U_\perp}$ slechts 8 %.

In hoofdstuk 4 hebben we onderzocht hoe $r_{12}(\tau)$ beïnvloed wordt door een hypothetisch $U_\perp$ windveld van twee verschillende waardes op de twee helften van het pad. De hieruit volgende $r_{12}(\tau)$ is een combinatie van $r_{12}(\tau)$ van de twee verschillende dwarswinden. Hierdoor, zal waarschijnlijk ook $\overline{U_\perp}$ verkregen uit $r_{12}(\tau)$ beïnvloed worden door een variabel $\overline{U_\perp}$-veld.

In hoofdstuk 5 hebben we onderzocht hoeveel de metingen van $\overline{U_\perp}$ van de scintillometer beïnvloedt worden door een variabel $U_\perp$-veld langs het scintillometer pad. Hiervoor zijn er metingen verricht boven stedelijk gebied in Helsinki, Finland. In dit gebied verwachten we dat $U_\perp$ varieert over het scintillometer pad. De metingen van de scintillometer worden vergeleken met Doppler lidar metingen, welke in staat is om $U_\perp$ te bepalen voor verschillende afstanden langs het pad ($U_\perp(x)$, waar x de positie langs het pad is). Om $\overline{U_\perp}$ uit de scintillometer te bepalen zijn de cumulatieve spectrum methode en opzoektabel methode toegepast. Beide methodes gaven $\overline{U_\perp}$-waardes die redelijk goed vergelijkbaar waren met die van de Doppler lidar, zeker gezien het complexe gebied waar de metingen verkregen zijn. Deze goede vergelijkbaarheid geeft aan dat beide meetapparaten in staat zijn $\overline{U_\perp}$ te bepalen in het complexe stedelijk gebied. Het onderzoek van vier gevallen toont aan dat de cumulatieve spectrum methode minder vatbaar is voor een variabele $U_\perp(x)$ dan de opzoektabel methode. Echter de opzoektabel methode kan worden aangepast om meer geschikt te zijn om $\overline{U_\perp}$ te bepalen voor condities waar $U_\perp(x)$ variabel is.

De laatste onderzoeksvraag gesteld in dit proefschrift was:

Vraag 4: In hoeverre is de scintillometer geschikt voor het detecteren van zogwervels, dwarswind en zicht langs een landingsbaan?

Deze vraag wordt beantwoordt in hoofdstuk 6 van dit proefschrift met behulp van metingen verzameld langs een landingsbaan op de luchthaven Schiphol (Amsterdam, Nederland). De scintillometermetingen zijn vergeleken met wind- en zichtmetingen verricht op de luchthaven. De resultaten tonen aan dat, na het toepassen van een filter op uitschieters, de scintillometer ook in staat is $\overline{U_\perp}$ te bepalen met behulp van de opzoektabel methode langs een landingsbaan over de korte tijdschaal nodig op vliegvelden (3 s). Alhoewel er een fitler op uitschieters is toegepast is de scintillometer nog steeds in staat de maximum $\overline{U_\perp}$ over 10 min te bepalen.

Het scintillometer signaal daalt zeer sterk als gevolg van een afname van het zicht. Hierdoor is het uitdagend een waarde voor zicht te kwantificeren met behulp van

het scintillometer signaal. De scintillometer is echter wel geschikt om tijdsperiode te identificeren waar het zicht minder dan 10 km is.

De resultaten tonen aan dat de scintillometer 's nachts in staat is zogwervels te detecteren, door middel van de extra fluctuaties die zogwervels introduceren in het scintillometer signaal. De hoeveelheid fluctuaties (ook wel variantie) geeft zelfs informatie over de sterkte van een zogwervel. Overdag wordt het scintillometer signaal sterk beïnvloed door de achtergrond atmosferische turbulentie, waardoor het onder deze omstandigheden zeer moeilijk is zogwervels te detecteren met behulp van een scintillometer.

Dank / Thanks!

Na een dikke vierenhalf jaar is het eindelijk zover; m'n boekje is af! Natuurlijk was dit niet mogelijk geweest zonder een aantal mensen en die wil ik bij deze bedanken.

Allereerst wil ik Oscar bedanken. Het is alweer een hele tijd geleden dat ik als student binnenliep voor de start van m'n master thesis, toen nog onwetend over alles wat met scintillometrie te maken had. Inmiddels is dat anders, bedankt voor het delen van jouw kennis en het duwtje in de rug wanneer ik dat nodig had. Fijn dat jij er altijd van overtuigd was dat ik mijn PhD kon afronden, ook als ik daar zelf aan twijfelde.

Bert bedankt voor het vertrouwen dat ik mijn PhD tot een goed einde zou afronden. Voor mijn persoonlijke leven nog belangrijker; bedankt dat je al die tijd terug de potentie zag in Eduardo, waardoor hij uiteindelijk bij onze groep terecht kwam.

Ylona en Anneke ook bedankt als mijn paranimfen. Ylona de deur staat ook in Zürich altijd open als ik je nodig heb. Super bedankt daarvoor en alle leuke tripjes in Zwitserland wanneer ik een vakantie nodig had (ook Bram bedankt hiervoor). Anneke al tijdens onze studietijd bleek dat we goed konden samenwerken en dat we dezelfde interesses hadden; mircometeorologie en meten. Waar ik je vooral voor wil bedanken is het luisterend oor dat er altijd was, met name op het einde van m'n PhD werd deze veelvuldig gebruikt. Bedankt ook voor de adviezen, zelfs als ik ze niet opvolgde is een second opinion altijd fijn!

Thanks also to all my other co-authors for their insights and comments on my papers. Arnold bedankt voor het meedenken aan mijn eerste artikel, maar nog meer voor al je enthousiasme voor micro-meteorologie. Je enthousiasme werkte aanstekelijk waardoor ik voor m'n BSc-thesis bij jouw terecht kwam, en een paar jaar later ook via jouw bij Oscar terecht kwam voor m'n MSc-thesis wat weer leidde naar m'n PhD. Curtis thanks for the always fast reply from Helsinki and supplying the Helsinki data. I really enjoyed the challenging data; working on the edge of the possibilities of both scintillometer and Doppler lidar technology.

DANK / THANKS!

Natuurlijk wil ik ook mijn kantoorgenootjes bedanken voor alle discussies, meedenken bij latex/matlab issues, het doorstaan van al mijn geklets en het opdrinken van de thee. In die vierenhalf jaar toch redelijk wat kantoren versleten: de mannen van Atlas (Chiel, Bram, Joel, Joost en Bart), de allergie-club in Aqua (Anneke en Bram) en de airco-kamer in Lumen (Anneke, Michał, Natalie en Miranda). Miranda ook bedankt voor de hulp met de voorkant, ik vind hem top! Ook de rest van de vakgroep bedankt voor de lunches, pauzes, etentjes en heel veel meer. Kees bedankt voor het meehelpen de scintillometer op te stellen op Schiphol en het oplossen van PC-issues als die er waren. Caroline bedankt voor de hulp wanneer dat nodig was.

Tijdens mijn PhD was er natuurlijk ook de nodige ontspanning nodig om even alles te vergeten. Velda, Justine en Laura bedankt voor onze quiz-avondjes, bioscoopbezoekjes en etentjes. Marjolein en Lotty, top dat we nog steeds onze dinerrouler avondjes hebben. Hopelijk lukt dat ook nog als ik verhuist ben richting Petten. Doortje bedankt voor alle weekend die (veel) te snel voorbij waren. Marina ik heb erg genoten van onze roadtrip samen, ook bedankt voor de thee-pauzes wanneer er weer wat stoom afgeblazen moest worden. Veraniek bedankt voor de puzzel-avondjes. Volleybal was er altijd om de nodige frustraties eruit te slaan als dat nodig was, bedankt voor alle gezelligheid bij mijn teamgenootjes bij WaHo en Invicta. Nog een extra bedankje voor de voor-volleybal-eters ;P (Annemarie, Annewieke, Elja en Linda), zelden zo hard gelachen als met jullie zelfs op de topstress tijd tijdens mijn onderzoek.

Dan is er natuurlijk de familie. Paps en mams jullie zijn er altijd, maar nog belangrijker jullie staan altijd achter ons (zowel bij Ylona als voor mij) welke keuze we ook maken. Bedankt dat jullie ook Eduardo zo snel hebben opgenomen in ons gezinnetje. Marijke bedankt voor onze stedentripjes, die houden we erin ;)

Last but not least my baby Eduardo. Thanks for ALWAYS being there and everything you do for me. But most improtantly thanks for being you. I can't imagine my life without you anymore.

List of publications

van Dinther, D., Hartogensis, O.K. & Moene, A.F. (2013). Crosswinds from a Single-Aperture Scintillometer Using Spectral Techniques. *Journal of Atmospheric and Oceanic Technology*, **30**, 3–21.

van Dinther, D. & Hartogensis, O.K. (2014). Using the Time-Lag-Correlation function of Dual-Aperture-Scintillometer measurements to obtain the Crosswind. *Journal of Atmospheric and Oceanic Technology*, **31**, 62–78.

van Dinther, D., Wood, C.R., Hartogensis, O.K., Nordbo, A. & O'Connor, E.J. (2014). Observing crosswind over urban terrain using scintillometer and Doppler lidar. *Atmospheric Measurement Techniques Discussions*, **7**, 6431–6456.

van Dinther, D. and Hartogensis, O.K. & Holtslag, A.A.M. (2014). Runway wake vortex, crosswind, and visibility detection with a scintillometer at Schiphol airport. *Boundary-Layer Meteorology*, **Under review**

Beyrich, F., Bange, J., Hartogensis, O.K., Raasch, S., Braam, M., **van Dinther, D.**, Gräf, D., van Kesteren, B., Kroonenberg, A.C., Maronga, B., Martin, S. & Moene, A.F. (2012). Towards a Validation of Scintillometer Measurements: The LITFASS-2009 Experiment. *Boundary-Layer Meteorology*, **144**, 83–112.

Van Kesteren, B., Hartogensis, O.K., **van Dinther, D.**, Moene, A.F. & De Bruin, H.A.R. (2013). Measuring H2O and CO2 fluxes at field scales with scintillometry: Part I Introduction and validation of four methods. *Agricultural and Forest Meteorology*,**178-179**, 75–87.

Van Kesteren, B., Hartogensis, O.K., **van Dinther, D.**, Moene, A.F., De Bruin, H.A.R. & Holtslag, A.A.M. (2013). Measuring H2O and CO2 fluxes at field scales with scintillometry: Part II Validation and application of 1-min flux estimates. *Agricultural and Forest Meteorology*, **178-179**, 88–105.

Maronga, B., Moene, A.F., **van Dinther, D.**, Raasch, S., Bosveld, F.C. & Gioli, B. (2013). Derivation of Structure Parameters of Temperature and Humidity in the Convective Boundary Layer from Large-Eddy Simulations and Implications for the Interpretation of Scintillometer Observations. *Boundary-Layer Meteorology*, **148**, 1–30.

Netherlands Research School for the
Socio-Economic and Natural Sciences of the Environment

D I P L O M A

For specialised PhD training

The Netherlands Research School for the
Socio-Economic and Natural Sciences of the Environment
(SENSE) declares that

Daniëlle van Dinther

born on 14 May 1986 in Sassenheim, The Netherlands

has successfully fulfilled all requirements of the
Educational Programme of SENSE.

Wageningen, 16 January 2014

the Chairman of the SENSE board	the SENSE Director of Education
Prof. dr. Huub Rijnaarts	Dr. Ad van Dommelen

The SENSE Research School has been accredited by the Royal Netherlands Academy of Arts and Sciences (KNAW)

K O N I N K L I J K E N E D E R L A N D S E
A K A D E M I E V A N W E T E N S C H A P P E N

The SENSE Research School declares that **Ms Daniëlle van Dinther** has successfully fulfilled all requirements of the Educational PhD Programme of SENSE with a work load of 44.2 EC, including the following activities:

SENSE PhD Courses

- Environmental Research in Context (2010)
- Research Context Activity: Organising 3rd scintillometer workshop, Wageningen (2011)
- Autumn School: Biogeochemistry and -physics of the lower atmosphere (2010)
- Bridging the scale gap between atmospheric scales (2012)

Other PhD Courses

- PhD Competence Assessment (2010)
- Scientific Writing (2011)
- Remote Sensing in Wind Energy, Risø DTU, Roskilde, Denmark (2011)
- Techniques for Writing and Presenting a Scientific Paper (2012)
- Voice and Presentation (2013)

Management and Didactic Skills Training

- Teaching assistant for practical 'Inleiding Atmosfeer' (2010), 'Field Practical Meteorology' (2011), 'Atmospheric Practical' (2012), and 'Environmental Data Collection and Analysis'(2012-2013)
- Supervision of BSc thesis entitled 'Scintillometer Crosswind Measurements at Airport Runways' (2012)

Selection of Oral Presentations

- *Obtaining crosswind from a single aperture scintillometers.* Boundary Layer Turbulence meeting - BBOS, 26 November 2010, Wageningen, The Netherlands
- *Obtaining crosswind from a scintillometer.* SENSE symposium 'Modelling & Observing Earth System Compartments, 22 February 2011, Wageningen, The Netherlands
- *Crosswind from a Single Aperture Scintillometer Using Spectral Techniques*. Symposium on Boundary Layers and Turbulence, 9-13 July, Boston, United States
- *Obtaining Crosswind from a Dual Aperture Scintillometer*. Buys Ballot Research School (BBOS) Autumn meeting, 24-26 October 2012, Berg en Dal, The Netherlands

SENSE Coordinator PhD Education

Dr. ing. Monique Gulickx